ADVANCE DENSITY FUNCTIONALS BASED ON MODEL EXCHANGE HOLES FOR A WIDE RANGE OF MOLECULAR AND SOLID-STATE SYSTEMS

By

ABHILASH PATRA

Enrolment No: PHYS11201504001

National Institute of Science Education and Research, Bhubaneswar

A thesis submitted to the

Board of Studies in Physical Sciences

In partial fulfillment of requirements

for the Degree of

DOCTOR OF PHILOSOPHY

of

HOMI BHABHA NATIONAL INSTITUTE

August, 2021

Homi Bhabha National Institute

Recommendations of the Viva Voce Committee

As members of the Viva Voce Committee, we certify that we have read the dissertation prepared by **Abhilash Patra** entitled "Advance density functionals based on model exchange holes for wide range of molecular and solid-state systems" and recommend that it may be accepted as fulfilling the thesis requirement for the award of Degree of Doctor of Philosophy.

Chairman - Prof. Bedangadas Mohanty _____ Pom Dhanty _____ 4/8/2021
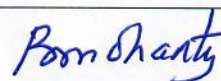
Guide/Convener - Dr. Prasanjit Samal _____ 4-8-21

Examiner - Prof. Manoj K. Harbola _____ M.K.Harb _____ 4-8-21
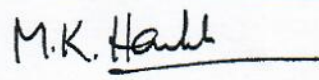
Member 1- Dr. Joydeep Bhattacharjee _____ 4-8-21

Member 2- Dr. A. V. Anil Kumar _____ 4/8/2021
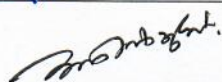
Member 3- Prof. Suresh Kumar Patra _____ 4/8/2021
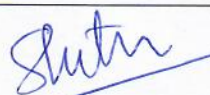
Final approval and acceptance of this thesis is contingent upon the candidates submission of the final copies of the thesis to HBNI.

I/We hereby certify that I/we have read this thesis prepared under my/our direction and recommend that it may be accepted as fulfilling the thesis requirement.

Date: 4-8-21

Place: Bhubaneswar

Guide

STATEMENT BY AUTHOR

This dissertation has been submitted in partial fulfillment of requirements for an advanced degree at Homi Bhabha National Institute (HBNI) and is deposited in the Library to be made available to borrowers under rules of the HBNI.

Brief quotations from this dissertation are allowable without special permission, provided that accurate acknowledgement of source is made. Requests for permission for extended quotation from or reproduction of this manuscript in whole or in part may be granted by the Competent Authority of HBNI when in his or her judgment the proposed use of the material is in the interests of scholarship. In all other instances, however, permission must be obtained from the author.

Abhilash Patra

DECLARATION

I, hereby declare that the investigation presented in the thesis has been carried out by me. The work is original and has not been submitted earlier as a whole or in part for a degree / diploma at this or any other Institution / University.

Abhilash Patra

List of Publications arising from the thesis

Journal

1. "A Parameter-Free Semilocal Exchange Energy Functional for Two-Dimensional Quantum Systems", **Abhilash Patra**, Subrata Jana and Prasanjit Samal, Journal of Physical Chemistry A, **2018**, 122(13), 3455-3461.

2. "Inhomogeneity induced and appropriately parameterized semilocal exchange and correlation energy functionals in two-dimensions", **Abhilash Patra**, Subrata Jana and Prasanjit Samal, Journal of Chemical Physics, **2018**, 148, 134117.

3. "Colle-Salvetti type correlation functionals for two-dimensional quantum dot systems", **Abhilash Patra** and Prasanjit Samal, Chemical Physics Letters, **2019**, 720, 70-75.

4. "Laplacian free and asymptotic corrected semilocal exchange potential applied to the band gap of solids", **Abhilash Patra**, Subrata Jana, Hemanadhan Myneni and Prasanjit Samal, Physical Chemistry Chemical Physics, **2019**, 21 (35), 19639-19650.

5. "Electronic band structure of layers within meta generalized gradient approximation of density functionals", **Abhilash Patra**, Bikash Patra, Lucian A. Constantin, and Prasanjit Samal, Physical Review B, **2020**, 102 (4), 045135.

6. "Long-range screened hybrid-functional theory satisfying the local-density linear response", Subrata Jana, **Abhilash Patra**, Lucian A. Constantin, Hemanadhan Myneni and Prasanjit Samal, Physical Review A, **2019** 99 (4), 042515.

7. "Performance of Tao-Mo Semilocal Functional with rVV10 Dispersion-Correction: Influence of Different Correlation", **Abhilash Patra**, Subrata Jana and Prasanjit Samal, The Journal of Physical Chemistry A, **2019**, 123 (49), 10582-10593.

Conferences

1. Poster:-"A Colle-Salvetti type correlation functional for two dimensional systems", **Abhilash Patra**, National Conference on Recent Trends in Condensed Matter Physics (RTCMP 2017), Bose Institute, Kolkata, West Bengal-700054, India.

2. Poster:-"An Assessment of Semi-local Exchange potentials in the Band Gap Calculation", **Abhilash Patra**, International Workshop on Advanced Materials (IWAM-2017), National Institute of Science & Technology, Berhampur, Orissa-761008, India.

3. Poster:-"Family of Becke potentials: An assessment in band gap calculations", **Abhilash Patra**, International Workshop on Evolution of Electronic Structure Theory & Experimental Realization (EESTER 2018), SRM Institute of Science and Technology & Indian Institute of Technology Madras, Tamil Nadu-600036, India.

Abhilash Patra

DEDICATIONS

Dedicated to

.....

My Family

.....

.....

My Teacher

ACKNOWLEDGEMENTS

Contents

SUMMARY

The density functional theory (DFT) is one of the best methods in describing various physical properties of systems starting from simple atoms, large clusters, periodic bulk solids to surface sciences. Such dominance of DFT over other many-body methods is the combined result of both accuracy and computational efficiency. Modern DFT starts with the Hohenberg-Kohn (HK) theorem [*Phys. Rev.* **136**, B864 (1964)] that provides a complete density-dependent Schrdinger-like equation for the many-particle problem and proves the unique mapping between the external potential and the ground state wavefunction, hence the ground state density. The practical application of DFT established with the Kohn-Sham (KS) formalism [*Phys. Rev.* **140**, A1133 (1965)] proposes transforming the complete interacting real system to a non-interacting fictitious system, keeping the ground state density fixed. In retaining the same density, the modified potential for this imaginary system must reflect the essence of interacting system. Similar to Schrdingers equation for wavefunction, the KS equation contains the kinetic energy term, the classical interaction is otherwise known as Hartree interaction, interaction with the nucleus, and the most important interaction, i.e., the exchange-correlation (xc) interaction, and all of the energy forms are functionals of a density. However, the exact density functional form of xc is unknown. So, we have to rely on the approximated xc functionals of the energy hence the potential. This thesis contains the recent advancement in the approximation of xc functionals and their convenient applications.

This whole work is centered on the development of new approximations for xc functionals focusing on various properties of molecular complexes to materials. The exchange energy can be understood as the interaction between the electron density and the exchange hole surrounding the electron. In a broad sense, the exchange hole is the space around an electron up to which no other electron can enter. So, by modeling the exchange hole, we

can get the exchange energy and exchange potential. We attempt to develop new model exchange holes to address different aspects of molecular or solid-state properties using DFT. Moreover, we start with the dimensional aspect of DFT, where we propose new xc functionals based on generalized exchange hole for pure two-dimensional (2D) quantum systems. The improved xc energies against previously available functionals for parabolic and Gaussian quantum dots are reported. Next, the concept of coordinate transformation of the exchange hole is utilized to model exchange-only potential that is very promising in band gap calculation of bulk materials. It is known that the hybrid methods are very accurate in predicting various properties, however, the development of hybrid methods is not straight forward. We need an exchange hole of any exchange energy functional to model the corresponding hybrid method. So, we derive the exchange hole for three types of exchange energy functionals through the reverse-engineered technique and apply them to construct long-range corrected hybrid functionals that are very favorable for molecular properties. Finally, we focus on density functional methods to address dispersion dominated systems. In this case, we use a well-known semilocal xc energy functional Tao-Mo (TM) [*Phys. Rev. Lett*, **117**, 073001 (2016)], developed from density matrix expansion and generalized coordinate transformed exchange hole with the rVV10 non-local correction [*Phys. Rev. B*, **87**, 041108(R) (2013)] to address Van der Waals systems.

List of Figures

List of Tables

Chapter 1

Introduction

Understanding the electronic structure of atoms, molecules, complexes, solids, surfaces, and nano-structures is helping in realizing the physical, chemical interactions, and predicting new materials that help in the day-to-day life of humankind. To get adequate knowledge, theoretical models of these complex systems are needed to be more precise and cost-effective. All the chemical and physical properties of these systems of interest depend on the correlated electrons present, and the number varies from the simple one-electron hydrogen atom to jumbo structures with thousand of interacting particles. The perfect and error-free inclusion of such many-body interaction in the theoretical model has been a challenge for theoretical physicists and chemists. More precise inclusion of electron-electron interaction achieve accurate description of structural properties, e.g., bond lengths and bond angles of molecules, lattice constants and volume of solids, transport properties, e.g., electrical conductivity, and other properties, e.g., binding energies, ionization potentials, electron affinities, atomization energies, cohesive energies, band structures. Basically, two well-known approaches are very successful in doing so. The first approach being the *ab initio* or *first principle* method uses the elemental Hamiltonian of the system and many-body Schrödinger equation needs to be solved for in this approach And the second approach is modeling a suitable Hamiltonian from available experimental information. The model Hamiltonian approach often uses the coupling constant between two sites, and this physical parameter is determined from the experiment or

the *ab initio* method. This thesis focuses on the first approach for its accuracy, efficiency, and applicability.

We start with the electronic Hamiltonian, decoupled from a complete electron-nucleus system by the *Born-Oppenheimer approximation*. The velocity of nuclei is very slow in comparison with the motion of electrons. As a result, the wavefunction of electrons only depends on the positions of nuclei, and the many-electron Schrödinger equation can be solved with a fixed nuclear configuration. So, only electronic Hamiltonian is written as,

$$\hat{H} = \hat{T}_e + \hat{V}_{n-e} + \hat{V}_{e-e}. \tag{1.1}$$

The N electronic Hamiltonian along with the electronic energy E, and electronic wave function $\Psi = \Psi(x_1, x_2..., x_n)$ completes the Schrödinger equation $\hat{H}\Psi = E\Psi$. The above Hamiltonian contains kinetic energy of N electrons $\hat{T}_e = \sum_{i=1}^{N} \frac{(-i\hbar\nabla_i)^2}{2m}$, interaction between electrons and K number of nuclei $\hat{V}_{n-e} = -\sum_{\alpha=1}^{K}\sum_{i=1}^{N} \frac{Z_\alpha e^2}{|\mathbf{R}_\alpha - \mathbf{r}_i|}$, and the interaction between electrons $\hat{V}_{e-e} = \sum_{i,j=1;i<j}^{N} \frac{e^2}{|\mathbf{r}_i - \mathbf{r}_j|}$. The 'm' present in the $\hat{T}$ is the mass of electrons, $\mathbf{r}_i$ is the position of ith electron, $\mathbf{R}_\alpha$ is position of αth nuclei, e and $Z_\alpha e$ are charges of electrons and nuclei, respectively. In addition to all these interactions, all other external potentials correspond to the electromagnetic field such as electric fields, Zeeman terms are readily included.

Out of different approaches to solve the Schrödinger equation, the Hartree-Fock (HF) approximation is the first method that uses the proper antisymmetric wavefunction, necessary for electronic systems. For an N electron system, the wavefunction is prepared from the *Slater determinant* of individual electronic orbitals,[1,2]

$$\Phi^{HF} = \frac{1}{\sqrt{N!}} \begin{vmatrix} \phi_1(\mathbf{r}_1, \sigma_1) & \phi_2(\mathbf{r}_1, \sigma_1) & \phi_3(\mathbf{r}_1, \sigma_1) & ... & \phi_N(\mathbf{r}_1, \sigma_1) \\ \phi_1(\mathbf{r}_2, \sigma_2) & \phi_2(\mathbf{r}_2, \sigma_2) & \phi_3(\mathbf{r}_2, \sigma_2) & ... & \phi_N(\mathbf{r}_2, \sigma_2) \\ .... \\ \phi_1(\mathbf{r}_N, \sigma_N) & \phi_2(\mathbf{r}_N, \sigma_N) & \phi_3(\mathbf{r}_N, \sigma_N) & ... & \phi_N(\mathbf{r}_N, \sigma_N) \end{vmatrix}, \tag{1.2}$$

where the single particle spin-orbitals $\phi_i(\mathbf{r}_j, \sigma_j)$ consist of both spatial function $\psi_i^\sigma(\mathbf{r}_j)$

and spin variable $\sigma = \uparrow, \downarrow$. Using variational principle, all the single particle orbitals can be determined for ground state Φ^{HF}. For all orthonormal ϕ's, the Φ^{HF} is normalized, i.e., $\langle \Phi^{HF} | \Phi^{HF} \rangle = 1$, and the energy is approximated as the expectation values of the Hamiltonian Eq.(1.1),

$$E^{HF} = \langle \Phi^{HF} | \hat{H} | \Phi^{HF} \rangle = \sum_{i=1}^{N} \sum_{\sigma=\uparrow,\downarrow} \int d^3r \phi_i^*(\mathbf{r}\sigma) [-\frac{1}{2}\nabla^2 + V_{ext}(\mathbf{r})] \phi_i(\mathbf{r}\sigma) \tag{1.3}$$

$$+ \frac{1}{2} \sum_{i,j=1}^{N} \sum_{\sigma,\sigma'=\uparrow,\downarrow} \int d^3r \int d^3r' \phi_i^*(\mathbf{r}\sigma) \phi_j^*(\mathbf{r}'\sigma') \frac{1}{|\mathbf{r}-\mathbf{r}'|} \phi_i(\mathbf{r}\sigma) \phi_j(\mathbf{r}'\sigma')$$

$$- \frac{1}{2} \sum_{i,j=1}^{N} \sum_{\sigma,\sigma'=\uparrow,\downarrow} \int d^3r \int d^3r' \phi_i^*(\mathbf{r}\sigma) \phi_j^*(\mathbf{r}'\sigma') \frac{1}{|\mathbf{r}-\mathbf{r}'|} \phi_j(\mathbf{r}\sigma) \phi_i(\mathbf{r}'\sigma').$$

The term group containing the kinetic energy of electrons and the external potential V_{ext} arising from the nucleus and electron interaction involve expectation values of single particle operators. Whereas, the next two terms known as direct or classical Coulomb, and the exchange interaction of electrons involve double sums over orbitals. It is to be noted that, the Hartree method that uses a wavefunction constructed from multiplication of individual electron wavefunctions gives rise to only classical Coulomb interaction. The HF method corrects the one-electron interaction by canceling the classical Coulomb and the exchange interaction at $i = j$. We will be using the HF exchange energy,

$$E_x^{HF} = -\frac{1}{2} \sum_{i,j=1}^{N} \sum_{\sigma,\sigma'=\uparrow,\downarrow} \int d^3r \int d^3r' \frac{\phi_i^*(\mathbf{r}\sigma)\phi_j^*(\mathbf{r}'\sigma')\phi_j(\mathbf{r}\sigma)\phi_i(\mathbf{r}'\sigma')}{|\mathbf{r}-\mathbf{r}'|} \tag{1.4}$$

further in the thesis. Now, the total energy is minimized with respect to the wavefunction, including orthonormality constraint and Lagrange multipliers,

$$\sum_{i=1}^{N} \sum_{\sigma} \frac{\delta}{\delta \phi_i^*(\mathbf{r}\sigma)} \left[E^{HF}[\phi_i(\mathbf{r}\sigma)] - \varepsilon_i \left(d^3r |\phi_i(\mathbf{r}\sigma)|^2 - 1 \right) \right] = 0, \tag{1.5}$$

and leads to the HF equation,

$$\left[-\frac{1}{2}\nabla^2 + V_{ext}(\mathbf{r})\right]\phi_i(\mathbf{r}\sigma) + \sum_{j=1}^{N}\delta_{\sigma\sigma'}\left\{\int d^3r'\phi_j^*(\mathbf{r}'\sigma')\frac{1}{|\mathbf{r}-\mathbf{r}'|}\phi_j(\mathbf{r}'\sigma')\phi_i(\mathbf{r}\sigma)\right. \quad (1.6)$$

$$\left.-\int d^3r'\phi_j^*(\mathbf{r}'\sigma')\frac{1}{|\mathbf{r}-\mathbf{r}'|}\phi_j(\mathbf{r}\sigma)\phi_i(\mathbf{r}'\sigma')\right\} = \varepsilon_i\phi_i(\mathbf{r}\sigma),$$

or

$$\left[-\frac{1}{2}\nabla^2 + V_{ext}(\mathbf{r}) + \int d^3r'\frac{\rho(\mathbf{r}')}{|\mathbf{r}-\mathbf{r}'|}\right]\phi_i(\mathbf{r}\sigma) - \sum_j\int d^3r'\frac{\phi_j^*(\mathbf{r}'\sigma)\phi_j(\mathbf{r}\sigma)\phi_i(\mathbf{r}'\sigma)}{|\mathbf{r}-\mathbf{r}'|} \quad (1.7)$$

$$= \varepsilon_i\phi_i(\mathbf{r}\sigma),$$

with $\rho(\mathbf{r}') = \sum_j|\phi_j(\mathbf{r}')|^2$. It is to be noted that the exchange interaction is between the orbitals having the same spins. This nonlocal single particle equation needs to be solved self-consistently. The last two terms in the LHS are the classical and exchange potentials seen by the ith electron. The solution of the HF equation results in a set of orthonormal orbitals with corresponding eigenvalues, and the HF ground state wavefunction can be formed from these orbitals through the Slater determinant Eq.(1.2). The above integro-differential equation Eq. (1.8) need to be solved solved iteratively as the terms present in the left hand side need the orbitals which are yet to be determined. The numerical solution to the HF equation is restricted to the systems where one can separately write the 1D radial equation. To solve the HF equation for molecules, Roothaan in 1951 proposed to use a set of atom centered basis functions in expanding the Hartree-Fock orbitals.[3] Employing the determinantal wavefunction, only the Pauli correlation between electrons is taken care. However, the most important Coulomb correlation that affects the movement of electrons is missing in the Slater determinant, hence in the HF approach. The Coulomb correlation can be included in the many-body approach by changing the single determinant type representation of wavefunction. The solution of HF equation gives information about unoccupied ϕ_i along with the N occupied orbitals. Both the occupied and unoccupied states form a complete basis in one-particle Hilbert space and the combination of all

determinants leads to complete basis for N-particle Hilbert space. Forming the correlated wavefunction from the combination of single determinants, higher order wavefunction methods such as, Møller-Plesset perturbation theory, configuration interaction, coupled cluster method have been developed and are more accurate. But the computational cost of these methods are very high and depends exponentially on the size of basis sets used. So, for cost effective calculation of large systems, one has to include Coulomb correlation in some other way to the HF exact exchange without hindering the ability of self-interaction correction. Though the HF method is computationally favourable than higher order correlated methods, it needs to be avoided for larger systems as the number of basis sets increases rapidly with electrons and hence the computational time also increases. The remedy for such problems is the density functional theory in which one deals with the density instead of many-body wave function with 3N number of degrees of freedom and can calculate quantum chemistry and solid state properties with satisfactory accuracy and computational efficiency.

1.1   Basic Theorems and Foundations of Density Functional Theory

The first density-based method was proposed long back in 1927 by Thomas and Fermi[4,5] to solve inhomogeneous electron gas system without considering any electron-electron interaction. This method approximates the kinetic energy functional in terms of five-third power of the electron density with appropriate constant. This method was extended by Dirac in 1930, in which only density-dependent exchange interaction is added and is formally known as Thomas-Fermi-Dirac approximation. The above-mentioned methods are unable to bind molecules and do not form accurate shell structures of atoms, missing necessary physics and chemistry. Though these methods are not very effective in physical chemistry and material applications, they put forth ideas of movement of interacting electrons in an external effective potential and solving the many-body Schrödinger equation with density. However, a clear connection between the wavefunction method and

the density-based solution was not clearly established. That leads to a question whether a complete description of electronic structure is possible through only the many-body density. An attempt to find the answer became the starting point for the modern-day DFT.

1.1.1 The Hohenberg-Kohn formulation

1.1.1.1 Density as a basic variable

Starting with a system of interacting electrons under an external potential $v_{ext}(\mathbf{r})$, and only Coulomb interaction, the Hamiltonian operator is written as Eq. (1.1). It is clear that, for the many-body ground state wavefunction *Psi*, the ground state density is the functional of external potential. And Hohenberg-Kohn[6] proved that the reverse relation is also true, i.e., "*the external potential is also a unique functional of the ground state density*". It implies that any two external potentials differ by more than a constant will not have a simultaneous ground state wavefunction. The proof of this theorem is by *reductio ad absurdum* way. Let us assume that two external potentials v_{ext} and $v'_{ext} \neq v_{ext}$(or $v'_{ext} - v_{ext} = const$) give rise to same ground state density ρ with corresponding ground state wavefunctions Ψ and Ψ'. So, we write two Schrödinger equations,

$$H|\Psi\rangle = (T + V_{ext} + U)|\Psi\rangle = E_0|\Psi\rangle, \tag{1.8}$$

and

$$H'|\Psi'\rangle = (T + V'_{ext} + U)|\Psi'\rangle = E'_0|\Psi'\rangle, \tag{1.9}$$

Using the minimal property, we get

$$E'_0 = \langle\Psi'|H'|\Psi'\rangle < \langle\Psi|H'|\Psi\rangle \tag{1.10}$$

Now adding and subtracting v_{ext} in the right hand term, we have

$$E'_0 < E_0 + \langle\Psi|[V'_{ext} - V_{ext}]|\Psi\rangle. \tag{1.11}$$

If we interchange the primed and unprimed quantities, we get

$$E_0 < E_0' + \langle \Psi' | [V_{ext} - V_{ext}'] | \Psi' \rangle. \tag{1.12}$$

Imposing our assumption of both Ψ and Ψ' give rise to a density ρ, and adding above Eq.(1.11) and Eq.(1.12), we get

$$E_0' + E_0 < E_0 + E_0' \tag{1.13}$$

Such contradiction arises from our assumption that the densities are the same. Thus there exist a particular v_{ext} for a ground state density, and they are uniquely mapped to each other. So, from the density, we can get all the quantities present in the Hamiltonian, and hence all the properties derivable from the Hamiltonian. Now, one question arises that whether any well behaved density that integrates to a positive finite value N will have corresponding potential $v(\mathbf{r})$. If their exist such potential then the density is called v-representable density. However, there also exist well-behaved densities which integrate to the correct particle numbers and are not v-representable, those are called N-representable densities.

1.1.1.2 Universal functional and variational principle

Now, let's define a density functional F[ρ] consisting of only kinetic and interaction energies,

$$F[\rho] = \langle \Psi[\rho] | T + U | \Psi[\rho] \rangle. \tag{1.14}$$

This functional F[ρ] is universal functional of density and does not depend explicitly on the number of particles and the external potential. For any given external potential $v(\mathbf{r})$ the total energy functional can be written as,

$$E[\rho] = F[\rho] + \int d^3 r v(\mathbf{r}) \rho(\mathbf{r}). \tag{1.15}$$

One important conclusion is extracted from the HK theorem that for the exact ground state density $\rho(\mathbf{r})$, above Eq.(1.15) will give the ground state energy $E[\rho]$. And energy $E'[\rho']$ corresponding to any trial density $\rho'(\mathbf{r})$ is greater than that of $E[\rho]$. This variational method corresponding to density can be proved as follows.

Let's consider a N particle system with an external potential $v(\mathbf{r})$, corresponding ground state density $\rho(\mathbf{r})$, and true ground state wavefunction Ψ. For any other wavefunction Ψ' that correspond to same number of electrons, we can write

$$E_v[\Psi'] = F[\rho'] + \int d^3 r v(\mathbf{r})\rho'(\mathbf{r}) > E_v[\Psi] = F[\rho] + \int d^3 r v(\mathbf{r})\rho(\mathbf{r}) \qquad (1.16)$$

or $E_v[\rho'] > E_v[\rho]$. So, with the help of wavefunctions, it is proved that we can get ground state energy from the true ground state density, for a given external potential. The minimization of energy in ρ is easier in comparison to wavefunction. Now using the variational principle in terms of density and the electron number constraint, the stationary principle can be written for the ground state as:

$$\delta\left\{E[\rho] - \mu\left[\int \rho(\mathbf{r})d^3 r - N\right]\right\} = 0 \qquad (1.17)$$

which leads to the Euler-Lagrange equation,

$$\frac{\delta E[\rho]}{\delta \rho(\mathbf{r})} = v(\mathbf{r}) + \frac{\delta F[\rho]}{\delta \rho(\mathbf{r})} = \mu, \qquad (1.18)$$

with chemical potential μ. So, with the true ground state density, we only need the exact form of the universal functional F to get the exact ground state chemical potential. However, the exact density functional form of the universal functional is still far from reach. Now, question arises that though ground state density and wavefunction are uniquely mapped, how to get the wavefunction from the density? We address this question in the next section.

1.1.2 Constrained-Search Formulation

It is obvious to get the density from corresponding wavefunction, but the reverse relation is not transparent. A density can be produced from infinite number of antisymmetric wavefunctions, but the true ground state wavefunction which will lead to ground state density need to be identified. For this Levy-Lieb[7] constrained search approach is followed. Let's consider only those antisymmetric wavefunctions Ψ_{ρ_0} that give density ρ_0 and these wavefunctions are different from the true ground state wavefunction Ψ_0 that correspond to ground state energy E_o. So, we can write,

$$E_0 = \langle \Psi_0 | \hat{H} | \Psi_0 \rangle \leq \langle \Psi_{\rho_0} | \hat{H} | \Psi_{\rho_0} \rangle, \tag{1.19}$$

where the N particle Hamiltonian $\hat{H} = \hat{T} + \hat{V}_{ee} + v(\mathbf{r})$. The external potential energy arising from both the sides are same. Then, we can write,

$$\langle \Psi_0 | \hat{T} + \hat{V}_{ee} | \Psi_0 \rangle \leq \langle \Psi_{\rho_0} | \hat{T} + \hat{V}_{ee} | \Psi_{\rho_0} \rangle \tag{1.20}$$

So, we get the ground state universal functional $F[\rho_0]$ by searching over the entire antisymmetric wavefunction and constrained to the wavefunctions that leads to exact ground state density ρ_0. Or,

$$F[\rho_0] = \langle \Psi_0 | \hat{T} + \hat{V}_{ee} | \Psi_0 \rangle = \min_{\Psi \to \rho_0} \langle \Psi | \hat{T} + \hat{V}_{ee} | \Psi \rangle. \tag{1.21}$$

This minimization can be extended to any *N*-representable densities and the ground state density can be obtained with following two step procedure,

$$E_0 = \min_{\Psi} \left\{ \langle \Psi | \hat{T} + \hat{V}_{ee} | \Psi \rangle + \int d^3 r v(\mathbf{r}) \rho(\mathbf{r}) \right\} \tag{1.22}$$

$$= \min_{\rho} \left\{ \min_{\Psi \to \rho} \left[\Psi | \hat{T} + \hat{V}_{ee} | \Psi \rangle + \int d^3 r v(\mathbf{r}) \rho(\mathbf{r}) \right] \right\}$$

In the above Eq.(1.23), first we minimize over the constrained wavefunctions that give ρ, and then the outer minimization is over all the obtained ρ. Now, using Eq.(1.21), we can write,

$$E_0 = \min_{\rho}\{F[\rho] + \int d^3 r v(\mathbf{r})\rho(\mathbf{r})\} \tag{1.23}$$

So, one can get the ground state energy by minimizing the energy functional with density and the ground state density will correspond to the ground state energy. From all the above discussions, it is clear that, we can use the density as a basic variable to express all the energy terms present in the Hamiltonian, and can get the ground state energy by minimizing with respect to the three-dimensional density in stead of 3N-dimensional many-body trial wavefunction. However, one obstacle still stands in the form of the universal functional. From the Thomas-Fermi model a rough approximation can be followed for both the kinetic energy and electron-electron interaction energies. But this lies far from applying the theory efficiently to practical systems. The Kohn-Sham formalism[8] helps to apply the HK theorem to practical systems with information of the universal functional and solving the many-body problem with density as the basic variable.

1.2   Kohn-Sham Formalism

Before the formulation of advance density functional theory, starting from the Hartree model the electronic structure calculation of atoms are done by considering the movement of electrons in an effective external potential. Such single particle model allows to interpret a eigenfunction as the state of an electron. An electron moving in the Hartree potential V_H can be written as,

$$[-\frac{1}{2}\nabla^2 + V_H(\mathbf{r})]\phi_i = \varepsilon_i\phi_i, \tag{1.24}$$

where $V_H(\mathbf{r}) = -\frac{Z}{\mathbf{r}} + \int \frac{\rho(\mathbf{r}')}{\mathbf{r}-\mathbf{r}'}d\mathbf{r}'$, Z is the atomic number, and ϕ_i is the ith electron wavefunction. The ground state mean density associated with the the wavefunction is

$$\rho(\mathbf{r}) = \sum_{i=1}^{N} |\phi_i(\mathbf{r})|^2.$$

The Schrödinger Eq.(1.24) treats the electrons as non-interacting particles and the effect of interactions are included in V_H. It was observed that the Hartree method is much better than that of Thomas-Fermi method for ground state properties[9] and these methods differ from each other in terms of treating the kinetic energy. So, Kohn and Sham proposed a model to treat electrons as non-interacting particles staying within Hohenberg-Kohn density based formalism by changing the interacting kinetic energy to non-interacting kinetic energy. As a result, we deal with a fictitious non-interacting electronic system having same electron number and electron density as the actual interacting system. The energy functional for the fictitious system is written as,

$$E_{KS}[\rho(\mathbf{r})] = T_s[\rho(\mathbf{r})] + \int d^3r v_{ext}(\mathbf{r})\rho(\mathbf{r}) + \frac{1}{2}\int d^3r d^3r' \frac{\rho(\mathbf{r})\rho(\mathbf{r}')}{|\mathbf{r}-\mathbf{r}'|} + E_{XC}[\rho(\mathbf{r})]. \quad (1.25)$$

Where

$$T_s[\rho(\mathbf{r})] = \sum_{i=1}^{N} \langle \phi_i | -\frac{1}{2}\nabla_i^2 | \phi_i \rangle \quad (1.26)$$

is the kinetic energy for density distribution $\rho(\mathbf{r})$ of the noninteracting system, and $\{\phi_i\}$ are Kohn-Sham orbitals. The last term is known as exchange-correlation(XC) energy functional. The $E_{XC}[\rho(\mathbf{r})]$ contains a part of the V_{e-e} except the classical coulomb interaction and effects of residual kinetic energy,

$$E_{XC}[\rho(\mathbf{r})] = T[\rho(\mathbf{r})] - T_s[\rho(\mathbf{r})] + V_{e-e}[\rho(\mathbf{r})] - J[\rho(\mathbf{r})] \quad (1.27)$$

with $J[\rho(\mathbf{r})]$ being the classical interaction part. The Euler-Lagrange equation corresponding to the KS Eq.(1.25) with electron number constraint similar to Eq.(1.18), written

as

$$\mu = v_{eff}(\mathbf{r}) + \frac{\delta T_s[\rho]}{\delta \rho(\mathbf{r})}, \tag{1.28}$$

and the Kohn-Sham effective potential contains,

$$v_{eff}(\mathbf{r}) = v_{ext}(\mathbf{r}) + \int \frac{\rho(\mathbf{r}')}{|\mathbf{r} - \mathbf{r}'|} + v_{XC}(\mathbf{r}). \tag{1.29}$$

The XC potential is defined as $v_{XC}(\mathbf{r}) = \delta E_{XC}[\rho]/\delta \rho(\mathbf{r})$. So, one can solve the fully interacting system via noninteracting electrons moving in an effective potential v_{eff} by solving single particle KS equations,

$$[-\frac{1}{2}\nabla^2 + v_{eff}(\mathbf{r})]\phi_i(\mathbf{r}) = \varepsilon_i \phi_i(\mathbf{r}), \tag{1.30}$$

with

$$\rho(\mathbf{r}) = \sum_{i=1}^{N} |\phi_i(\mathbf{r})|^2. \tag{1.31}$$

The effective potential depends on $\rho(\mathbf{r})$ and the density is derived from $\phi_i(\mathbf{r})$. So, the KS equation needs to be solved self-consistently. Starting from a guessed density, $v_{eff}(\mathbf{r})$ is modeled from Eq.(1.29). Then, this effective potential is used in KS equation Eq.(1.30) to get $\phi_i(\mathbf{r})$ and hence, the new density. The equations from Eq.(1.28) to Eq.(1.31) collectively represent the KS formalism. So, we have to construct an effective single particle potential for the fictitious noninteracting system, which will lead to the same density as the complete interacting system. But, the Slater determinant wavefunction made from the KS orbitals ϕ_i is different from the true interacting wavefunction, and the KS energies and orbitals have no direct physical meaning except the energy of the highest occupied orbital. The negative of the highest occupied orbital energy($IP = -\varepsilon_N$) is recognized as the ionization potential of the interacting system. In addition, Janak's theorem provides an important observation about the eigen values. It proves the derivative of total energy with respect to the occupation number of a particular eigen state gives the KS eigenvalue of this state($\delta E/\delta n_i = \varepsilon_i$).

In principle, the KS DFT is exact in the sense that it includes all the many-body

interactions. However, the accuracy of the calculation depends completely on the approximated form of the XC energy functional and the potential. In search of more accurate XC functional, a lot of research have been carried out and it remains as one of the present day research interest in the DFT community.

1.3 Approximations for Exchange-Correlation

From the advent of KS formalism, many level of approximations have been proposed starting from the simple electron density dependent E_{XC} to complicated non-local corrected methods. All these approximations can be arranged in the Jacob's ladder of XC functionals[10] that goes from Hartree method to heaven of accuracy methods with an error up to 1cal/mol. Out of large number of developed functionals, we will only discuss more successful functionals and the series of functionals that are very effective for new development.

1.3.1 Local Density Approximation (LDA)

The exchange energy form derived by Dirac for homogeneous electron gas is used in the density functional method to treat completely interacting practical system. Only density dependent simple form of the exchange energy functional presented as,

$$E_X^{LDA}[\rho] = \int d^3r \rho \varepsilon_x^{unif}[\rho], \tag{1.32}$$

with $\varepsilon_x^{unif} = -\frac{3}{4}(\frac{3}{\pi})^{1/3}\rho^{1/3}$ being the LDA exchange energy density. This form of exchange energy does not contain any empirical parameter to include any physical constraint, and the coefficient present is completely from the properties of homogeneous electron gas (HEG). Corresponding exchange potential $v_x = -(\frac{3}{\pi})^{1/3}\rho^{1/3}$ can be used to form the KS effective potential to solve the KS equation. Though LDA enjoyed a lot of early success, one important failure can be observed by using exponentially decaying density. For a density of the form $\rho(\mathbf{r}) \sim e^{-\alpha r}$, the LDA exchange potential follows

$v_x^{LDA}(\mathbf{r}) \sim e^{-\alpha r/3}$. Such exponential decay of the potential in the asymptotic region contradicts the exact Coulombic behavior $-1/r$ and leads to incorrect binding of molecules. The exchange energies of atoms are underestimated by the LDA to a large extent. Unlike the exchange, the derivation of LDA correlation energy functional is not straight forward. But the forms at two extreme conditions high density limit ($\rho \to \infty$), and low density limit ($\rho \to 0$) can be extracted from the random phase approximation (RPA), and different ways have been proposed to interpolate these extreme cases for intermediate region. One leading correlation energy functional in this direction is given by Vosko, Wilk, and Nusair (VWN),[11] which successfully preserves both high, and low density limiting conditions. The correlation energy of LDA usually overestimates the correlation energy. The underestimation by the exchange and the overestimation by the correlation energy causes the error cancellation for a particular calculation. As, the approximation is based on HEG system, it is expected that the accuracy of the LDA E_{XC} will be better in case of slowly varying densities. But the results of XC energies on the application of LDA to practical systems is far from the exact values, so more modifications are needed to model appropriate XC functionals.

1.3.2 Generalized Gradient Approximation (GGA)

Before going to the GGA functionals, we give a short note on gradient expansion approximations(GEA) of density functionals. Though the GEA is not successful in comparison to LDA, it helps in the development of the next rung functionals. The GEA is the earliest semilocal approximation that considers a small variation in the density and treat it as a perturbation to the HEG. Applying the slow variation of density, the exchange energy functional as obtained by Svendsen et al.[12]

$$E_x^{GEA} = \int d^3 r \varepsilon_x^{HEG}[\rho]\left\{1 + \frac{10}{81}p + \frac{146}{2025}\left[q^2 - \frac{5}{2}qp + Dp^2\right]\right\}. \tag{1.33}$$

The gradient and Laplacian of density dependent parameters $p = |\nabla\rho|^2/[4(3\pi^2)^{2/3}\rho^{8/3}]$ and $q = \nabla^2\rho/[4(3\pi^2)^{2/3}\rho^{5/3}]$. An adjustable parameter D is an advantage for higher rung

functionals that can be fixed accordingly. This form of the exchange functional having gradient expansion up to 4th order acts as a constraint that all the higher rung functionals should satisfy to ensure the exact slowly varying density limit of the exchange energy. Assuming the higher order expansion terms have comparative very small effect after second order in gradient, the second order gradient expansion(GE2) improves the exchange energy of atoms over LDA exchange. Whereas, the inclusion of second order gradient expansion in the correlation energy leads to positive correlation energies[13]. Overall, GE2 faces serious issues such as; (i) the underlying exchange potential diverges for exponentially decaying density, (ii) the exchange energy of atoms improves over the LDA but the correlation energy become positive (wrong sign), (iii) there is no improvement over the LDA in case of solids. So different gradient dependent XC functionals have been proposed to avoid such shortcomings of GE2 and for more accurate treatment within semilocal DFT.

The approximated functionals in GGA level use the density and its gradient as ingredients, and a general representation of the exchange energy functional can be followed as,

$$E_{XC}^{GGA}[\rho] = \int d^3r\rho(\mathbf{r})\varepsilon_{XC}^{GGA}(\rho(\mathbf{r}),\nabla\rho(\mathbf{r})) \qquad (1.34)$$

Now, we discuss some well-known GGA functionals and the physical idea behind the construction of these functionals.

To get an appropriate asymptotic behavior of the exchange potential, the well known exchange functional is B88,[14] proposed by Becke on 1988. The form of the functional is given by,

$$E_x^{B88} = E_x^{LDA} - \beta \sum_\sigma \int d^3r\rho_\sigma^{4/3} \frac{x_\sigma^2}{1+6\beta x_\sigma sinh^{-1}x_\sigma}. \qquad (1.35)$$

Here, the parameter $\beta = 0.0042$ is fixed from the exact values of six noble gas atoms, and the dimensionless reduced density gradient $x_\sigma = |\nabla\rho_\sigma|/\rho_\sigma^{4/3}$. The exchange energies of atoms of B88 functional improves a lot over LDA values and agree well with corresponding exact exchange energies. For example, considering the exchange energy of transition metal zinc, LDA=-65.64, B88=-69.86, whereas exact exchange energy is -69.64 a.u.. Other than Becke's functionals, a successful series of XC functionals have been proposed

by John. P. Perdew based on gradient expansion of exchange hole with the real space cut off technique.[15,16] In terms of the enhancement factor the exchange energy functional is written in the form,

$$E_x[\rho] = \int d^3r\rho\varepsilon_x^{unif}F_X(s).$$ (1.36)

The uniform exchange energy density is given by Eq.(1.32), and $F_X(s)$ is called the enhancement factor and for all GGA type functionals, it depends on the reduced density gradient $s = |\nabla\rho|/2k_F\rho$, where $k_F = (3\pi^2\rho)^{2/3}$ is the Fermi wave vector. Now, the main task is to construct the enhancement factor by imposing known constraints. One of the most important constraint is given by Eq.(1.33), i.e., for slowly varying density, the F_X should follow the term present within the curly bracket. Now, we discuss the construction of the most used XC functional popularly known as PBE-GGA(Perdew-Burke-Ernzerhof).[17] The exchange enhancement factor for PBE functional follows

$$F_x(s) = 1 + \kappa - \frac{\kappa}{1 + x/k},$$ (1.37)

where, $x = \mu s^2$. The enhancement factor having this form recovers the LDA linear response, i.e., at $s \to 0$,

$$F_x(s) = 1 + \mu s^2,$$ (1.38)

where $\mu = 0.21951$ is fixed from the correlation energy to cancel gradient dependent terms in the LDA limit. Also, such form of exchange retains the LDA as the first term. Now, another parameter κ is fixed from imposing the tight-bound constraint of the exchange energy or the exchange enhancement factor. The exchange energy should obey the Lieb-Oxford bound[18]

$$E_x \geq -1.679 \int d^3r\rho^{4/3}$$ (1.39)

Following the above constraint for exchange energy, the enhancement factor should follow $F_x \leq 1.804$ which leads to $\kappa = 0.804$. To construct exchange energy functionals, the constraints such as recovering LDA exchange, exact small s behavior, and strong upper bound for F_x are very important. For example, changing the value of param-

eter μ present in Eq.(1.39) to the exact value from the gradient expansion Eq.(1.33), $\mu^{GE} = 10/81 \approx 0.1235$, PBEsol[19] XC was proposed. The correlation energy functional for such type of exchange energies are proposed by adding density gradient dependent functions to the LDA correlation and imposing constraints, e.g., density scaling, variation of density in slow and rapid conditions, and recovering the uniform electron gas limit. Apart from this type of approximations, where new gradient dependent terms are added to the LDA to obey physical constraints, other methods are proposed based on interaction between the density and its exchange hole. The exchange energy of such type of functionals are written as,

$$E_x = -\frac{1}{2} \int d^3r \rho(\mathbf{r}) \int d^3u \frac{\rho_x(\mathbf{r},\mathbf{r}+\mathbf{u})}{u},\tag{1.40}$$

where $\rho_x(\mathbf{r},\mathbf{r}+\mathbf{u})$ is the Fermi hole or exchange hole, and $\mathbf{u} = \mathbf{r} - \mathbf{r}'$. The exchange hole is the exchange charge density that surrounds an electron within which no other electrons can come. The conventional exchange hole integrates to exactly one electron deficiency, i.e., $\int d^3u \rho_x(\mathbf{r},\mathbf{r}+\mathbf{u}) = -1$, and the exchange energy only depends on the spherical average of the exchange hole. These are the constraints to be satisfied by the model exchange hole. Also, Becke in 1983[20] proposed a constraint for short-range behavior of the exchange hole up to second order in u,

$$\langle \rho_x(u) \rangle = \rho + \frac{1}{6} \{ \nabla^2 \rho - 2\tau + \frac{1}{2} \frac{(\nabla \rho)^2}{\rho} \} u^2 + ...\tag{1.41}$$

where $\tau = \sum_i |\nabla \phi_i|^2$ is the kinetic energy density. In all GGA type exchange energy functionals, the kinetic energy density is replaced by its density dependent expansion form,

$$\tau = \tau^{unif} + \frac{|\nabla \rho|^2}{72\rho} + \frac{\nabla^2 \rho}{6},\tag{1.42}$$

with the HEG kinetic energy density $\tau^{unif} = (3/10)(3\pi^2)^{2/3}\rho^{5/3}$. Both Eq.(1.41) and Eq.(1.42) are very useful and we will often recall these equations in other sections of the thesis. Based on the exchange hole model Becke proposed two different functionals in 1983[20] and 1986[21] that are very effective in comparison to the LDA. Throughout the

thesis, we will use the concept of exchange hole and generalized coordinate transformed exchange hole to construct new XC functionals. Though GGAs improve over LDA and the accuracy is acceptable in most of the cases, the errors in comparison to experimental methods are still high in predicting atomization energies(mean absolute error(MAE) of 15.17 kcal/mol for G2/148 test set),[22] barrier heights (MAE of 9.32 kcal/mol for BH76), ionization potential (MAE of 3.47 kcal/mol for IP13 test set),[23] electron affinity (MAE 2.64 kcal/mol for the EA13 test set)[23] etc. The next rung or the third rung of Jacob's ladder is dedicated to meta-GGA (mGGA) type XC functionals,[24,25,26] which use the kinetic energy density (τ) as an ingredient in addition to density and gradient of density. The idea of τ dependent functionals was there from 1983 when the Taylor expansion of the exchange hole at the small interelectronic distance limit was derived(Eq. (1.41)). The practical implication of these functionals was made possible by the development of the generalized Kohn-Sham (gKS) scheme.[27] The use of the additional ingredient, τ, allows the functional to satisfy more number of constraints. In addition, using τ, different type of iso-orbital indicators can be formed to recognize various bonding regions.[28] In the next section, we discuss the construction of mGGA type XC functionals and the advantages of such functionals.

1.3.3   Meta-Generalized Gradient Approximation (MGGA)

As discussed before, in addition to electron density and the gradient of density, the MGGA functionals use another natural ingredient, the kinetic energy density

$$\tau(\mathbf{r}) = \sum_i^{occup} |\nabla\phi_i(\mathbf{r})|^2. \tag{1.43}$$

Preserving all the good qualities of PBE functional, Perdew-Kurth-Zupan-Blaha(PKZB)[29] functional was constructed over the form of PBE. For such an exchange energy functional, the Eq 1.36 follows

$$E_x^{MGGA}[\rho] = \int d^3r\rho\varepsilon_x^{unif}F_X(\rho,\nabla\rho,\tau). \tag{1.44}$$

The form of the enhancement factor for PKZB is the same with Eq.(1.37) but with a different Laplacian of density dependent form of x given as,

$$x^{PKZB} = \frac{10}{81}p + \frac{146}{2025}\tilde{q}^2 - \frac{73}{405}\tilde{q}p + \left[D + \frac{1}{\kappa}\left(\frac{10}{81}\right)^2\right]p^2. \tag{1.45}$$

Such intense form of x is chosen to recover the exact behavior of the exchange energy functional for slowly varying density up fourth order in ∇ as given in Eq.(1.33). But the form of $\tilde{q}$ is different from the original reduced Laplacian of density q present in Eq.(1.33). The form of q is transformed to

$$\tilde{q} = \frac{3\tau}{2(3\pi^2)^{2/3}\rho^{5/3}} - \frac{9}{10} - \frac{p}{12} \tag{1.46}$$

such that, the new form $\tilde{q}$ goes to q at slowly varying limit and the divergence of q at a nucleus is checked. The value of parameter $\kappa = 0.804$ is the same as in PBE, and the value of $D = 0.113$ is fixed by minimizing the error in the atomization energies. The atomization energies and the surface energies are improved in compare to PBE but the poor bond length and poor description of hydrogen bonded systems open the room for further improvement. Following the same framework as PKZB, the Tao-Perdew-Staroverov-Scuseria (TPSS)[30] functional was proposed by modifying the form of x present in Eq.(1.37). Defining a different form of q as,

$$\tilde{q}_b = \frac{9(\alpha - 1)}{20[1 + b\alpha(\alpha - 1)]^{1/2}} + \frac{2p}{3}, \tag{1.47}$$

the form of x is changed to

$$x^{TPSS} = \left\{ \left[\frac{10}{81} + c\frac{z^2}{(1+z^2)^2}\right]p + \frac{146}{2025}\tilde{q}_b^2 - \frac{73}{405}\tilde{q}_b\sqrt{\frac{1}{2}\left(\frac{3}{5}z\right)^2 + \frac{p^2}{2}} + \frac{1}{\kappa}\left(\frac{10}{81}\right)^2 p^2 \right.$$
$$\left. + 2\sqrt{e}\frac{10}{81}\left(\frac{3}{5}z\right)^2 + e\mu p^3 \right\}/(1 + \sqrt{e}p)^2. \tag{1.48}$$

The form of $\tilde{q}_b$ is chosen in such a way that for $b = 0$, $\tilde{q}_b$ goes to $\tilde{q}$ of PKZB. Also, two iso-orbital indicators $z = \tau^W/\tau \leq 1$ and $\alpha = (\tau - \tau^W)/\tau^{unif}$ are introduced. Here, $\tau^W = |\nabla\rho|^2/(8\rho)$ is the Weizsacker kinetic energy density. The parameters $c = 1.59096$ and $e = 1.537$ are fixed by minimizing the ground state exchange energy of hydrogen atom, whereas $b = 0.40$ is fixed to make the enhancement factor vary monotonically with s. Similar to the way of PBEsol functional construction, revTPSS[31] functional was proposed by redefining the parameters and modifying $cz^2/(1+z^2)^2$ present within x to $cz^3/(1+z^2)^2$. The post revTPSS functionals extensively use the properties of iso-orbital indicator α. The values of α correspond to different chemical environments as, for single orbital region $\alpha = 0$, for slowly varying region $\alpha \approx 1$, and for non-covalent bonding $\alpha \geq 1$. The revTPSS functional recovers the exact limits for $\alpha = 0$ and $\alpha \approx 1$ regions, but there is no function present in the functional form to guide it for $0 < \alpha < 1$. So recovering these limiting conditions and interpolating $\alpha = 0$ and $\alpha \approx 1$ regions, new advance density functionals[32,33,34,35] are proposed. The most successful form in this genre is the strongly constrained and appropriately normed (SCAN)[34] meta-GGA functional. The form of the enhancement factor of SCAN is given by,

$$F_x^{SCAN}(s, \alpha) = [h_x^1(s, \alpha) + f_x(\alpha)\{h_x^0 - h_x^1(s, \alpha)\}]g_x(s). \qquad (1.49)$$

Here, the form of $h_x^1(s, \alpha)$ is chosen to recover the fourth-order gradient expansion of exchange that is necessary for $\alpha \approx 1$. For $\alpha = 0$, the strongly tight bound to the enhancement factor($F_x \leq 1.174$) is imposed, which implies, $F_x(s, \alpha = 0) = h_x^0 g_x(s)$ with $h_x^0 = 1.174$, and $g_x(s) = 1 - exp[-a_1 s^{-1/2}]$. The function $f(\alpha)$ is the switching function that interpolates two limiting conditions and makes sure the smooth transition. Moreover, the SCAN functional is constructed by imposing six constraints to the exchange, six constraints to the correlation, and five constraints to both together XC energy. Again, to make SCAN functional more numerical stable, recently, regularized -SCAN(rSCAN)[36] functional has been proposed by modeling the switching function as a polynomial of α. But the numerical stability model comes with a cost of accuracy.[37] And very recently, the r[2]SCAN[38] functional is being proposed that claims to solve the numerical instability

problem with retaining the accuracy of parent SCAN functional.

As discussed in the GGA section, the meta-GGA exchange energies can also be formed from the concept of exchange hole Eq.(1.40). Examples of successful meta-GGA exchange functionals in this group are generalized density matrix expansion (gDME),[39] Voorhis-Scuseria 1997(VS97),[40] VS98,[26] M06-L,[41] and recently proposed Tao-Mo(TM).[42] All these functionals are made by forming the exchange holes from the DME. We will not show the derivation of the 3D DME, instead, the 2D version of the DME that is derived in parallel to 3D will be discussed in next chapter. Moreover, the idea of recent successful TM functional is to construct XC functional by interpolating energy functional for the compact density and the slowly varying density. For compact density, the enhancement factor derived from the DME is suitable, whereas for slowly varying density, the enhancement factor should follow the fourth order gradient expansion,

$$F_x^{TM}(p,z,\alpha) = wF_x^{DME} + (1-w)F_x^{sc}. \tag{1.50}$$

Where, $w = \frac{z^2 + 3z^3}{(1+z^3)^2}$ is the interpolating function, and F_x^{DME} is the enhancement factor derived from the DME, and F_x^{sc} is the enhancement factor used for the slowly varying correction of density. The form of F_x^{sc} is derived in accordance with Eq.(1.33) and given as,

$$F_x^{sc} = \left\{ 10 \left[\left(\frac{10}{81} + \frac{50}{729}p \right) p + \frac{146}{2025}\tilde{q}_0^2 - \frac{73\tilde{q}_0}{405} \left(\frac{3z}{5} \right) (1-z) \right] \right\}^{1/10}, \tag{1.51}$$

with $\tilde{q}_0$ is same as Eq.(1.47) for $b = 0$. The DME part of the F_x is given by,

$$F_x^{DME}(p,\alpha) = \frac{1}{f^2} + \frac{7R}{9f^4} \tag{1.52}$$

with $R = 1 + 595(2\lambda - 1)^2 \frac{p}{54} - [\tau - 3(\lambda^2 - \lambda + 1/2)(\tau - \tau^{unif} - |\nabla\rho|^2/72\rho)]/\tau^{unif}$ and $f = [1 + 10(70y/27) + \beta y^2]^{1/10}$. Here, $y = (2\lambda - 1)^2 p$ and λ is the parameter used to transform the exchange hole to make the exchange hole more flexible without hindering the form of the exchange energy functional. The application of these GGA and meta-

GGA type density functional can be assessed from various properties of periodic solids as discussed in recent papers by Jana et al.[43,44] It is shown that no XC functional is able to give the least error for all the properties of solids and all meta-GGAs do not improve over GGAs. For 3d transition metals PBE is better that meta-GGAs. For lattice constants the TM functional is the best, whereas SCAN is the best for bulk moduli, cohesive energies, and band gaps. For molecular properties including weak bonded systems, TM functional is the best.[45,46] Though the semilocal functionals have acceptable accuracy in predicting energies, they are very poor describing ionization potential, electron affinity, proton affinity, barrier heights etc. The hybrid methods that use some part of exact exchange to the semilocal XC energy were emerged as the solution to these problems with additional computational cost.

1.3.4   Hybrid Treatment

Within the KS formalism, the addition of full HF exchange with the semilocal correlation does not attain the expected chemical accuracy.[47] A different parametric combination of semilocal exchange, HF exchange, and semilocal correlation was proposed by Becke known as B3PW91[48]

$$E_{XC}^{B3PW91} = E_{XC}^{LSDA} + a_0(E_X^{exact} - E_X^{LSDA}) + a_X \Delta E_X^{B88} + a_C \Delta E_c^{PW91}. \qquad (1.53)$$

Where, a_0, a_X, and a_C are parameters determined by fitting with the experimental data of atomization energies, ionization potentials, and electron affinities ($a_0 = 0.20$, $a_X = 0.72$, and $a_C = 0.81$). Other terms, E_X^{exact} is the exact exchange energy, E_X^{B88} is the B88 GGA exchange energy functional,[14] and E_c^{PW91} is the PW91 GGA correlation.[49] The Δ used behind the exchange and correlation is for optimum mixture of gradient correction. The conclusion is that the admixture of some part of the exact exchange increases the accuracy significantly. Since then, different approximations have been proposed by admixing other XC functionals with the exact exchange. One of the most successful methods is the

B3LYP hybrid functional[50] and the form of the XC functional is given as,

$$E_{XC}^{B3LYP} = a_{x0}E_X^{LSDA} + (1 - a_{x0})E_X^{HF} + a_{x1}\Delta E_X^{B88} + a_c E_c^{LYP} + (1 - a_c)E_C^{LSDA}, \quad (1.54)$$

with $a_{x0} = 0.20$, $a_{x1} = 0.72$, $a_c = 0.81$, and E_c^{LYP} is the LYP correlation.[51] Another well-known method that used the PBE XC functional with a quarter of exact exchange known as PBE0 functional.[52] These type of hybrid functionals are known as global hybrids as the fraction of exact exchange is constant all over the Coulomb interaction range r_{ij}. So, for a fraction 'a' of E_X^{HF}, the XC potential decays as $-a/r_{ij}$ instead of the correct behavior of $-1/r_{ij}$. The exact asymptotic decay of the potential is necessary for molecular complexes. To avoid such problems, the range-separation scheme[53] for the Coulomb interaction was proposed that uses the error function to separate the range of dominance of semilocal exchange and HF exchange. The Coulomb operator $\frac{1}{r_{ij}}$ is separated into short-range (SR) and long-range(LR) parts with the help of error functions as follows,

$$\frac{1}{r_{ij}} = \underbrace{\frac{erfc(\omega r_{ij})}{r_{ij}}}_{\text{SR}} + \underbrace{\frac{erf(\omega r_{ij})}{r_{ij}}}_{\text{LR}}, \quad (1.55)$$

with ω as a range-separation parameter. The long-range corrected hybrid functionals use HF in LR and complete density functional exchange in SR. A thorough discussion on the long-range corrected hybrid methods will be presented in Chapter 4 of this thesis. However, for solid-state systems that use periodic boundary conditions(PBC), the convergence of HF is an important issue. To avoid the divergence arising from Coulomb potential, Jochen et al proposed a model popularly known as Heyd-Scuseria-Ernzerhof(HSE).[54,55] The HSE model mixes the exact exchange only for the SR interactions. The form of the HSE model is written as,

$$E_{XC}^{HSE} = aE_X^{SR,HF}(\omega) + (1 - a)E_X^{SR,PBE}(\omega) + E_X^{LR,PBE}(\omega) + E_C^{PBE}. \quad (1.56)$$

The mixing parameter $a = 0.25$ and the screening parameter is fixed to $\omega = 0.15$. The derivation of the SR part of density functional will be discussed in Chapter 4. The SR

part of the HF exchange is calculated by multiplying the complementary error function $erfc(\omega r_{ij})$ to the HF exchange with appropriate value of ω. The dominance of such hybrid methods in the solid state properties can be found in Ref..[56] So far, we have discussed the construction of popular density functional methods that have been used in practical applications to predict properties of solids and molecular complexes, theoretically. However, there are many XC functionals that could not be discussed in the thesis and all those functionals can be found in LIBXC.[57,58]

Though there are many developments, there is always a space for further improvement on the approximations, and there are many fields that need improved methods. For this purpose, we focus on developing new methods or new approximations for XC interactions. We adopt the exchange hole model Eq.(1.40) to construct new XC functionals. In chapter 2, we show both empirical and non-empirical XC energy functionals in 2D. By modeling the 2D exchange holes from the 2D DME, these XC functionals are proposed for pure 2D systems. In chapter 3, we show the construction of a Laplacian free model of the exchange hole potential and the use of exchange hole potential in band gap calculations. In this chapter, we also discuss the demerits of using exchange-only potentials in case of mono-layer calculations and what can be possible alternate within semilocal DFT. Next, chapter 4 is dedicated to long-range corrected screened hybrid functionals. Here, we briefly discuss the technique to construct an appropriate exchange hole from any GGA type exchange energy functionals. We construct three type of exchange holes and using the exchange holes, new LC screened hybrid functionals are developed for molecular complexes. In the final chapter, we discuss the status of dispersion interaction in the DFT. We propose a model to address the long-range correlation. The model is assessed through some molecular and solid state systems having significant van der Waals interactions.

Chapter 2

Density Functional Theory in Two Dimensions

2.1 Introduction

Present day research interest in condensed matter physics or material science include lower dimensional quantum problems. Accuracy of solving such lower dimensional problems needs a flawless treatment of the dimensionality of the system. The two-dimensional systems that include semiconductor quantum dots(QDs), quantum Hall-devices, quantum point contact systems, restrict the movement of electrons in two-dimensions. If one wishes to study these systems within DFT, appropriate treatment of the dimension of these systems is essential. The unknown and approximated portion of the energy functionals, i.e., the exchange correlation energy functional also needs an appropriate treatment. In recent articles,[59,60,61] it is seen that the use of three-dimensional exchange-correlation functionals in pure two-dimensional quantum systems leads significant deviation from exact values. To address such dimensional cross-over problems, attempts have been made to construct exchange-correlation functionals[62,63,64] appropriate for quasi-2D systems. Parallel to the Jacob's ladder of energy functionals in three-dimensions, Jacob's ladder can be formed for two-dimensional approximated density functionals. Starting from LDA, that represents the first rung, the ladder goes to the heaven of calculation with very ac-

curate energies and densities of interacting systems. The pure 2D systems such as QDs have been studied by 2D-LDA exchange in combination with 2D-LDA correlation.[65] To incorporate the non-homogeneous effects of systems, GGA functionals and mGGA functionals[57,58] have been proposed in the last decade. The recent applications of some of these semilocal functionals in studying artificial graphene(AG)[66,67,68,69,70] encourage the development of new more accurate density functionals for 2D quantum systems. The AGs are engineered with appropriate quantum dot potential arranged in hexagonal lattices. The use of AGs has a lot of advantages including easy access to strong spin-orbit coupling regime, controllable inter-particle interaction, and designing and studying artificial defects and Dirac physics. To study these systems within 2D-DFT, it needs reliable exchange-correlation density functionals. This chapter is dedicated to the development of more accurate exchange-correlation energy functionals for above mentioned 2D systems.

We start the chapter with the density matrix expansion(DME) in two-dimensions that will be used to construct mGGA level exchange and correlation energy functionals. The advantages of DME to construct the functionals will be discussed along with the new possibilities of approximations to include electron-electron interaction. In the first part, we propose parameter-free exchange energy functionals using expressions of the DME up to second order. The efficiency of such simple form of functional is enhanced by replacing the homogeneous momentum with the statistically averaged kinetic energy density. Next, we explore the DME of exchange hole with use of generalized coordinate transformation, that allows us to play with the shape of exchange hole. With the help of such generalized exchange hole, we again propose three exchange functionals with appropriate parameterization. The Fermi momentum present in these functionals is modified with the inclusion of reduced density gradient and kinetic energy density to incorporate the inhomogeneity of the actual system. A suitable correlation functional for such parameterized exchange functional is modeled by incorporating the semi-local correction with the available 2D-LDA[65] correlation energy functional. In the last part, we propose a Colle-Salvetti type two-dimensional correlation energy functional for the general use with available exchange energy functionals. Extensive testing of these functionals are demonstrated by considering parabolic and Gaussian quantum dots (QD), by varying the confinement strength and

the confined particle number. All these developed functionals possess their own importance in describing these 2D systems, so, we discuss all these results thoroughly and individually. To validate the accuracy of these functionals a comparison with available previously developed functionals is essential and we present the comparison rigorously.

2.2 Density Matrix Expansion in 2-Dimensions

The DME method is a very successful strategy that has been used to construct analytic exchange energy functionals in three-dimensions.[26,39,40,71] The functionality of such suitable method needs to be explored in 2D. The exchange energy within DFT can be termed as the electrostatic interaction between the density of an electron at $\mathbf{r}$ and its exchange hole that surrounds the electron.[72] With this information the exchange energy in 2D is written as,

$$E_x = \frac{1}{2} \int \rho(\mathbf{r}) d^2r \int d^2r' \frac{\langle \rho_x(\mathbf{r}, \mathbf{r}') \rangle}{|\mathbf{r} - \mathbf{r}'|} \ . \tag{2.1}$$

Here, $\langle \rho_x(\mathbf{r}, \mathbf{r}') \rangle$ is the cylindrically averaged exchange hole in 2D. The exchange hole is a significant quantity, and is physically understandable. One such example is the system averaged exchange hole on top of the electron is proportional to the $\langle \rho \rangle$. This exchange hole can be expressed using the 1st order density matrix $\Gamma_1(\mathbf{r}, \mathbf{r}')$ and expressed as,

$$\langle \rho_x(\mathbf{r}, \mathbf{r}') \rangle = -\frac{\langle |\Gamma_1(\mathbf{r}, \mathbf{r}')|^2 \rangle}{2\rho(\mathbf{r})} \tag{2.2}$$

with

$$\Gamma_1(\mathbf{r}, \mathbf{r}') = 2 \sum_{i=1}^{occu} \phi_i^*(\mathbf{r}) \phi_i(\mathbf{r}') \ . \tag{2.3}$$

Here, ϕ_i are the KS orbitals filled with electrons. Hence, one can get exchange energy by modeling the exchange hole through density matrix. Here, we use a model for exchange hole, originally developed for 3D systems by Negele-Vautherin (NV).[73] In the relative and center-of-mass coordinates $\mathbf{u}$ and $\mathbf{R}$, the density matrix can be expressed as,

$$\Gamma_1\left(\mathbf{R} + \frac{\mathbf{u}}{2}, \mathbf{R} - \frac{\mathbf{u}}{2}\right) = \sum_i \phi_i^*\left(\mathbf{R} + \frac{\mathbf{u}}{2}\right) \phi_i\left(\mathbf{R} - \frac{\mathbf{u}}{2}\right) , \tag{2.4}$$

where $\mathbf{R} = \frac{\mathbf{r} + \mathbf{r}'}{2}$ and $\mathbf{u} = \mathbf{r} - \mathbf{r}'$. By employing the Taylor series expansion, Eq.(2.4) is written as,

$$\Gamma_1^{2D} = e^{\mathbf{u} \cdot \frac{(\vec{\nabla}_1 - \vec{\nabla}_2)}{2}} \sum_i \phi_i^*(\mathbf{R_1}) \phi_i(\mathbf{R_2})|_{u=0} = e^{u \frac{(\vec{\nabla}_1 - \vec{\nabla}_2)}{2} cos\phi} \sum_i \phi_i^*(\mathbf{R_1}) \phi_i(\mathbf{R_2})|_{u=0} , \quad (2.5)$$

where $\vec{\nabla}_1$ acts on $\mathbf{R_1}$ and $\vec{\nabla}_2$ acts on $\mathbf{R_2}$. Now, to derive the 2D Negele-Vautherin exchange hole,[73] the plane wave present in Eq.(2.5) is expanded in terms of the Bessel and hypergeometric functions using the generalized Gegenbauer additional theorem[74] as follows,

$$e^{izy} = \frac{2}{z} \sum_{n=0}^{\infty} (2n+1)(-1)^n J_{2n+1}(z) C_{2n}^1(y) \quad (2.6)$$

with $z = ku$, $y = -\frac{i(\vec{\nabla}_1 - \vec{\nabla}_2)cos\phi}{2k}$, and k being the Fermi momentum. J_{2n+1} are the Bessel functions and the polynomial C_{2n}^m is expressed as,

$$C_{2v}^m(x) = (-1)^v \begin{pmatrix} v + m - 1 \\ v \end{pmatrix} {}_2F_1\left(-v, v+m; \frac{1}{2}; x^2\right) \quad (2.7)$$

with ${}_2F_1$ being the generalized Hypergeometric function that follows a general form,

$$_2F_1(a, b; c; z) = \sum_{n=0}^{\infty} \frac{(a)_n (b)_n}{(c)_n} \frac{z^n}{n!}$$

Now, using Eq.(2.6) and Eq.(2.7), the density matrix Eq.(2.5) up to second order in u^2 is derived as,

$$\Gamma_1^{2D}\left(\mathbf{R} + \frac{\mathbf{u}}{2}, \mathbf{R} - \frac{\mathbf{u}}{2}\right) = \frac{2J_1(ku)}{ku} \rho(R) + \frac{6J_3(ku)}{k^3 u} \left[4\cos^2\phi\left\{\frac{\nabla^2\rho}{4} - 2\tau\right\} + k^2\rho\right] , \quad (2.8)$$

where $\tau = \sum_i^{occ} |\vec{\nabla}\phi_i|^2$ is the KS kinetic energy density. Now, we calculate the cylindrically averaged density matrix to get rid of angular dependency of the density matrix and

hence the exchange hole. With the realization of

$$
\begin{aligned}
\left\langle |\Gamma_1^{2D}\left(\mathbf{R}+\frac{\mathbf{u}}{2},\mathbf{R}-\frac{\mathbf{u}}{2}\right)|^2\right\rangle_{cyl} &= \left\langle |\Gamma_1^{2D}\left(\mathbf{R}+\frac{\mathbf{u}}{2},\mathbf{R}-\frac{\mathbf{u}}{2}\right)|\right\rangle_{cyl}^2 + O(u^4) \\
&= \rho(\mathbf{R}) + \frac{u^2}{2}\rho(\mathbf{R})[\frac{1}{4}\nabla^2\rho(\mathbf{R}) - 2\tau] + O(u^4), \quad (2.9)
\end{aligned}
$$

the cylindrical average density matrix is written as,

$$
\left\langle |\Gamma_{1t}^{2D}\left(\mathbf{R}+\frac{\mathbf{u}}{2},\mathbf{R}-\frac{\mathbf{u}}{2}\right)|\right\rangle_{cyl} = \frac{2J_1(ku)}{ku}\rho(R) + \frac{6J_3(ku)}{k^3u}\left[\frac{\nabla^2\rho}{2} - 4\tau + k^2\rho\right]. \quad (2.10)
$$

Now, if one expands the Bessel functions, hence Eq.(2.10), it perfectly recovers the exact form for small u from Eq.(2.9). In 3D, such type of expansion has been used by Negele-Vautherin,[73] Scuseria and co-workers,[26,39,40] and Tsuneda et. al.[71] Recently proposed Tao-Mo 3D-mGGA functional[42] that is based on the density matrix expansion and the series resummation technique is transformed to its 2D counterpart[74] by Jana et al. Here, the main motivation is to derive a very simple form of the exchange energy by terminating our exchange hole up to u^2, and without applying the series resummation technique. So, using the simple form of cylindrical averaged density matrix of Eq.(2.10), the cylindrical averaged exchange hole can be written as,

$$
\langle\rho_x(R,u)\rangle_{cyl} = -\frac{2J_1^2(ku)\rho(R)}{k^2u^2} - \frac{12J_1(ku)J_3(ku)}{k^4u^2}\left[\frac{\nabla^2\rho}{2} - 4\tau + k^2\rho\right]. \quad (2.11)
$$

For homogeneous density, the Laplacian of density present within the square bracket becomes zero, and other two terms cancels with each other. So, in the homogeneous limit, only the first term in Eq.(2.11) survives which is the exact exchange hole for uniform electron gas. The recovery of the correct exchange hole in the HEG limit is a positive sign to proceed, and we will be using such exchange hole to construct exchange energy functionals in the following section.

2.2.1   Parameter-free exchange energy functional

Now, we use the above-developed cylindrical averaged density matrix expansion and hence the exchange hole to construct a parameter-free exchange energy functional. In the center-of-mass coordinate system, the exchange energy expression Eq.(2.1) becomes

$$E_x = \frac{1}{2} \int d^2R \int d^2u \frac{\rho(R)\langle \rho_x(R,u)\rangle_{cyl}}{u}. \tag{2.12}$$

The use of cylindrically averaged exchange hole of Eq.(2.11), the exchange energy Eq.(2.12) is written as,

$$E_x = -\frac{1}{2} \int d^2R \left[\frac{16\rho^2}{3k} + \frac{32\rho}{15k^3} \left(\frac{\nabla^2\rho}{2} - 4\tau + k^2\rho \right) \right]. \tag{2.13}$$

The above form of exchange energy functional contains the Laplacian of density and the presence of $\nabla^2\rho$ may lead to numerical instability. This is because it diverges near nucleus for 3D systems, and also some of previous studies in 2D[74,75] suggest to replace the Laplacian of density with appropriateform. So, we replace the Laplacian of density by utilizing the identity suggested by Voorhis and Scuseria[40] in 3D and adopted by Pittalis et. al.[76] for 2D. This leads to,

$$E_x = -\frac{1}{2} \int d^2R \left[\frac{16\rho^2}{3k} + \frac{32\rho^3}{15k^3} \left\{ \frac{x^2}{4} - \left(\frac{4\tau - k^2\rho}{\rho^2} \right) \right\} \right], \tag{2.14}$$

where $x = \frac{|\nabla\rho|}{\rho^{3/2}}$ is the 2D reduced density gradient. Now, using the spin density scaling relation,

$$E_x[\rho_\uparrow, \rho_\downarrow] = \frac{1}{2} E_x[2\rho_\uparrow] + \frac{1}{2} E_x[2\rho_\downarrow], \tag{2.15}$$

the spin polarized exchange energy becomes,

$$E_x[\rho_\sigma, k_\sigma, \tau_\sigma] = -\frac{1}{2} \sum_\sigma \int d^2R \left[\frac{32\rho_\sigma^2}{3k_\sigma} + \frac{128\rho_\sigma^3}{15k_\sigma^3} \left(\frac{x_\sigma^2}{8} - z_\sigma \right) \right]. \tag{2.16}$$

Here, a dimensionless quantity z is defined as $z_\sigma = (4\tau_\sigma - 2k_\sigma^2\rho_\sigma)/4\rho_\sigma^2$. The 1st choice for k_σ is quite obvious i.e. the Fermi momentum $k_\sigma = k_{F\sigma} = \sqrt{4\pi\rho_\sigma}$. In general the mo-

mentum k_σ can be thought as a parameter which obeys one restriction, i.e., the dimension of k_σ should be length inverse (wavevector).[40] Now, we make a kinetic energy density $\tau_\sigma(R)$ dependent k_σ, similar to a previous work by Tsuneda et.al.[71] in 3D through the following relation,

$$\tau_\sigma(\mathbf{R}) = 2\langle \frac{k^2}{2} \rangle \rho_\sigma(R) \quad = \quad \rho_\sigma(\mathbf{R}) \frac{\int k_\sigma^2 f_\sigma(R,k_\sigma) d^2 k_\sigma}{\int f_\sigma(R,k_\sigma) d^2 k_\sigma} = \frac{k_\sigma^2}{2} \rho_\sigma . \tag{2.17}$$

The distribution function $f_\sigma(R,k)$ is approximated by the step function in the momentum space.[71] As the k_σ of Eq.(2.17) is identical to the Fermi momentum in our exchange energy expression, we will be taking the help of this kinetic energy dependent k_σ. Upon using Eq.(2.17), k_σ can be expressed as,

$$k_\sigma = k_\sigma[\tau_\sigma] = \sqrt{\frac{2\tau_\sigma}{\rho_\sigma}} . \tag{2.18}$$

In above Eq.(2.18), If we use the 2D Thomas-Fermi (TF) kinetic-energy density, $\tau_\sigma^{TF} = 2\pi\rho_\sigma^2$, then momentum vector k_σ will be identical to the 2D Fermi momentum $k_{F\sigma} = \sqrt{4\pi\rho_\sigma}$ for the homogeneous system. Using k_σ from Eq.(2.18) in Eq.(2.16), we get a vanishing z_σ, and a simple parameter-free, meta-GGA exchange functional (E^{PF}) in 2D is obtained,

$$E_x^{PF}[\rho_\sigma, \nabla\rho_\sigma, k_\sigma[\tau_\sigma]] = -\frac{1}{2} \sum_\sigma \int d^2 R \, \frac{32\rho_\sigma^2}{3 k_\sigma} \left[1 + \frac{x_\sigma^2 \rho_\sigma}{10 k_\sigma^2} \right] , \tag{2.19}$$

Now, let's replace k_σ with help of Eq.(2.18). This replacement leads a kinetic energy dependent mGGA exchange functional of form,

$$E_x^{PF}[\rho_\sigma, \nabla\rho_\sigma, \tau_\sigma] = -\frac{1}{2} \sum_\sigma \int d^2 R \, \frac{32\rho_\sigma^{5/2}}{3\sqrt{2\tau_\sigma}} \left[1 + \frac{x_\sigma^2 \rho_\sigma}{20\tau_\sigma} \right] . \tag{2.20}$$

The choice of τ_σ present in Eq.(2.20) can be used as a progressive part, i.e., the form of τ_σ can be varied with our convenience. We start from the simple form of τ. Considering the uniform electron gas, the Thomas-Fermi kinetic energy density $\tau_\sigma = \tau_\sigma^{TF}$ is

Table 2.1: Shown are the exchange energies of parabolic quantum dots in atomic units (a.u.) by using E_x^{PF-KS}, with $\tau_\sigma = \tau_\sigma^{KS}$ and E_x^{MPF}. The first column shows the number of confined electrons and the second column the confinement strengths. The exchange energies as obtained from E_x^{PF-KS} and E_x^{MPF} functionals are presented in the last two columns. Exchange energies of the exact exchange 2D-EXX, 2D-LSDA, 2D-B88, and 2D-B86 as obtained from OCTOPUS code are also shown for the comparison. The last row represents the MAPE, Δ.

N	ω	$-E_x^{2D-EXX}$	$-E_x^{2D-LSDA}$	$-E_x^{2D-B86}$	$-E_x^{2D-B88}$	$-E_x^{PF-KS}$	$-E_x^{MPF}$
2	1/6	0.380	0.337	0.368	0.364	0.373	0.413
2	0.25	0.485	0.431	0.470	0.464	0.479	0.527
2	0.50	0.729	0.649	0.707	0.699	0.726	0.789
2	1.00	1.083	0.967	1.051	1.039	1.085	1.167
2	1.50	1.358	1.214	1.319	1.344	1.365	1.457
2	2.50	1.797	1.610	1.748	1.728	1.812	1.908
2	3.50	2.157	1.934	2.097	2.074	2.175	2.258
Δ			16.55	2.94	3.59	**0.83**	7.35

our first choice. But the uniform kinetic energy density is far from the exact interacting system. So, upon using τ_σ^{TF} in in Eq.(2.20), we get unsatisfactory results. Hence, we are omitting the discussion of this form of exchange energy in the calculation section. The second form of the τ, is the Kohn-Sham kinetic energy density τ_σ^{KS}, and we are denoting the corresponding exchange functional obtained from Eq.(2.20) as E_x^{PF-KS}. The results for E_x^{PF-KS} are discussed in Table 2.1 and Table 2.2 that present exchange energies of parabolic quantum dots having different confinement strength and confined electrons. However, some mediocre results of Eq.(2.20) prompted us to remodel the functional form Eq.(2.19) more appropriately. The potential reasons for such results are also explained in the next part in more detail.

As mentioned, the modifications in the form of the functional are done by imposing physical constraints. For any nonuniform systems, we seek an energy form, the first term of which must recover the LDA, and the subsequent terms can be regarded as the advance order corrections to LDA. For this purpose, we have replaced k_σ present in the first part of Eq.(2.19) with $k_{F\sigma}$, and used the k_σ from Eq.(2.18) in the second part. After such

changes, the modified parameter free (MPF) exchange functional (E_x^{MPF}) becomes

$$E_x^{MPF}[\rho_\sigma, \nabla\rho_\sigma, \tau_\sigma] = -\frac{1}{2}\sum_\sigma \int d^2R \, \frac{8k_{F\sigma}\rho_\sigma}{3\pi}\left[1 + \frac{x_\sigma^2 \rho_\sigma}{10\left(\sqrt{\frac{2\tau_\sigma}{\rho_\sigma}}\right)^2}\right] \qquad (2.21)$$

The form of E_x^{MPF} is simple, and the first term represents the LDA exchange energy. The stability of E_x^{MPF} is expected to be more as it recovers the LDA exchange completely, and the non-uniform effects are taken care by the second term.

2.2.2   Numerical Demonstration - I

We demonstrate the performance of newly developed 2D functionals E_x^{PF-KS}, and (E_x^{MPF}) by applying it to multi-electron quantum dots (QD). The parabolic potential representing the QD is "$V_0 = \omega^2 r^2/2$", ω is the confinement strength. The exchange energies corresponding to 2D-KLI,[77] 2D-LSDA,[78] 2D-B88[79] and 2D-B86[76] are also calculated within the spin DFT implemented in the OCTOPUS code.[80] The output densities, and the kinetic energy densities of self-consistent KLI-OEP are used as the input for all the new functionals. The performances of the newly proposed exchange energy functionals, Eq.(2.20) with $\tau_\sigma = \tau_\sigma^{KS}$ and Eq.(2.21) are given in Table 2.1 for two electrons and in Table 2.2 for $N = 6$ to $N = 56$. The value of the confinement strength is varied from $1/6$ to 3.5. We intentionally present the results in two tables to show the advantages of E_x^{MPF} for $N > 2$.

From Table 2.1, we observe that E_x^{PF-KS} which is constructed by the replacement of τ_σ with τ_σ^{KS} in Eq.(2.20) give better exchange energies for two electrons QDs and leads to the best mean absolute percentage error (MAPE). So, the functional E_x^{PF-KS} presented in Eq.(2.20) can be used to study the properties of the quantum dots having only two confined electrons. However, the first term in Eq.(2.20) with the KS-KE density looks unstable, and it is observed that with the increase of electrons and ω value, the error increases. Such inefficient performance is caused due to the delocalization of τ_σ^{KS} relative to the density of electrons ρ_σ. In 3D, a similar outcome can be seen in the work of Tsuneda et. al..[71] So, for betterment, we have modified Eq.(2.19) into Eq.(2.21).

Next, we examine the performance of E_x^{MPF} presented in Eq.(2.21). The results for

Table 2.2: All the columns are identical to Table 2.1 but with $N = 6$ to 56.

N	ω	$-E_x^{2D-EXX}$	$-E_x^{2D-LSDA}$	$-E_x^{2D-B86}$	$-E_x^{2D-B88}$	$-E_x^{PF-KS}$	$-E_x^{MPF}$
6	$1/1.89^2$	1.735	1.642	1.719	1.749	1.775	1.743
6	0.25	1.618	1.531	1.603	1.594	1.655	1.626
6	0.42168	2.229	2.110	2.206	2.241	2.283	2.238
6	0.50	2.470	2.339	2.444	2.431	2.532	2.481
6	1.00	3.732	3.537	3.690	3.742	3.830	3.745
6	1.50	4.726	4.482	4.672	4.648	4.851	4.740
6	2.50	6.331	6.008	6.258	6.226	6.491	6.337
6	3.50	7.651	7.264	7.562	7.525	7.829	7.642
12	0.50	5.431	5.257	5.406	5.387	5.559	5.442
12	1.00	8.275	8.013	8.230	8.311	8.474	8.282
12	1.50	10.535	10.206	10.476	10.444	10.789	10.534
12	2.50	14.204	13.765	14.122	14.080	14.535	14.169
12	3.50	17.237	16.709	17.136	17.086	17.620	17.153
20	0.50	9.765	9.553	9.746	9.722	9.968	9.783
20	1.00	14.957	14.638	14.919	15.029	15.266	14.977
20	1.50	19.108	18.704	19.053	19.188	19.496	19.123
20	2.50	25.875	25.334	25.796	25.973	26.376	25.867
20	3.50	31.491	30.837	31.392	31.603	32.063	31.445
30	1.00	23.979	23.610	23.953	24.091	24.410	24.005
30	1.50	30.707	30.237	30.665	30.836	31.249	30.722
30	2.50	41.718	41.085	41.651	41.878	42.420	41.686
30	3.50	50.882	50.115	50.794	51.068	51.694	50.778
42	1.00	35.513	35.099	35.503	35.671	36.071	35.561
42	1.50	45.560	45.032	45.538	45.747	46.259	45.606
42	2.50	62.051	61.339	62.007	62.286	62.946	62.062
42	3.50	75.814	74.946	75.748	76.085	76.837	75.771
56	1.00	49.710	49.256	49.722	49.919	50.407	49.771
56	1.50	63.869	63.289	63.871	64.117	64.739	63.921
56	2.50	87.164	86.378	87.148	87.479	88.281	87.160
56	3.50	106.639	105.684	106.609	107.010	107.918	106.542
Δ			2.75	0.45	0.58	**1.97**	**0.17**
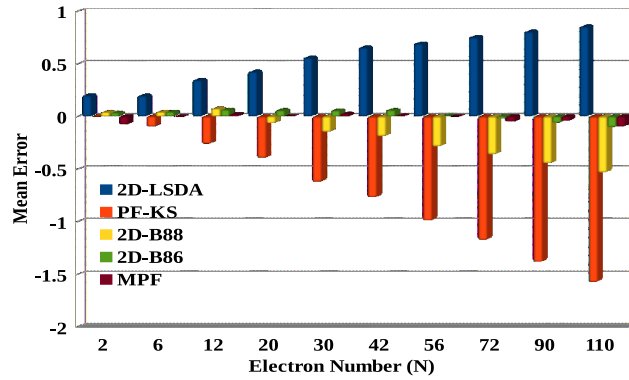
Figure 2.1: The mean errors of different exchange energy functionals listed in Table 2.2 for few electron parabolic quantum dots. For systems having $N = 72$, 90, and 110, ω is varied from 1 to 3.5.
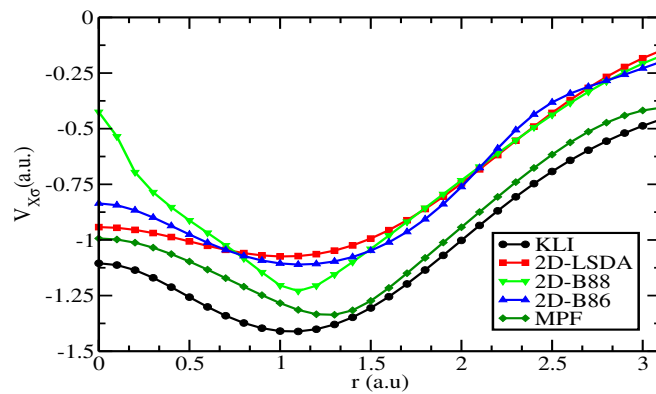
Figure 2.2: The exchange potentials for a parabolic quantum dot with N=6 and $\omega = 1$.

Table 2.3: The exchange energies (in a.u.) of Gaussian quantum dots using E_x^{MPF} i.e. Eq.(2.21). For comparison, the results obtained with other relevant functionals are also provided and the last row represents the MAPE.

N	ω^2	$-E_x^{2D-EXX}$	$-E_x^{2D-LSDA}$	$-E_x^{2D-B86}$	$-E_x^{2D-MPF}$
6	0.10	6.525	6.193	6.450	6.521
6	1/6	7.454	7.076	7.367	7.444
6	0.25	8.255	7.840	8.160	8.232
6	0.50	9.744	9.260	9.635	9.688
12	0.10	14.324	13.887	14.241	14.255
12	1/6	16.304	15.812	16.211	16.187
12	0.25	17.986	17.437	17.873	17.824
12	0.50	20.908	20.295	20.795	20.634
20	0.1	25.386	24.871	25.311	25.354
20	1/6	28.692	28.122	28.611	28.606
20	0.25	31.349	30.736	31.263	31.197
Δ			3.47	0.70	**0.48**

QDs with $N = 2$ are tabulated in Table 2.1, and the MAPE is better than the 2D-LSDA and inferior to 2D-B88 and 2D-B86. But for QDs having more than two confined electrons, E_x^{MPF} gives the best result(Table 2.2), and it will be very useful to study practical systems in 2D. We emphasize on the calculated MAPE of E_x^{MPF}) given in Table 2.2, i.e., 0.17 which is the best MAPE calculated so far. We plot the mean error (ME) of the functionals presented in Table 2.2 in Figure 2.1 considering parabolic QDs with a set of electron numbers up to 56. The color bars represent the exchange energy functionals. It can be seen that, the deviations of E_x^{MPF} are very small the 2D-KLI (origin). In Figure 2.2, we have plotted the exchange potentials of discussed functionals for a parabolic QD with $N = 6$ and $\omega = 1$. The potential of MPF matches comparatively more appropriately with the KLI potential, but all the semilocal potentials fail to produce exact behavior in the asymptotic region.

Next, we analyze the performance of the simple parameter free exchange energy functional applying to the Gaussian quantum dot system with external potential "$V(r) = -V_0 exp(-\omega^2 r^2)$", where $-V_0$ be the depth of the potential. Here, the shape of the potential depends on ω and V_0. For the present study, we have fixed V_0 at 40 $a.u.$, and varied

the electron number (N) and confinement strength ω. The exchange energies for these systems are tabulated in Table 2.3. In this case, the reduction in error for E_x^{MPF} is quite encouraging. A clear improvement over 2D-LSDA is observed from the above table. The small error of E_x^{MPF} functional in both types of quantum dots increases the merit of such construction.

The E_x^{MPF} functional has a very simple mathematical form and the accuracy is very good for systems having electrons more than two. The underlying exchange hole always has a scope for new developments and we use the general coordinate transformation of it to model new exchange-correlation energy functionals in the next section.

2.3   Coordinate transformation of the exchange hole and energy functionals

In the previous section, we formulated the density matrix expansion for 2D, and used the same to make exchange hole and hence the exchange energy functional. Here, we take advantages of coordinate transformation, which will make the density matrix and the exchange hole more localized and the shape of the exchange hole can be controlled. Now, we use the general coordinate transformation $(\mathbf{r}, \mathbf{r}') \rightarrow (\mathbf{r}_\lambda, \mathbf{u})$ with $\mathbf{r}_\lambda = \lambda \mathbf{r} + (1 - \lambda)\mathbf{r}'$ and $\mathbf{u} = \mathbf{r}' - \mathbf{r}$. The Jacobian of such transformation is 1 and a real number λ lies between $1/2$ and 1. The advantage of such transformation can be understood if we analyze the behavior of exchange hole at two extreme values of λ. At $\lambda = 1/2$, the exchange hole is transformed to the center of the mass coordinate system, leading to a maximally localized hole. On the other hand, $\lambda = 1$ leads to a conventional hole. Now, using this transformation in the exchange energy expression Eq.(2.1), the exchange energy written as

$$E_x = \frac{1}{2} \int d^2 r_\lambda \int d^2 u \, \frac{\rho(\mathbf{r}_\lambda)\rho_x(\mathbf{r}_\lambda, \mathbf{u})}{\mathbf{u}} \, , \qquad (2.22)$$

and Eq.(2.2) can be rewritten as

$$\rho_x(\mathbf{r}_\lambda, \mathbf{u}) = -\frac{\langle |\gamma_1^t(\mathbf{r}_\lambda - (1-\lambda)\mathbf{u}, \mathbf{r}_\lambda + \lambda\mathbf{u})|^2 \rangle}{2\rho(\mathbf{r}_\lambda)} , \qquad (2.23)$$

where $\gamma_1^t(\mathbf{r}_\lambda - (1-\lambda)\mathbf{u}, \mathbf{r}_\lambda + \lambda\mathbf{u})$ is the transformed single-particle density matrix. Now, expanding the density matrix about $u = 0$ and using the Bessel and Hypergeometric functions as discussed before, the density matrix Eq.(2.10) transformed to

$$\Gamma_{1t} = 2\rho\frac{J_1(ku)}{ku} + \frac{6J_3(ku)}{k^3 u}\left[4\cos^2\phi\{(\lambda^2 - \lambda + \frac{1}{2})\nabla^2\rho - 2\tau\} + k^2\rho\right]. \qquad (2.24)$$

Such expansion is comprehensible as the zeroth order expansion recovers the 2D-LDA and the λ dependency is only restricted to the second term. The second term takes care of the non-uniformity involved in the actual system. Now this transformed density matrix can be used to get a general coordinate transformed cylindrical averaged exchange hole by using Eq.(2.23), and is expressed as

$$\rho_x(r, u) = -\frac{2J_1^2(ku)\rho}{k^2 u^2} - \frac{12J_1(ku)J_3(ku)}{k^4 u^2}\mathscr{A} - \frac{18J_3^2(ku)}{k^6 u^2 \rho}\mathscr{A}^2, \qquad (2.25)$$

where, $\mathscr{A} = 2(\lambda^2 - \lambda + \frac{1}{2})\nabla^2\rho - 4\tau + k^2\rho$. The first term in above Eq.(2.25) is the exchange hole for the homogeneous system, i.e., the LDA exchange hole is perfectly recovered with our method. And the transformation of exchange hole is reflected in other subsequent terms without affecting the uniform limit. The translational-invariance of uniform system can be well observed. To get exchange functionals with reliable accuracy, we keep the expansion up to 4th order in u. Next, we use this averaged exchange hole to model exchange, and correction energy functionals.

2.3.1   Parameterized Exchange energy functionals

Now, to construct the desired semilocal meta-GGA type exchange functionals, we use the exchange hole presented in Eq.(2.25) in the exchange energy form of Eq.(2.22), and replace the Laplacian of density with the help of integration by parts (similar to Eq.(2.14)).

The final exchange energy form is written as,

$$E_x = -\int d^2r \left[\frac{8\rho^2}{3k} + \frac{16\rho^3}{15k^3}\mathscr{B} + \frac{32\rho^4}{35k^5}\mathscr{B}^2 \right], \tag{2.26}$$

where

$$\mathscr{B} = \left(\lambda^2 - \lambda + \frac{1}{2} \right)x^2 - \left(\frac{4\tau - k^2\rho}{\rho^2} \right) \tag{2.27}$$

and $x = \frac{|\nabla\rho|}{\rho^{3/2}}$ is the 2D reduced density gradient. The exchange energy functional presented in above Eq.(2.27) depends on the electron density ρ, the kinetic energy density τ, parameter λ, and the momentum k. The choice of momentum k is in our hand, and that can be used to enforce the functional to include non-uniformity of the real system. Replacing k with the Fermi momentum $k_F = \sqrt{2\pi\rho}$, and using Thomas-Fermi kinetic energy density $\tau^{unif} = \pi\rho^2/2$, it can be seen that the homogeneous constraint is well satisfied. To go beyond the local-density model other physically motivated forms of momentum k need to be adopted. Before going to model different forms of k, we present the spin-scaled form of the exchange energy using the relation presented in Eq.(2.15) as,

$$E_x = -\frac{1}{2} \sum_{\sigma=\uparrow,\downarrow} \int d^2r \left[\frac{32\rho_\sigma^2}{3k_\sigma} + \frac{128\rho_\sigma^3}{15k_\sigma^3}\mathscr{G}_\sigma(x_\sigma,z_\sigma) + \frac{512\rho_\sigma^4}{35k_\sigma^5}\mathscr{G}_\sigma^2(x_\sigma,z_\sigma) \right], \tag{2.28}$$

where

$$\mathscr{G}_\sigma(x_\sigma,z_\sigma) = (\lambda^2 - \lambda + \frac{1}{2})\frac{x_\sigma^2}{2} - z_\sigma, \tag{2.29}$$

and "$z_\sigma = \frac{\tau}{\rho_\sigma^2} - 2\pi$" is a dimensionless quantity. As discussed, the functional form of the momentum is not unique, but any accepted choice must obey one constraint, i.e., k should follow inverse of length dimension. Using the obvious choice $k = k_F$, the exchange functional becomes,

$$E_x = -\frac{1}{2} \sum_{\sigma=\uparrow,\downarrow} \int d^2r \frac{32\rho_\sigma^2}{3k_F} \left[1 + \frac{4\rho_\sigma\mathscr{G}_\sigma(x_\sigma,z_\sigma)}{5k_F^2} + \frac{48\rho_\sigma^2\mathscr{G}_\sigma^2(x_\sigma,z_\sigma)}{35k_F^4} \right]. \tag{2.30}$$

However, our priority is to add the inhomogeneity of the interacting system by choosing different forms of momentum k. Depending on the physically admissible choices of k

other than k_F, we propose different exchange energy functionals. To incorporate the non-uniformity of the real system in the energy form through momentum, suitable functionals having density dependency need to be added intuitively, and the LDA exchange functional must be recovered upon imposing the homogeneity limit. In principle, it is possible because the form of the exchange energy functional, i.e., Eq.(2.30), depends on dimensionless quantities x_σ and z_σ. For uniform systems, x_σ becomes zero as it depends on $\nabla \rho$, and z_σ goes to zero at $\tau = \tau^{unif}$ (HEG). Using x_σ, and z_σ as the ingredients, functionals are developed in the next subsections.

2.3.1.1 Density gradient dependent momentum

Here, we modify the Fermi momentum by utilizing the dimensionless reduced density gradient. The addition of x_σ^2 to k_F obeys the required constraints, i.e., the new momentum $\bar{k}_{F,g}$ secures the dimension of length inverse and becomes k_F in the homogeneous density limit. We propose the first modification to the Fermi momentum as,

$$\bar{k}_{F,g} = k_F(1 + \alpha x_\sigma^2), \tag{2.31}$$

where α is an adjustable parameter that takes care of the gradient effect. Using $\bar{k}_{F,g}$ from Eq.(2.31), in Eq.(2.30) the new semilocal exchange energy functional E_x^{GDM} (exchange energy with gradient dependent momentum) becomes,

$$E_x^{GDM}[x_\sigma, z_\sigma] = -\frac{1}{2} \sum_{\sigma=\uparrow,\downarrow} \int d^2r \left[\frac{32\rho_\sigma^2}{3\bar{k}_{F,g}} + A\frac{128\rho_\sigma \mathscr{G}_\sigma(x_\sigma, z_\sigma)}{15\bar{k}_{F,g}^3} + B\frac{512\rho_\sigma^2 \mathscr{G}_\sigma^2(x_\sigma, z_\sigma)}{35\bar{k}_{F,g}^5} \right]. \tag{2.32}$$

In the present study, we have terminated the density matrix at 2nd order. Hence, the underlying exchange hole is not completely correct. To take care the left over effect, two adjustable parameters A and B are introduced, which will be fixed later. Also, because of $\bar{k}_{F,g}$ present in the denominator of the first term, the first term is different from the LSDA exchange energy. To incorporate these effects, parameterization of higher order terms are essential.

2.3.1.2   Kinetic energy dependent momentum

Next, we attempt to modify the momentum through the kinetic energy density. The kinetic energy density is encountered through the term z_σ present in the exchange energy functional Eq.(2.30). The inclusion of z_σ in k_F, will make the momentum to depend on the kinetic energy density. In this way, the inhomogeneous effect of the interacting system can be included in the functional form. It is conspicuous that addition of a fraction of z_σ to k_F obeys the dimension and uniform density limit restrictions. Thus, a new form of the transformed momentum is proposed to be,

$$\overline{k}_{F,t} = k_F(1 + \alpha z_\sigma). \tag{2.33}$$

Similar to Eq.(2.31), α is the adjustable parameter introduced to add the inhomogeneity through a small fraction of z_σ. Now, putting the transformed momentum Eq.(2.33) in the exchange form of Eq.(2.30), the exchange energy functional E_x^{TDM} (τ dependent momentum), similar to Eq.(2.32) written as,

$$E_x^{TDM}[x_\sigma, z_\sigma] = -\frac{1}{2} \sum_{\sigma=\uparrow,\downarrow} \int d^2r \Big[\frac{32\rho_\sigma^2}{3\overline{k}_{F,t}} + A\frac{128\rho_\sigma \mathscr{G}_\sigma(x_\sigma, z_\sigma)}{15\overline{k}_{F,t}^3} + B\frac{512\rho_\sigma^2 \mathscr{G}_\sigma^2(x_\sigma, z_\sigma)}{35\overline{k}_{F,t}^5} \Big].$$
$$\tag{2.34}$$

Similar Eq.(2.32), A and B are the adjustable parameters. The Eq.(2.34) only differs from Eq.(2.32) by a different choice of momentum, i.e., $\overline{k}_{F,g}$ is replaced by $\overline{k}_{F,t}$.

2.3.1.3   Reduced density gradient and kinetic energy density dependent momentum

So far the reduced density gradient x_σ and z_σ are used individually in the momentum to include the inhomogeneity effects in the semilocal functionals. The use of both x_σ and z_σ together is also an option as the addition of both terms in appropriate order will respect the required constraints. Following a simple form to add both the kinetic energy density and reduced density gradient in the momentum as,

$$\overline{k}_{F,g,t} = k_F\{1 + \alpha(x_\sigma^2 + z_\sigma)\}, \tag{2.35}$$

Table 2.4: Tabulated are the asigned values of all the constants present in the exchange energy functionals E_x^{GDM}, E_x^{TDM}, and E_x^{GTDM}

Functional	α	A	B
E_x^{GDM}	0.001	0.2	0.3303
E_x^{TDM}	0.001	0.2	0.0824
E_x^{GTDM}	0.001	0.2	0.3646

where α is an adjustable parameter defined in the same manner as Eq.(2.31) and Eq.(2.33). The exchange energy functional E_x^{GTDM}(gradient and τ dependent momentum) with $\bar{k}_{F,g,t}$ is,

$$E_x^{GTDM}[x_\sigma, z_\sigma] = -\frac{1}{2} \sum_{\sigma=\uparrow,\downarrow} \int d^2r \left[\frac{32\rho_\sigma^2}{3\bar{k}_{F,g,t}} + A\frac{128\rho_\sigma \mathscr{G}_\sigma(x_\sigma, z_\sigma)}{15\bar{k}_{F,g,t}^3} + B\frac{512\rho_\sigma^2 \mathscr{G}_\sigma^2(x_\sigma, z_\sigma)}{35\bar{k}_{F,g,t}^5} \right],$$

(2.36)

where A and B are again tunable constants. The effects of higher-order terms in the density matrix expansion can be included through these parameters.

2.3.2   The correlation energy functional

After developing the exchange energy functionals, we focus on the correlation part of the total energy. It is necessary to construct an appropriate semilocal correlation functional which will be more relevant for our exchange energies, constructed above. The 2D-LDA correlation energy functional[65] is a commonly used functional in calculating 2D systems. The analytic form of 2D-LDA correlation energy functional was constructed by interpolating two limiting behaviors, the low-density limit from the Diffusion Monte Carlo (DMC) data and high-density limit from a 2D LDA type exchange-correlation energy functional,[81] and given as,

$$\varepsilon_c^{LDA}(r_s, \zeta) = (e^{-\beta r_s} - 1)\varepsilon_x^{(6)}(r_s, \zeta) + \alpha_0(r_s) + \alpha_1(r_s)\zeta^2 + \alpha_2(r_s)\zeta^4,$$

(2.37)

where $r_s = 1/\sqrt{\pi\rho}$, ζ is the usual spin-polarization and $\varepsilon_x^{(6)}(r_s, \zeta) = \varepsilon_x(r_s, \zeta) - (1 + \frac{3}{8}\zeta^2 + \frac{3}{128}\zeta^4)\varepsilon_x(r_s, 0)$ is the Taylor expansion of ε_x beyond fourth order in ζ. Here, the

2D-LSDA exchange energy term, $\varepsilon_x = -2\sqrt{2}[(1+\zeta)^{3/2} + (1-\zeta)^{3/2}]/3\pi r_s$. The functional form of $\alpha_i(r_s)$ is taken as a 2D generalization form from electron-gas correlation of Perdew-Wang[49] and is given by,

$$\alpha_i(r_s) = A_i + \left(B_i + C_i r_s^2 + D_i r_s^3\right) \times ln\left(1 + \frac{1}{E_i r_s + F_i r_s^{3/2} + G_i r_s^2 + H_i r_s^3}\right). \qquad (2.38)$$

The values of these parameters present in the above Eq.(2.38) is same as present in the Table II of reference.[65] This correlation functional is local as it depends only on spin-polarization ζ and the electron density ρ via r_s. However, such LDA functional tend to overestimate the correlation energy of the parabolic QDs up to a large extent, that can be observed from Table 2.6. So, modification to the functional form is essential for applying it to non-uniform systems. We suggest that the non-local effects of the interacting system can be induced in the LDA correlation energy via a parametric form of the exchange functional derived above. In fact, use of the exchange enhancement factor in the correlation energy is encountered in recent 3D correlation functionals.[26,82] Similar to 3D, here, we have used a modified form of E_x^{GTDM} with convenient parameters. The modified form of momentum from Eq.(2.35) with a different constant can be written as,

$$\bar{k}_{F,g,t} = k_F\{1 + \delta(x_\sigma^2 + z_\sigma)\} = k_F \Gamma_\sigma(x_\sigma, z_\sigma). \qquad (2.39)$$

Now, this form of momentum can be used in place of k_σ present in the Eq.(2.28), and with this replacement Eq.(2.28) modified to,

$$E_x = -\frac{1}{2}\sum_{\sigma=\uparrow,\downarrow}\int d^2r\, \frac{32\rho_\sigma^2}{3k_F}\left[\frac{L}{\Gamma_\sigma} + \frac{M\,4\rho_\sigma \mathscr{G}_\sigma(x_\sigma,z_\sigma)}{5k_F^2\Gamma_\sigma^3} + \frac{N\,48\rho_\sigma^2 \mathscr{G}_\sigma^2(x_\sigma,z_\sigma)}{35k_F^4\Gamma_\sigma^5}\right], \qquad (2.40)$$

where L, M, and N are parameters through which the effect of neglected higher order terms can be included. The above Eq.(2.40) differs from E_x^{GTDM} by a small change in the enhancement factor. This modification is essential to have a suitable multiplicative factor for the correlation functional. It is to be note that, Eq.(2.40) is not for the exchange energy calculations, but to include the non-local effects in the correlation functional using
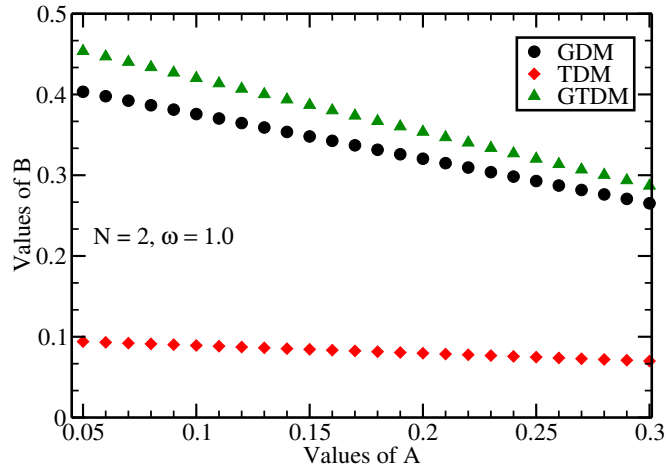
Figure 2.3: Correlation between two parameters *A* and *B* for two electron parabolic quantum dot with $\omega = 1$ is plotted for all the functionals.

the enhancement factor like term present within square bracket.

Mixing the local contribution from Eq.(2.37) and the non-uniformity via Eq.(2.40), a new spin-polarized correlation energy functional is written as,

$$E_{c,\sigma}^{NIL} = \frac{1}{2} \sum_{\sigma=\uparrow,\downarrow} \int d^2r \, \varepsilon_{c,\sigma}^{LDA}(r_s, \zeta) \mathbf{F}_{\mathbf{c},\sigma}(x_\sigma, z_\sigma). \tag{2.41}$$

Where

$$F_{c,\sigma} = \frac{L}{\Gamma_\sigma} + \frac{M \, 4\rho_\sigma \mathscr{G}_\sigma(x_\sigma, z_\sigma)}{5k_F^2 \Gamma_\sigma^3} + \frac{N \, 48\rho_\sigma^2 \mathscr{G}_\sigma^2(x_\sigma, z_\sigma)}{35k_F^4 \Gamma_\sigma^5}. \tag{2.42}$$

Here, $\mathbf{F}_{\mathbf{c},\sigma}$ is a dimensionless quantity and has no dimensional effect on any multiplied physical quantity. After assigning appropriate values to all the parameters the above non-local effect induced LDA correlation functional $E_{c,\sigma}^{NIL}$ will be completed. This task will be completed in the next section by comparing the result with the exact values for the parabolic quantum dots.

2.3.3 Numerical Demonstration - II

Similar to the previous section, we demonstrate the efficiency of these parameterized functionals by applying them on parabolically confined QDs, also known as artificial atoms having external potential as $\omega^2 r^2/2$, ω being the confinement strength. The SCF

Table 2.5: The exchange energies (in a.u.) of parabolic quantum dots as obtained from proposed exchange energy functionals $-E_x^{GDM}$, $-E_x^{TDM}$, and $-E_x^{GTDM}$. The first column is for the number of electrons 'N', 2nd is for confinement strength ω. The self-consistent results for 2D-EXX (KLI), 2D-LDA, 2D modified B86, 2D-B88 are shown in succeeding columns. The last row contains the MAPE (Δ).

N	ω	$-E_x^{2D-EXX}$	$-E_x^{2D-LDA}$	$-E_x^{2D-B86}$	$-E_x^{2D-B88}$	$-E_x^{2D-GDM}$	$-E_x^{2D-TDM}$	$-E_x^{2D-GTDM}$
2	1/6	0.380	0.337	0.368	0.364	0.387	0.387	0.387
2	0.25	0.485	0.431	0.470	0.464	0.492	0.492	0.492
2	0.50	0.729	0.649	0.707	0.699	0.736	0.736	0.736
2	1.00	1.083	0.967	1.051	1.039	1.086	1.086	1.086
2	1.50	1.358	1.214	1.319	1.344	1.354	1.354	1.354
2	2.50	1.797	1.610	1.748	1.728	1.772	1.772	1.772
2	3.50	2.157	1.934	2.097	2.074	2.100	2.101	2.100
6	0.25	1.618	1.531	1.603	1.594	1.640	1.634	1.638
6	0.50	2.470	2.339	2.444	2.431	2.496	2.487	2.491
6	1.00	3.732	3.537	3.690	3.742	3.758	3.747	3.751
6	1.50	4.726	4.482	4.672	4.648	4.750	4.737	4.741
6	2.50	6.331	6.008	6.258	6.226	6.340	6.325	6.328
6	3.50	7.651	7.264	7.562	7.525	7.630	7.620	7.619
12	0.50	5.431	5.257	5.406	5.387	5.458	5.451	5.448
12	1.00	8.275	8.013	8.230	8.311	8.295	8.285	8.279
12	1.50	10.535	10.206	10.476	10.444	10.541	10.529	10.521
12	2.50	14.204	13.765	14.122	14.080	14.163	14.146	14.136
12	3.50	17.237	16.709	17.136	17.165	17.133	17.108	17.103
20	0.50	9.765	9.553	9.746	9.819	9.803	9.794	9.788
20	1.00	14.957	14.638	14.919	15.014	14.991	14.979	14.968
20	1.50	19.108	18.704	19.053	19.159	19.131	19.116	19.101
20	2.50	25.875	25.334	25.796	25.973	25.854	25.838	25.817
20	3.50	31.491	30.837	31.392	31.603	31.399	31.399	31.365
42	1.00	35.513	35.099	35.503	35.671	35.590	35.547	35.520
42	1.50	45.560	45.032	45.538	45.747	45.589	45.572	45.539
42	2.50	62.051	61.339	62.007	62.286	62.005	61.989	61.944
42	3.50	75.814	74.946	75.748	76.085	75.674	75.622	75.592
56	1.00	49.710	49.256	49.722	49.919	49.757	49.744	49.709
56	1.50	63.869	63.289	63.871	64.117	63.885	63.867	63.824
56	2.50	87.164	86.378	87.148	87.479	87.076	87.040	86.994
56	3.50	106.639	105.684	106.609	107.010	106.408	106.330	106.309
72	1.00	66.708	66.219	66.746	66.972	66.772	66.758	66.716
72	1.50	85.814	85.186	85.844	86.129	85.850	85.832	85.781
72	2.50	117.312	116.456	117.327	117.712	117.260	117.228	117.171
72	3.50	143.696	142.650	143.697	144.163	143.519	143.426	143.406
90	1.00	86.631	86.111	86.698	86.954	86.697	86.682	86.633
90	1.50	111.558	110.889	111.622	111.946	111.585	111.566	111.504
90	2.50	152.723	151.808	152.779	153.217	152.608	152.593	152.515
90	3.50	187.262	186.139	187.306	187.838	186.974	186.869	186.844
110	1.00	109.595	109.048	109.695	109.981	109.681	109.666	109.609
110	1.50	141.255	140.548	141.357	141.720	141.304	141.283	141.214
110	2.50	193.617	192.647	193.715	194.210	193.526	193.515	193.421
110	3.50	237.612	236.420	237.706	238.306	237.369	237.263	237.223
Δ			4.2	0.71	1.04	**0.39**	**0.36**	**0.38**

results for 2D-LDA,[81] 2D-B88,[83] and 2D-modified GGA[84] along with the EXX results for these systems are presented again in Table2.5, similar to Table 2.2. The exchange energies for these QDs having electrons from 2 to 110 and the confinement strength from 0.25 to 3.5 are shown considering above mentioned available functionals, and newly constructed functionals.

Before going to results, the first task is to get appropriate values of all the constants present in the exchange and correlation energy functionals. There are four adjustable parameters A, B, λ, and α present in all the three exchange energy functionals E_x^{GDM}, E_x^{TDM}, and E_x^{GTDM}. For all the cases, the parameter λ that is defined for the localization of the exchange hole is chosen to be 0.5, and this value corresponds to maximally localized exchange hole. The LSDA like term present as the first term in all the exchange energy functionals contains parameter α via the modified k. To add some non-uniformity in the Fermi momentum k_F, the parameter α is introduced. So, we expect the effect of all the increasing ordered terms to decrease gradually. Keeping this in mind, and by taking $A = B = 0$, we fix $\alpha = 0.001$. Also, we observe that for higher values ($\alpha > 0.001$), the calculated exchange energies differ more from the exact values in case of smaller ω valued QDs. To fix other two parameters A and B, a two-dimensional scan is performed for understanding their interdependency. For this, we show the variation of A and B depending on each other in Figure 2.3, and it is observed that they are negatively correlated. Also, there exists a B for every value of fixed parameter A that leads to exact exchange energy. we have two observations: (i) for $A > 0.5$, the exchange energies of higher electron systems differs from the exact, and (ii) for $A < 0.1$, the exchange energies for lesser number of confined electrons differs from the exact values. Analyzing above points, we fix $A = 0.02$. With $\alpha = 0.001$ and $A = 0.2$, exchange energies of only two electron QDs (present in Table 2.5) are calculated taking different values of B. The mean of all B's that gives the exchange energy same as the EXX is concluded as the final value. We follow the same procedure to fix the parameters in case of all exchange energy functionals and values for these parameters are tabulated in Table 2.4.

In Table 2.5, we present the number of electrons (N), confinement strength (ω) in first two columns. Then exchange energies of four known functionals, and three newly pro-
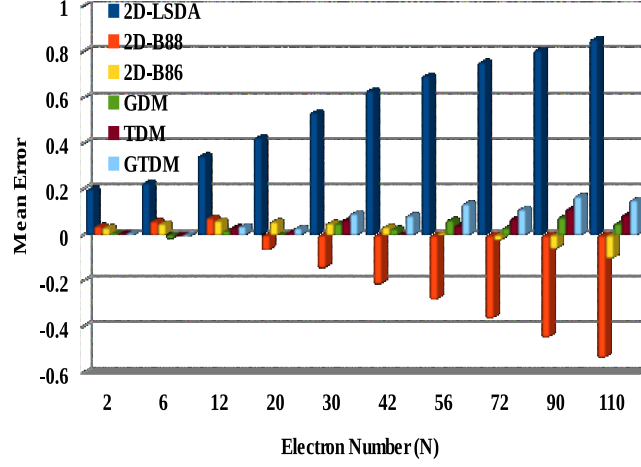
Figure 2.4: The mean errors of exchange energies as obtained from different functionals are shown for parabolic quantum dots.

posed functionals are tabulated in subsequent columns. The MAPE for all the functionals are given in the last row for comparison. It is clear from Table 2.5 that the new functionals are very competitive and give better exchange energies. The MAPE of Exchange energy functional E_x^{GDM}, E_x^{TDM}, and E_x^{GTDM} are 0.39, 0.36, and 0.38 respectively for all 46 calculations. The mean error for these functionals are shown in Figure 2.4. The heights of different color bars represent the ME corresponding to the exchange energy functionals considered in the present study.

Similar to exchange energy functionals, the correlation energy functional $E_{c,\sigma}^{NIL}$ from Eq.(2.41) also contains four parameters as, δ, L, M, and N. We fix these parameters by comparing with the exact correlation energy of QDs. In DFT, we can get the correlation energy from the total energy , and the EXX, as $E_c^{ref} = E_{tot}^{ref} - E_{tot}^{EXX}$, where E_{tot}^{ref} is the exact total energy of the system and E_{tot}^{EXX} is the total energy of the system taking taking only exact exchange. First, keeping $M = N = 0$, and calculating two extreme cases of smaller ($N = 2$, $\omega = 1/6$) and larger ($N = 6$, $\omega = 0.42168$) QDs, we fix the values of δ and L. Then a model of a practical QD is considered for fixing M and N. This QD is modeled with parabolic potential with $N = 6$, and $\omega = 0.42168$, and it represent a GaAs QD[93] having 5*mev* confinement strength. The final value for these constants are $\delta = 0.001, L = 0.86, M = 0.07$, and $N = 0.0448$. We tabulated the correlation energies for two,

Table 2.6: The first two columns list the number of electrons and the confinement strength (ω). Results for two local correlation functionals 2D-LDA[65] and 2D-PRM[85] are given in 6th and 7th columns respectively. Other following columns are for both XC energies. The sources for the reference values are given below in this table.

N	ω	E_{tot}^{ref*}	E_{tot}^{2D-EXX}	$-E_c^{ref}$	$-E_c^{2D-LDA}$	$-E_c^{2D-PRM}$	$-E_c^{NIL}$	$-E_{xc}^{ref†}$	$-E_{xc}^{LDA}$	$-E_{xc}^{B86-PRM**}$	$-E_{xc}^{mod}$
2	1/6	$2/3^a$	0.7686	0.1020	0.1221	0.1100	0.1024	0.4936	0.4721	0.5000	0.4894
2	0.25	0.9324^b	1.0462	0.1138	0.1390	0.1230	0.1169	0.5987	0.5819	0.6146	0.6089
2	1.00	3^a	3.1619	0.1619	0.1987	0.1632	0.1660	1.246	1.1737	1.2355	1.2520
6	0.25	6.995^b	7.3910	0.3960	0.4574	0.3990	0.3880	2.014	2.0112	2.0430	2.0260
6	$1/1.89^2$	7.6001^c	8.0211	0.4210	0.4732	0.4103	0.4015	2.156	2.1372	2.1683	2.1568
6	0.42168	10.37^d	10.8204	0.4504	0.5305	0.4493	0.4504	2.6784	2.6604	2.6905	2.7003
12	0.25	23.6548^e	24.5129	0.8581	0.9680	0.8363	0.8239	4.3957	4.4228	4.4130	4.3820
12	0.50	39.211^e	40.2231	1.0121	1.1665	0.9664	0.9932	6.4453	6.4525	6.4151	6.4512
12	1.00	65.768^e	66.9130	1.1450	1.3555	1.0745	1.1530	9.4204	9.3923	9.3396	9.4460
Δ	–	–	–	–	17.41	3.73	2.09	–	1.74	1.00	0.57

* The reference results are discussed in References[85,86,87]
† $E_{xc}^{ref} = E_x^{2D-EXX} + E_c^{ref}$
** Self consistent calculation with 2D-B86[84] exchange and 2D-PRM[85] correlation functionals.
a-Analytic solution by Taut from Ref..[88]
b-CI data from Ref..[89]
c-Diffusion QMC data from Ref..[90]
d-Variational QMC data from Ref..[91]
e-Variational QMC data from Ref..[92]

six and twelve electrons in Table 2.6. Two local-type correlation functionals[65,85] along with the reference values are shown in the same table for comparison. In addition, the exchange-correlation values for E_{xc}^{mod} combining E_x^{GTDM} exchange, and $E_{c,\sigma}^{NIL}$ correlation is also shown in the same table, and similar result is expected from both E_x^{GDM} and E_x^{TDM}. The self consistent exchange-correlation energies of $E_{XC}^{LDA} = E_x^{2D-LDA} + E_c^{2D-LDA}$ and $E_{XC}^{B86-PRM} = E_x^{2D-B86} + E_c^{2D-PRM}$ are also presented for comparison. It is observed from Fig 2.4 that the exchange functionals E_x^{GDM}, E_x^{TDM} and E_x^{GTDM} have positive mean error for the higher number of electrons. Hence, for these systems some part of these ME will be compensated by negative mean error of $E_{c,\sigma}^{NIL}$. Also the mean error cancellation in case of LSDA is clearly easily perceived from Table 2.6. The MAPE for the constructed correlation functional is recognizable in Table 2.6. Also the combination of the exchange, and correlation energy functional E_{xc}^{mod} agrees well with the reference values in parabolic quantum dots.

Up to now, we have discussed the exchange energy functionals constructed from the DME, and a correlation energy functional developed from the combination of LSDA and enhancement factor from DME. In the next section, we propose a correlation energy functional that can be used with other available 2D exchange energy functionals. The basis of the construction is Colle-Salvetti-type correlated wave functions. Also, a special case with the vanishing density gradient is analyzed.

2.4 Colle-Salvetti type correlation functionals in two dimensions

Among different construction methods, the use of correlated wavefunction to construct the correlation energy functional has been proved to be very successful. This correlated many-particle wavefunction having single determinant Hartree-Fock function used by Colle and Salvetti[94,95] to construct the correlation energy functionals. As required, such form of wavefunction able to take care of the correlation energy between the different spin pair electrons. A method in this direction is developed by Tsuneda et al.[96,97] that

assimilates the correlation between similar, and opposite pair of electrons. Satisfying the electron-electron cusp condition,[98] this type of very effective wavefunction is written as,

$$\Psi_{\sigma_1\sigma_2}(\mathbf{x}_1, \mathbf{x}_2..., \mathbf{x}_N) = \Psi_{\sigma_1\sigma_2}^{HF}(\mathbf{x}_1, \mathbf{x}_2..., \mathbf{x}_N) \times \prod_{i>j}[1 - \varphi_{\sigma_1\sigma_2}(\mathbf{r}_i, \mathbf{r}_j)], \qquad (2.43)$$

where $\mathbf{x}_i$ is the spatial-spin-coordinate of the ith electron, and $\mathbf{r}_i$ is the spatial part, σ_1 and, σ_2 are two spin components. The $\Psi_{\sigma_1\sigma_2}^{HF}$ is defined as a spin-polarized one-determinant HF wavefunction. The form of $\varphi_{\sigma_1\sigma_2}(\mathbf{r}_i, \mathbf{r}_j)$ imposes the electronic cusp conditions to be satisfied by the wavefunction. For opposite spin pairs, the form of 'φ' in relative $r = |\mathbf{r}_i - \mathbf{r}_j|$ and center of mass $\mathbf{R} = (\mathbf{r}_i + \mathbf{r}_j)/2$ coordinates is given by,[96]

$$\varphi_{\sigma_1\sigma_2}(\mathbf{R}, r) = e^{-\beta_{\sigma_1\sigma_2}^2 r^2}[1 - \Phi_{\sigma_1\sigma_2}(\mathbf{R})(1 + \alpha r)]. \qquad (2.44)$$

Here, the correlation potential can be controlled by both $\Phi_{\sigma_1\sigma_2}$ and the parameter $\beta_{\sigma_1\sigma_2}$, and the parameter α is used to impose the cusp conditions via the pair correlation function. A obvious observation from Eq.(2.43) and Eq.(2.44) is that, Eq.(2.43) will reduce to Ψ^{HF} if the distance between two electrons is very large, and hence the electrons are barely correlated. Similarly, when the pair of electrons share the same spatial positions, i.e., $\mathbf{r}_i \to \mathbf{r}_j$, the function becomes,

$$\Psi = \Psi^{HF}\Phi(\mathbf{R}).$$

The value of α present in Eq.(2.44) is settled as one in two dimensions,[85] to satisfy the pair correlation cusp conditions.[98] The approximated form of Φ, as shown in,[85]

$$\Phi(\mathbf{R}) \simeq \frac{\sqrt{\pi}\beta}{\sqrt{\pi}\beta + \pi/2}, \qquad (2.45)$$

and it is deduced by imposing the condition,

$$\int d^2\mathbf{r}\, \varphi(\mathbf{R}, r) = 0. \qquad (2.46)$$

The parameter β being the crucial parts of the correlation energy, is determined by following a method used in 3D,[96] and it makes the form of β more adaptable. To fix β, we start with the exchange energy of the form

$$E_x \equiv -\frac{1}{2} \sum_\sigma \int \rho_\sigma \langle r_\sigma^{-1} \rangle \, d^2\mathbf{R}, \tag{2.47}$$

the correlation length proposed by Becke[82] in 3D and Pittalis et al. in 2D,[86] is given as,

$$Z_{\sigma_1 \sigma_2} = C_{\sigma_1 \sigma_2} \left(\frac{1}{\langle r_{\sigma_1}^{-1} \rangle} + \frac{1}{\langle r_{\sigma_2}^{-1} \rangle} \right), \tag{2.48}$$

where $C_{\sigma_1 \sigma_2}$ is the proportionality constant, ρ_σ is the electron density of spin σ and $\langle r_\sigma^{-1} \rangle$ is the mean inverse radius of Fermi hole. In 2D, the form of B88[79] functional is given as,

$$E_x^{2D-B88} = -\frac{1}{2} \sum_\sigma \int d^2r \rho_\sigma^{3/2} \left(\frac{16}{3\sqrt{\pi}} + \frac{\gamma_{2D} \widetilde{x}_\sigma^2}{1 + 8\gamma_{2D} \widetilde{x}_\sigma \sinh^{-1} \widetilde{x}_\sigma} \right). \tag{2.49}$$

Here, $\widetilde{x}_\sigma = \frac{|\nabla \rho_\sigma|}{\rho_\sigma^{3/2}}$ is the reduced density gradient, and the value of the constant $\gamma_{2D} = 0.007$. The Eq.(2.49) is written as,

$$E_x^{2D-B88} = -\frac{1}{2} \sum_\sigma \int d^2r \rho_\sigma (\rho_\sigma^{1/2} K_\sigma), \tag{2.50}$$

and K_σ follows the mathematical expression present within parenthesis in Eq.(2.49). Now, comparing equations (2.47), (2.48), and (2.50), the correlation length in 2D is written as

$$Z_{\sigma_1 \sigma_2} = C_{\sigma_1 \sigma_2} (\rho_{\sigma_1}^{-1/2} K_{\sigma_1}^{-1} + \rho_{\sigma_2}^{-1/2} K_{\sigma_2}^{-1}). \tag{2.51}$$

The concept of the correlation length can be used to calculate β, and hence the exchange energy dependent β can be used in the correlation energy. For this, it can be thought that, the area A, where the correlation energy or $\varphi_{\sigma_1 \sigma_2}(\mathbf{r}_i, \mathbf{r}_j)$ deviates well from zero is expressed as[85]

$$A = 2\pi \int e^{-\beta^2 r^2} r \, dr = \frac{\pi}{\beta^2}. \tag{2.52}$$

If the area of the exchange energy is assumed to be proportional to the area of the circle having the radius half of the correlation length, then

$$A_{\sigma_1 \sigma_2} = \pi (Z_{\sigma_1 \sigma_2}/2)^2. \tag{2.53}$$

Using Eq.(2.52), Eq.(2.53), and the form of $Z_{\sigma_1 \sigma_2}$, we have

$$\beta_{\sigma_1 \sigma_2} = q_{\sigma_1 \sigma_2} \left(\frac{K_{\sigma_1} \rho_{\sigma_1}^{1/2} K_{\sigma_2} \rho_{\sigma_2}^{1/2}}{K_{\sigma_2} \rho_{\sigma_2}^{1/2} + K_{\sigma_1} \rho_{\sigma_1}^{1/2}} \right). \tag{2.54}$$

The proportionality constant $q_{\sigma_1 \sigma_2}$ determines the correlation length. Now the exponent of Eq.(2.44), i.e., $\beta_{\sigma_1 \sigma_2}$ will have the form of Eq.(2.54) along with Becke's K_σ. So, from Eq.(2.43) and Eq.(2.44), the correlation energy is expressed as,

$$E_{\sigma_1 \sigma_2}^c = -\int P_{2HF}^{\sigma_1 \sigma_2}(\mathbf{r}_1, \mathbf{r}_2)[2\varphi_{\sigma_1 \sigma_2}(\mathbf{r}_1, \mathbf{r}_2) - \varphi_{\sigma_1 \sigma_2}^2(\mathbf{r}_1, \mathbf{r}_2)](1/r)\, d^2 r_1\, d^2 r_2, \tag{2.55}$$

$P_{2HF}^{\sigma_1 \sigma_2}(\mathbf{r}_1, \mathbf{r}_2)$ being the second-order reduced density matrix, which is obtained by multiplying Ψ^{HF} to itself. Taking Taylor expansion of a function up to second order, a general equation can be written as[94]

$$\int e^{-\beta^2 r^2}(1/r)F(\mathbf{r}, \mathbf{R})d\mathbf{r} = 2\pi F(0, \mathbf{R}) \int e^{-\beta^2 r^2} dr + \frac{\pi}{2}(\nabla_\mathbf{r}^2 F(\mathbf{r}, \mathbf{R}))_{r=0} \int e^{-\beta^2 r^2} r^2 dr. \tag{2.56}$$

The above identity Eq.(2.56) can be projected on Eq.(2.55), as a result,

$$E_{\sigma_1 \sigma_2}^c = -\pi \int \rho_{\sigma_1} \rho_{\sigma_2} \Big[2 \int e^{-\beta^2 r^2}\{1 - \Phi(1+r)\}dr - \int e^{-2\beta^2 r^2}\{1 - \Phi(1+r)\}^2 dr +$$
$$\frac{L_{\sigma_1 \sigma_2}}{2} \int e^{-\beta^2 r^2}\{1 - \Phi(1+r)\}r^2 dr - \frac{L_{\sigma_1 \sigma_2}}{4} \int e^{-2\beta^2 r^2}\{1 - \Phi(1+r)\}^2 r^2 dr \Big] d^2 \mathbf{R}, \tag{2.57}$$

where

$$L_{\sigma_1 \sigma_2} = \frac{[\nabla_r^2 P_{2HF}^{\sigma_1 \sigma_2}(\mathbf{R} + \frac{\mathbf{r}}{2}, \mathbf{R} - \frac{\mathbf{r}}{2})]_{r=0}}{\rho_{\sigma_1}(\mathbf{R})\rho_{\sigma_2}(\mathbf{R})}. \tag{2.58}$$

In the present study, the correlation energy only between two opposite pair of electrons is considered. This is because the correlation energy between the same spin oriented electrons will vanish due to Pauli's exclusion principle, if, we terminate the Taylor expansion of Eq.(2.56) up to first order. To derive the above Eq.(2.57), we have used the relations $P_{2HF}^{\sigma_1 \sigma_2}(\mathbf{R}, \mathbf{R}) = \rho_{\sigma_1}(\mathbf{R}) \rho_{\sigma_2}(\mathbf{R})/2$ and $P_{2HF}^{\sigma \sigma}(\mathbf{R}, \mathbf{R}) = 0$. Now, to evaluate the Eq.(2.57), we use the value of β from Eq.(2.54), and neglected some insignificant valued terms ($\simeq 0$). Then the correlation energy term reduces to,

$$E_{\sigma_1 \sigma_2}^c = -\int \left(\frac{\rho_{\sigma_1}^{1/2}}{K_{\sigma_2}} + \frac{\rho_{\sigma_2}^{1/2}}{K_{\sigma_1}} \right)^2 \frac{1.793 + 0.942/\beta_{\sigma_1 \sigma_2} - \mathbf{M}_{\sigma_1 \sigma_2}(0.168 + 0.164/\beta_{\sigma_1 \sigma_2})}{(q_{\sigma_1 \sigma_2})^2 (1 + 1.772/\beta_{\sigma_1 \sigma_2} + 0.785/\beta_{\sigma_1 \sigma_2}^2)} \, d^2\mathbf{R},$$

$$(2.59)$$

where $\mathbf{M}_{\sigma_1 \sigma_2}(\mathbf{R}) = L_{\sigma_1 \sigma_2}(\mathbf{R})/\beta_{\sigma_1 \sigma_2}^2(\mathbf{R})$.

To make a very simple form, we further approximate Eq.(2.59) with the help of one of the principal CS scheme as used before in the references.[94,96] Then the form changes to,

$$E_{\sigma_1 \sigma_2}^c = -\int \left(\frac{\rho_{\sigma_1}^{1/2}}{K_{\sigma_2}} + \frac{\rho_{\sigma_2}^{1/2}}{K_{\sigma_1}} \right)^2 \frac{a + c\mathbf{M}_{\sigma_1 \sigma_2} e^{-d/\beta}}{1 + b/\beta} \, d^2\mathbf{R}. \qquad (2.60)$$

Here, a, b, c, and d are constants, and they will be fixed in the next section by comparing with reference energies. Taking $\{\alpha, \beta\}$ spins for σ_1, σ_2 electrons and imposing the condition $E_{\alpha,\beta}^c = E_{\beta,\alpha}^c$, the total correlation energy is written as

$$E^c[\rho_\alpha, \rho_\beta] = 2E_{\alpha,\beta}^c. \qquad (2.61)$$

It is to be noted that, previously a correlation energy functional is derived for 2D systems based on CS scheme, and using the correlated wavefunction by Pittalis, Räsänen, and Marques (PRM).[85] They approximated the underlying pair density[99] as a Gaussian approximation, and made the functional local, and electron number (N) dependent. But in our case, the correlation energy Eq.(2.60) depends on the gradient of density, and independent of confined electron number. Here, an option arises to model the PRM functional by the inclusion gradient dependent β from Eq.(2.54). However, such modification able to produce accurate correlation energies for less number of confined electrons, but the

Table 2.7: The correlation energies (in a.u.) of parabolic quantum dots. The confinement electron number, confinement strength, total energy, total exact exchange, and reference correlation energies are tabulated from first to fifth columns. The correlation energies of newly proposed functionals E_c^{GCS} and E_c^{LCS} are given in the last two columns. The last row is for the Δ.

N	ω	E_{tot}^{ref}	E_{tot}^{EXX}	$-E_c^{ref}$	$-E_c^{AMGB}$	$-E_c^{PRM}$	$-E_c^{GCS}$	$-E_c^{LCS}$
2	1/6	$2/3^a$	0.7686	0.1020	0.1221	0.1100	0.1012	0.1019
2	0.25	0.9324^b	1.0462	0.1138	0.1390	0.1230	0.1156	0.1172
2	1.00	3^a	3.1619	0.1619	0.1987	0.1632	0.1618	0.1677
6	0.25	6.995^c	7.3910	0.3960	0.4574	0.3990	0.3895	0.3870
6	$1/1.89^2$	7.6001^d	8.0211	0.4210	0.4732	0.4103	0.4029	0.4009
6	0.42168	10.37^e	10.8204	0.4504	0.5305	0.4493	0.4504	0.4504
6	1.00	20.1821^c	20.7223	0.5402	0.6476	0.5204	0.5409	0.5465
12	0.25	23.6548^c	24.5129	0.8581	0.9680	0.8363	0.8324	0.8210
12	$1/1.89^2$	25.636^d	26.5532	0.9172	1.0000	0.8583	0.8593	0.8486
12	0.50	39.211^c	40.2231	1.0121	1.1665	0.9664	0.9953	0.9891
12	1.00	65.768^c	66.9130	1.1450	1.3555	1.0745	1.1396	1.1405
20	0.25	57.2088^c	58.8188	1.6101	1.6956	1.4527	1.4648	1.4401
20	0.50	93.9838^c	95.7435	1.7597	2.0144	1.6538	1.7255	1.7078
20	1.00	156.030^c	158.0235	1.9935	2.3301	1.8288	1.9648	1.9570
30	0.5	187.2425^c	189.9525	2.7095	3.1042	2.5303	2.6628	2.6294
30	1.0	308.832^c	311.9588	3.1268	3.5769	2.7854	3.0179	2.9978
30	2.0	515.976^c	519.2705	3.2945	3.9938	2.9779	3.2987	3.2933
Δ					16.03	5.57	**2.21**	**2.72**

a-Analytic solution by Taut from Ref. [88].
b-CI data from Ref. [89].
c-Variational Monte-Carlo data from Ref. [92].
d-Diffusion QMC data from Ref. [90].
e-Variational QMC data from Ref. [91].

error increases with the increase of *N*. So, we are skipping the results for such modified form of PRM functional.

To fix the parameters, we start with the parameter *c* attached to **M**(Eq.(2.60). For a simple functional form and to avoid the Laplacian of the second order density matrix, we assign $c = 0$. Also, such choice of *c* changes the correlation energy to a new form which would be same as the form obtained by terminating Eq.(2.56) only at first order. So, not considering the other higher order terms, the correlation energy only takes care the coulomb correlation between two opposite spin-electrons, and it makes one to think

all the equal spin correlation effects are considered by the exchange energy part of the E_{xc}. However, for $c \neq 0$, one can follow a procedure by Lee, Yang, and Parr[51] to use the Laplacian of density matrix as a progressive part that depends of orbital free form of the kinetic energy density. Due to unavailability of advance only-density dependent kinetic energy functional, we fix $c = 0$ as final option. This value of c implies no need to fix the parameter d. So, imposing the above parameters on Eq.(2.60), the gradient dependent Colle-Salvetti (GCS) correlation functional (E_c^{GCS}) is written as,

$$E_c^{GCS} = -\int \left(\frac{\rho_{\sigma_1}^{1/2}}{K_{\sigma_2}} + \frac{\rho_{\sigma_2}^{1/2}}{K_{\sigma_1}} \right)^2 \frac{a}{1 + x/\beta'} \, d^2\mathbf{R}, \tag{2.62}$$

where $\beta' = (K_{\sigma_1}\rho_{\sigma_1}^{1/2} K_{\sigma_2}\rho_{\sigma_2}^{1/2})/(K_{\sigma_2}\rho_{\sigma_2}^{1/2} + K_{\sigma_1}\rho_{\sigma_1}^{1/2})$ and x is the resulting constant of b and $q_{\sigma_1\sigma_2}$.

Also, we present one special case of this gradient dependent correlation functional E_c^{GCS} by forcing the density gradient to zero for the local density case. So, using $\nabla\rho_\sigma = 0$ in K_σ of 2D-B88, $K_\sigma[\rho_\sigma]$ changes into a constant. Hence, E_c^{GCS} modifies to a local type correlation functional that depends on the density and two adjustable parameters. We name it as local-Colle-Salvetti (LCS) correlation functional E_c^{LCS}. We discuss the numerical correlation energy results for both these functionals below.

2.4.1   Numerical Demonstration - III

The 2D parabolic QDs are also used here to examine the effectiveness of these correlation functionals. Before going to evaluate the correlation energies, we need to fix the parameters a, and x present in these energy expression Eq.(2.62). First considering the real GaAs QD analogous 6-electron QD with $\omega = 0.42168$, a rough values of a and x are determined. As we have only two parameters, a in numerator and x in the denominator, there always exist a value of x for any fractional value of a that will give the exact reference correlation energy (QMC). So for the above mentioned QD, we calculate the correlation energies by varying a from 0.1 to 0.2 with corresponding values of x. The extracted pairs of a and x are used to calculate correlation energies for the first two closed shell QDs (present in
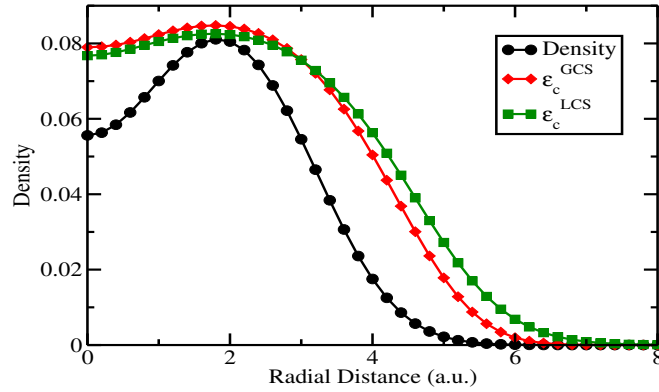
Figure 2.5: Correlation energy densities of E_c^{GCS} and E_c^{LCS} are plotted along with the exact density of a parabolic quantum dot having $N = 6$ and $\omega = 0.42168$.

Table 2.7), and the optimized values are taken by comparison with corresponding QMC references. The final values of these two constants are determined to be $a = 0.156$ and $x = 0.2643$. Also the Same procedure is followed to fix the parameters E_c^{LCS}, and are determined to be $a = 0.155$ and $x = 0.2783$.

To examine the nature of variation of the correlation energy densities of these constructed functionals with the electron density, we plot the correlation energy density of both E_c^{GCS}, and E_c^{LCS} along with the exact density in Figure 2.5. A parabolic QD with $N = 6$, and $\omega = 0.42168$ is considered for this figure. It is clearly observed from Figure 2.5 that energy densities of both LCS, and GCS have smooth decay in the tail of density. The faster decay of E_c^{GCS} compare to E_c^{LCS} shows the effect of presence of the gradient of density. Also, for the same QD, we plot the correlation energy densities with the correlation length $1/\beta'$ in Figure 2.6. The used correlation length β' is different from β in the way that in β' no proportionality constant is used. Our correlation length depends inversely on both K_σ, and the square root of density. As a result, the correlation length for LCS increases rapidly with the decrease of density (and constant K_σ). But the rapidness is compensated by the presence of K_σ in case of GCS. Due to different scaling, we plot the correlation energy density for LCS in the inset of Figure 2.6. It is observed that both ε_c^{GCS} and ε_c^{LCS} start around 0.08, but decay in different ways. GCS energy density decays quickly almost to zero at 27, whereas the LCS energy density decays slowly to zero at above 500. In both the cases, the correlation contribution is higher for small values of the
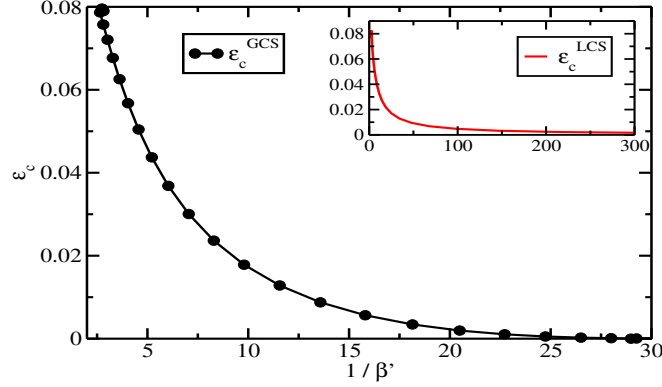
Figure 2.6: The variation of correlation energy densities with the correlation length for the same quantum dot as 2.5.

Table 2.8: The MAPE for the exchange-correlation functionals constructed by combining four 2D-meta-GGA exchanges and four correlation functionals are shown. The correlation functionals are in the first column, and exchange energy functionals are in the top row. The quantum dots that are shown in Table 2.7 are used for the calculations.

	E_x^{GDM}	E_x^{TDM}	E_x^{GTDM}	E_x^{PF}
E_c^{AMGB}	3.04	2.92	2.93	2.49
E_c^{PRM}	0.95	0.92	0.98	0.64
E_c^{GCS}	**0.48**	**0.43**	**0.48**	0.43
E_c^{LCS}	0.79	0.71	0.75	**0.42**

E_x^{GDM}, E_x^{TDM}, and E_x^{GTDM} are from reference [100]
E_x^{PF} from reference [101]

correlation length, and it decreases as the correlation length increases.

Now, we apply these two correlation energy functionals to parabolic QDs, and the energy are tabulated in Table 2.7. Similar to the discussed exchange energy functionals, the correlation energy functionals for QDs are calculated with spin-DFT implemented within the OCTOPUS[80] code. Similar to Table 2.6, the reference correlation energies are calculated, and the output density of EXX is used as input for the correlation energy functionals E_c^{GCS}, and E_c^{LCS}. Use of these inputs in a post-hoc manner is acceptable and discussed in Ref. [86]. The SCF energies for two local correlation functionals Attaccalite-Moroni-Gori-Giorgi-Bachelet(AMGB)[65] and PRM are also calculated and presented in Table 2.7. In this table, the correlation energies of QD are presented by varying the confined electron
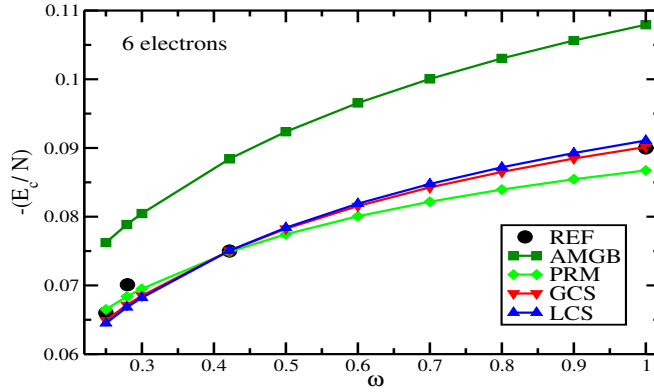
Figure 2.7: Shown are the correlation energies per electron for six electron parabolic quantum dots with different confinement strengths.

number N and confinement strength ω. The correlation energies for E_c^{GCS}, and E_c^{LCS} as given in last two columns along with AMGB, PRM, and reference values can be compared for the efficiency of new development. From the MAPE (given in the last row), following clear observation can be made. The 2D-LDA functional, i.e., E_c^{AMGB} has the maximum error. The functional E_c^{PRM} is more accurate than AMGB, and the proposed functionals E_c^{GCS} and E_c^{LCS} outdated these local functionals. Also, by comparing LCS and GCS, the usefulness of gradient of density is realized as E_c^{GCS} gives more accurate correlation energies with MAPE of 2.21, i.e, the best error value. The more advantages of using GCS, and LCS is that for more confinement electrons, the difference between the exact and the calculated correlation energies decreases. To test the compatibility with the exchange energy functionals, we add these correlation energies to previously developed mGGA type exchange energy functionals E_x^{2D-GDM}(2.32), E_x^{2D-TDM}(2.34), $E_x^{2D-GTDM}$(2.36), and E_x^{PF-KS}(combination of 2.20, and 2.21. 2.20 is used for 2 electron quantum dots and 2.21 used for other quantum dots). In Table 2.8, we present the MAPE for these 2D-E$_{xc}$. E_c^{GCS} correlation functional is appropriate for all the meta-GGA exchange energy functionals and it has the minimum MAPE for all the cases except the combination with E_x^{PF}.

In Figure 2.7, the correlation energy per particle is plotted for AMGB, PRM, LCS, and GCS functionals. Proposed functionals E_c^{GCS} and E_c^{LCS} follow the reference values more closely. To understand the usefullness of these functionals in 2D homogeneous
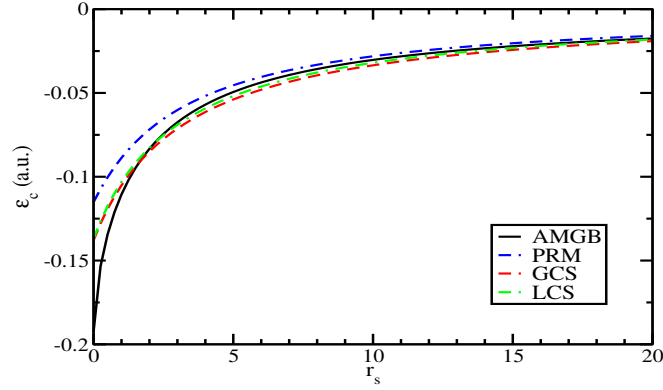
Figure 2.8: Correlation energy per electron as a function of r_s for the 2D uniform electron gas using different functionals.

electron gas limit, in Fig. 2.8, we plot the correlation energy per electron as a function of $r_s = 1/\sqrt{\pi\rho}$. For homogeneous limit, the reference functional is 2D-AMGB. From Fig. 2.8, it is clear that both GCS and LCS excellently match with the reference AMGB and only differ at very weak correlation limit, i.e, at very small value of r_s. We believe the newly constructed correlation functionals are propitious for the higher number of electronic systems. E_c^{GCS} functional has advantages over E_c^{LCS} functional due to the gradient of density effect.

2.4.2 Fundamental conditions

Here, we want to test ability of the proposed correlation functionals E_c^{GCS} and E_c^{LCS} to satisfy some fundamental conditions and scaling relations that exact correlation energy functional should obey.

(a) For a given density, the correlation energy is less than or equal to zero, i.e.,

$$E_c[\rho] \leq 0. \tag{2.63}$$

For negative correlation energy, the terms within the integral of Eq.(2.62) must be positive. The constants a and x present in Eq.(2.62) are positive, and the first term is positive due to the presence of square. Also, K_σ present in β' is always positive, as

the exchange energy Eq.(2.50) is negative. So, for any given density, the correlation functionals, E_c^{GCS} and E_c^{LCS} obey the important condition Eq.(2.63).

(b) By scaling all the coordinates uniformly, the scaling of 2D correlation energy functionals can be derived. For 3D correlation functionals, the correlation scales as,[102]

$$E_c[\rho_\lambda] < \lambda E_c[\rho] \quad (\lambda < 1), \tag{2.64}$$

$$E_c[\rho_\lambda] > \lambda E_c[\rho] \quad (\lambda > 1), \tag{2.65}$$

with $\rho(R_x, R_y, R_z) \rightarrow \rho_\lambda = \lambda^3 \rho(\lambda R_x, \lambda R_y, \lambda R_z)$. The 2D correlation energy functional also obey same conditions Eq.(2.64), and Eq.(2.65) with scaled density $\rho_\lambda = \lambda^2 \rho(\lambda R_x, \lambda R_y)$. Under uniform scaling of coordinates, K_σ of 2D-B88 functional Eq.(2.50) is dimensionless. So, using the scaled density and scaled β' ($\beta'[\rho_\lambda] = \lambda \beta'[\rho]$) in Eq.(2.62), it can be observed that the functionals E_c^{GCS} and E_c^{LCS} satisfy these two conditions.

(c) In the high-density limit ($\lambda \rightarrow \infty$), and under uniform coordinate scaling, 3D-correlation functionals scale to a constant[103]

$$\lim_{\lambda \to \infty} E_c[\rho_\lambda] = const. \tag{2.66}$$

Following the same procedure as,[103] it is seen that in the high-density limit, the exact 2D correlation energy functional scales to a constant value. The correlation energy functionals E_c^{GCS} and E_c^{LCS} satisfy this condition (c).

(d) Similar to above condition (c), in the low-density limit ($\lambda \rightarrow 0$) the 2D-correlation energy follows

$$\lim_{\lambda \to 0} \frac{1}{\lambda} E_c[\rho_\lambda] = const. \tag{2.67}$$

This condition is also satisfied by both the correlation functionals, as K_σ of 2D-B88 functional is dimensionless.

(e) Now, taking non-uniform scaling of coordinates, within the high-density limit ($\lambda \rightarrow$

∞), the exact 3D-correlation energy functional should scale as[104]

$$\lim_{\lambda \to \infty} \lambda E_c[\rho_\lambda^x] = const.$$ (2.68)

For two-dimensions, the condition is the same, i.e., for non-uniform scaled density $\rho_\lambda^x = \lambda \rho(\lambda R_x, R_y)$, the correlation energy approaches to a constant value under high-density limit, similar to Eq.(2.68). Both the proposed correlation functionals do not satisfy this condition. Due to the presence of λ in the numerator of scaled correlation energy, the left-hand side of Eq.(2.68) goes to $-\infty$ instead of a constant.

(f) Similar to (e), within low-density limit and nonuniform scaling the correlation energy follows,

$$\lim_{\lambda \to 0} \frac{1}{\lambda} E_c[\rho_\lambda^x] = 0.$$ (2.69)

Both E_c^{GCS} and E_c^{LCS} functionals do not satisfy this condition.

The proposed correlation energy functionals E_c^{GCS} and a local version of it, E_c^{LCS} satisfy four important conditions that the exact 2D-correlation functional satisfies. But both the functionals do not satisfy the limiting conditions at high and low-density under non-uniform scaling of coordinates. Though they fail in these limiting cases, the correlation energy for the discussed parabolic systems are satisfactory.

2.5   Concluding remarks

In our attempts to construct new exchange-correlation energy functionals for two-dimensional quantum systems, we successfully derived exchange energy functionals based on density matrix expansion, and the correlation energy functionals are derived based on both DME and the Colle-Salvetti method. The proposed parameter-free simple exchange energy functional is proved to be very accurate for quantum dots with confined electrons more than two. Also, the parameterized exchange energy functionals derived by using the reduced density gradient and the kinetic energy densities are accurate for all forms of parabolic QDs. These exchange energy functionals accompanied by similar type of

correlation energy functional with parameterized form. Finally, we derived a correlation energy functional using the Colle-Salvetti type many-body wave function very useful for 2D-systems, and it becomes more accurate with the parameter-free exchange energy functional.

Chapter 3

Laplacian free and asymptotic corrected semilocal exchange potential applied to the band gap of solids

Prediction of reliable, and more accurate band gaps of narrow band gap semiconductors to large band gap insulators is very necessary within the semilocal method of DFT. Before proceeding, a short discussion on fractional particle numbers and the derivative discontinuity is necessary. This is required to understand, why the KS method tends to underestimate the bandgaps? Let's consider the trial KS density $\rho(\mathbf{r})$ integrates to number of electrons $N = M + \eta$, with $M > 0$, and $0 < \eta < 1$.[105] Such fractional electron number may arise from the density variation in the open systems. To get the minimum energy for such system, one needs to take superposition of two pure states Ψ_M and Ψ_{M+1} corresponding to electron numbers M and $M+1$ with probabilities of $1 - \eta$, and η. Such choice leads to $(1 - \eta)M + \eta(M+1) = M + \eta$ and the density is given by, $\rho(\mathbf{r}) = (1 - \eta)\langle\Psi_N|\hat{\rho}(\mathbf{r})|\Psi_N\rangle + \eta\langle\Psi_{N+1}|\hat{\rho}(\mathbf{r})|\Psi_{N+1}\rangle$. The use of above constrained density in the variational method to minimize the total energy guarantees the electron number $N + \eta$ and the minimum average energy is given by

$$E_{M+\eta} = (1 - \eta)E_M + \eta E_{M+1}. \tag{3.1}$$

It implies the variation of E with N is a continuous line segments joining integer electron numbers. But discontinuity at integer electron numbers are observed, i.e., $\mu = \delta E / \delta N$ is discontinuous at integer N. And the slope on the positive and negative side of E(N) is equal to electron affinity (EA) and ionization potential(IP). For an atom having integral nuclear charge Z, the chemical potential follows,

$$\mu = \begin{cases} -I, & (Z-1 < N < Z) \\ -A, & (Z < N < Z+1) \end{cases}$$

Where, the IP $I = -(E_Z - E_{Z-1})$ and the EA $A = -(E_{Z+1} - E_Z)$. Or for an N-electron system $I(N) = E(N-1) - E(N)$ and $A(N) = E(N) - E(N+1)$. In the KS system the fundamental gap is given by $E_g = I(N) - A(N)$ and the center of fundamental band is given by $-[I(N) - A(N)]/2$. The infinitesimal change in the charge density due to addition or removal of infinitesimal electron number may be thought as it is arising from the potential. Such infinitesimal change in the potential will not change the one-electron energy and with help of Janak's theorem, we can write, the IP of the KS system is same as the negative of highest occupied electron energy, i.e., $I(N) = -\varepsilon_N(N)$, and the EA is $A(N) = -\varepsilon_{N+1}(N)$, where ε_{N+1} is the energy of lowest unoccupied state.[106] But, in strict sense, an infinitesimal change through an integer electron number will see a constant jump Δ in the potential[106]

$$\delta\rho(\mathbf{r}) \leftrightarrow \delta v_{eff}(\mathbf{r}) + \Delta \tag{3.2}$$

The derivative discontinuity Δ in the XC energy arising at integer electron number give as,

$$\Delta_{xc} = \left.\frac{\delta E_{xc}[\rho]}{\delta\rho(\mathbf{r})}\right|_{+} - \left.\frac{\delta E_{xc}[\rho]}{\delta\rho(\mathbf{r})}\right|_{-} \tag{3.3}$$

The positive and negative signs means functional derivatives need to be calculated from above and below the integer particle number, respectively. The fundamental gap of the KS system underestimates the band width equal to the derivative discontinuity Δ_{xc}.[105,107] However, the KS formalism able to predict the correct band center. So, for getting the gap close to the experimental values, the approximated exchange-correlation functional

must include Δ_{xc}. To take care one of such important constraints, few other methods being proposed such as the exact-exchange (EXX) formalism that by construction includes Δ_{xc}.[108,109,110] Also, the hybrid methods are very accurate in this direction, but the expensive calculation make them ineffective in case of large crystal structures. In this regard, the meta-GGAs methods are very appealing and have acceptable accuracy. Several meta-GGA functionals[30,34,42] with the ability of producing admissible band gaps have been developed in recent past. Though these functionals are sufficient to describe the ground state properties, they unable to describe the excited property such as the band structure up to expectation. The underlying cases being given to the inherent "delocalization error"[111,112] and the absence of (Δ_{xc}).[105,106] These two important constraints are included within the hybrid functionals,[113,114] but it is much more expensive than the meta-GGA methods. However, later it is observed that the meta-GGA functionals within the generalized Kohn-Sham scheme posses some amount of Δ_{xc}.[115,116] Other than the hybrid methods, there are several methods such as self interaction correction (SIC),[117,118,119] on-site potential correction with density functional formalism (DFT + U),[120] DFT based dynamic mean field theory (DFT+DMFT), and and quasi particle self energy corrections (GW)[121,122,123,124,125,126] are also proposed. But, except DFT+U, other methods are computationally expensive and DFT+U is only for the localized electronic systems with $3d$ or $4f$ electrons.

To get rid of such problems, exchange only potentials suitable for both the problems have been proposed and successfully applied to crystals.[127,128,129,130,131,132,133,134] In attempt to incorporate such effects simple GGA type exchange potentials proposed by Leeuwen and Baerends (LB),[135] Gritsenko et al. (GLLB)[136] meta-GGA type exchange only potential proposed by Becke and Johnson (BJ) potential.[127] In BJ potential, to get the step structure of the exact potential, KS kinetic energy dependent term is added to the Slater potential. To make a semilocal form of the BJ potential, the Slater potential is replaced by asymptotically correct Becke-Roussel (BR)[137] semilocal potential. In this work, we attempt to modify the BR potential through its under lying exchange hole, and use the modified potential for band gap calculations. First, we replace the Laplacian of density present in the exchange hole with the help of KS kinetic energy density. It is

necessary to avoid the divergence of exchange hole near the nucleus, as the finite exchange hole is always needed everywhere through out the system.[42,138] By avoiding the Laplacian, the form of the potential will be very simple, and such strategies are usually encountered in the construction of meta-GGA functionals. Also, in avoiding Laplacian, we avoid numerical problems arising from the higher order derivatives of density.[139,140] *Secondly*, We use the generalized coordinate transformation[42] to make the exchange hole more localized[72] and more precise. *Finally*, similar to first chapter, we modify the Fermi momentum to include in-homogeneity of the system without obstructing the uniform limit of exchange hole.

Integrating all these ideas, we propose a modified version of BR potential (mBR) by employing the Laplacian free, generalized exchange hole. Within the frame of Tran and Blaha[129] exchange potential, the mBR is utilized in the band gap calculation of a wide range of materials. This test set includes various oxides, transition metal dichalcogenides, crystals of oligoacenes. For comparison purpose, we compare the proposed potential with previously developed potentials along with available references. Besides these materials, we analyze the performance on the band gap opening of silicon doped graphene and in monolayer of hexagonal boron nitride.

3.1   Theoretical Background

Representing the exchange energy functional in terms of spherical averaged exchange hole $\langle \rho_{x\sigma}(\mathbf{r}, \mathbf{r}+\mathbf{u}) \rangle$ surrounding electron density $\rho_\sigma(\mathbf{r})$, similar to Eq.(2.1), and Eq.(2.22),

$$E_x = -\frac{1}{2} \sum_\sigma \int \int \frac{\rho_\sigma(\mathbf{r}) \langle \rho_{x\sigma}(\mathbf{r}, \mathbf{r}+\mathbf{u}) \rangle}{u} \, d\mathbf{r} d\mathbf{u}. \qquad (3.4)$$

The exchange hole present in the above Eq.(3.4) depends on the electronic separation ($\mathbf{u}$) along with its orientation. Similar to Eq.(2.2), and Eq.(2.3), writing the spherically averaged exchange holein terms of 1st order spherically averaged reduced density matrix as,

$$\langle \rho_{x\sigma}(\mathbf{r}, \mathbf{r}+\mathbf{u}) \rangle = -\frac{\langle |\Gamma_{1\sigma}(\mathbf{r}, \mathbf{r}+\mathbf{u})|^2 \rangle}{\rho_\sigma(\mathbf{r})} \quad . \qquad (3.5)$$

The spherically averaged reduced density matrix is formed from the usual reduced density matrix via

$$\langle |\Gamma_{1\sigma}(\mathbf{r},\mathbf{r}+\mathbf{u})| \rangle = \frac{1}{4\pi} \int \Gamma_{1\sigma}(\mathbf{r},\mathbf{r}+\mathbf{u}) \, d\Omega_u , \tag{3.6}$$

and the reduced density matrix is written by the KS orbitals $\psi_{i\sigma}$ as

$$\Gamma_{1\sigma}(\mathbf{r},\mathbf{r}+\mathbf{u}) = \sum_{i}^{occ} \psi_{i\sigma}^{*}(\mathbf{r}) \psi_{i\sigma}(\mathbf{r}+\mathbf{u}) . \tag{3.7}$$

Now using the exchange potential that can be generated from the spherically averaged exchange hole, the exchange energy form of Eq.(3.4) expressed as,

$$E_x = \frac{1}{2} \sum_{\sigma} \int \rho_\sigma(\mathbf{r}) U_{x\sigma}(\mathbf{r}) d\mathbf{r} . \tag{3.8}$$

Where, $U_{x\sigma}(\mathbf{r})$ is the exchange potential generated from the exchange hole and

$$U_{x\sigma}(\mathbf{r}) = - \int \frac{\langle \rho_{x\sigma}(\mathbf{r},\mathbf{r}+\mathbf{u}) \rangle}{u} \, d\mathbf{u} . \tag{3.9}$$

As can be seen, the exchange hole is an important entity, from which we can make the exchange potential, and hence the exchange energy. One important point needs to be added here that, the above-mentioned exchange potential is not the functional derivative of any exchange energy.

In this regard, a form of exchange potential is proposed by Becke and Roussel,[137] which is defined as

$$U_{x\sigma} = -(1 - e^{-x} - \frac{1}{2}xe^{-x})/b, \tag{3.10}$$

where $b = (x^3 e^{-x}/(8\pi\rho_\sigma))^{1/3}$, and the value of x is the solution of a nonlinear one-dimensional equation,

$$\frac{xe^{-2x/3}}{x-2} = \frac{2\pi^{2/3}\rho_\sigma^{5/3}}{3Q_\sigma^{BR}} . \tag{3.11}$$

Here,

$$Q_\sigma^{BR} = \frac{1}{6}(\nabla^2\rho_\sigma - 2\gamma D_\sigma^{BR}) \tag{3.12}$$

with $D_\sigma^{BR} = \tau_\sigma - (\nabla\rho_\sigma)^2/4\rho_\sigma$ and $\gamma = 0.8$. The form of Q_σ^{BR} is obtained from the second order term of in the Taylor series expansion of the spherical averaged exchange hole near the reference,

$$\langle\rho_{x\sigma}(\mathbf{r},\mathbf{u})\rangle = \rho_\sigma(\mathbf{r}) + \frac{u^2}{6}\left[\nabla^2\rho_\sigma(\mathbf{r}) - 2\gamma D_\sigma^{BR}\right], \tag{3.13}$$

In the following section, we discuss the proposed modifications over BR potential.

3.1.1 Semilocal View of Slater Potential: a generalized coordinate transformation based approach

In the previous chapter, we have localized the 2D-exchange hole through the generalized coordinate transformation, and this idea is also encountered in 3D functional construction.[72,141] The benefits from such transformation can be interpreted as follows, (i) depending on the coordinate transformation parameter, different exchange hole, hence the exchange potential can be constructed,[142] (ii) it well respects the uniform density limit, and only affects higher order non-uniform terms, (iii) the on-top value of exchange hole remains unaltered.[72] In this process, one of the important properties, i.e., the normalization constraint is lost.[72] However, this constraint can be imposed following the re-summation technique of Jianmin et. el..[42] Also, following the BR model, we consider the small '$u-$' behavior of the exchange potential, so that the asymptotic behavior can be retained.

Let's start with the generalized coordinate transformation of 1st order reduced density matrix as discussed in Eq.(2.23),

$$\Gamma_{1\sigma}^t(\mathbf{r},\mathbf{r}+\mathbf{u}) = \sum_i^{occ} \psi_{i\sigma}^*(\mathbf{r}+(\lambda-1)\mathbf{u})\psi_{i\sigma}(\mathbf{r}+\lambda\mathbf{u}), \tag{3.14}$$

and the corresponding spherically averaged exchange hole is written as

$$\langle\rho_{x\sigma}^t(\mathbf{r},\mathbf{r}+\mathbf{u})\rangle = -\frac{\langle|\Gamma_{1\sigma}^t(\mathbf{r},\mathbf{r}+\mathbf{u})|^2\rangle}{\rho_\sigma(\mathbf{r})}, \tag{3.15}$$

Based on the coordinate-transformation parameter λ, the localization of exchange hole is

handled. Now, this transformed hole can be used to obtain the transformed potential,

$$U_{x\sigma}^t(\mathbf{r}) = - \int \frac{\langle \rho_{x\sigma}^t(\mathbf{r}, \mathbf{r} + \mathbf{u}) \rangle}{u} \, d\mathbf{u} \qquad (3.16)$$

and the exchange energy

$$E_x^t = \frac{1}{2} \sum_\sigma \int \rho_\sigma(\mathbf{r}) U_{x\sigma}^t(\mathbf{r}) d\mathbf{r}. \qquad (3.17)$$

To get the improved version of BR potential, we start with the transformed exchange hole developed from the density matrix expansion (DME).[42] Use of such exchange hole has advantages, (i) controlled localization of hole, (ii) inclusion of inhomogeneity without disturbing the uniform density limit, and (iii) avoiding the Laplacian of density through well known substitution. Incorporating all these rectifications, the small $\mathbf{u}$ expansion of the exchange hole written as,

$$\langle \rho_{x\sigma}^t(\mathbf{r}, \mathbf{u}) \rangle = \rho_\sigma(\mathbf{r}) + \frac{u^2}{6} \Big[2(\lambda^2 - \lambda + \frac{1}{2}) \nabla^2 \rho_\sigma(\mathbf{r}) - 4\tau_\sigma + \frac{6}{5} k_\sigma^2 \rho_\sigma(\mathbf{r})(f_\sigma^2 - 1)$$
$$+ \frac{1}{2}(2\lambda - 1)^2 \frac{(\vec{\nabla}\rho_\sigma(\mathbf{r}))^2}{\rho_\sigma(\mathbf{r})} \Big], \qquad (3.18)$$

with,

$$f_\sigma = \Big[1 + 10(\frac{70}{27}) \frac{1}{4(6\pi^2)^{\frac{2}{3}}} (2\lambda - 1)^2 x_\sigma^2 + \frac{\beta}{16(6\pi^2)^{\frac{4}{3}}} (2\lambda - 1)^4 x_\sigma^4 \Big]^{\frac{1}{10}}. \qquad (3.19)$$

The reduced density gradient $x_\sigma = |\nabla\rho_\sigma|/\rho_\sigma^{\frac{4}{3}}$. There is no unique form of f_σ, and is used to include the non-uniform effect via the momentum was fixed by using the normalization condition of the exchange hole.[42] Any quantity obeying a particular constraint that reduced to unity in the homogeneous limit can be an observable option. The used parameters λ, and β will be determined later. With the limiting conditions $f_\sigma \approx 1$, and $\lambda = 1$ that defines the slowly varying density, and conventional exchange hole, above transformed exchange hole 3.18 reduces to BR exchange hole 3.13. Also, the uniform limit exchange hole is well respected. The proposed modifications on the exchange hole makes it more flexible, and more accurate, as it able to recover correct small -u behavior, uniform density

limit, and adjustable shape.

Now, we collect the modified Q_σ from the second order term of the transformed exchange hole,

$$Q_\sigma^{mBR} = \frac{1}{6}\left[2(\lambda^2 - \lambda + \frac{1}{2})\nabla^2\rho_\sigma(\mathbf{r}) + \frac{6}{5}k_\sigma^2\rho_\sigma(\mathbf{r})(f_\sigma^2 - 1) - 2\gamma D_\sigma^{mBR}\right], \tag{3.20}$$

where $D_\sigma^{mBR} = 2\tau_\sigma - \frac{1}{4}(2\lambda - 1)^2\frac{(\vec{\nabla}\rho_\sigma(\mathbf{r}))^2}{\rho_\sigma(\mathbf{r})}$, and parameter γ will be fixed later. As discussed before, to avoid the divergence of exchange hole near nucleus, and to avoid the complexity arising in the inclusion of divergence, we take the help of the density dependent kinetic energy density,[42,137] and replace the Laplacian as,

$$\nabla^2\rho_\sigma(\mathbf{r}) \approx 3[2\tau_\sigma - \tau_\sigma^{unif} - \frac{1}{36}\frac{(\vec{\nabla}\rho_\sigma(\mathbf{r}))^2}{\rho_\sigma(\mathbf{r})}]. \tag{3.21}$$

With these rectifications, the present model of Q_σ^{mBR} attains the form as,

$$Q_\sigma^{mBR} = \frac{1}{6}\left[6(\lambda^2 - \lambda + \frac{1}{2})\left(2\tau_\sigma - \tau_\sigma^{unif} - \frac{1}{36}\frac{(\vec{\nabla}\rho_\sigma(\mathbf{r}))^2}{\rho_\sigma(\mathbf{r})}\right) + \frac{6}{5}k_\sigma^2\rho_\sigma(\mathbf{r})(f_\sigma^2 - 1) - 2\gamma D_\sigma^{mBR}\right]. \tag{3.22}$$

Similar to BR,[137] using the general exchange hole model as analytically derived from the hydrogen orbital, the above derived Q_σ^{mBR} can be used in the non-linear one-dimensional equation(3.11),

$$\frac{y\exp(-2y/3)}{y-2} = \frac{2}{3}\pi^{2/3}\frac{\rho_\sigma^{5/3}}{Q_\sigma^{mBR}}. \tag{3.23}$$

For a given density, its gradient, and the kinetic energy density, the value of y can be found numerically. And at any reference point the coordinate-transformed exchange potential becomes,

$$U_{x\sigma}^t(\mathbf{r}) = -(1 - e^{-y} - \frac{1}{2}ye^{-y})/b_t \tag{3.24}$$

with

$$b_t^3 = \frac{y^3 e^{-y}}{8\pi\rho_\sigma}. \tag{3.25}$$

Finally, the proposed transformed exchange hole has asymptotically decaying potential,

Table 3.1: The exchange energies (in a.u.) of noble-gas atoms are shown. The MAE as obtained taking HF as the references are given in the last row.

Atoms	HF	LDA	BR $\gamma = 1.0$	BR $\gamma = 0.8$	mBR $\gamma = 1.0$ $\lambda = 0.877$ $\beta = 20.0$
He	-1.026	-0.884	-1.039	-1.039	-1.032
Ne	-12.11	-11.03	-12.19	-12.33	-12.23
Ar	-30.19	-27.86	-30.09	-30.55	-30.33
Kr	-93.89	-88.62	-92.88	-94.77	-93.97
Xe	-179.2	-170.6	-176.4	-180.3	-178.7
MAE(Δ)		3.48	1.20	0.51	**0.16**

and satisfy all other discussed constraints. Now, we need to assign appropriate values to the constants β, λ, and γ present in the potential.

3.1.2   Testing *m*BR on atoms

To fix the parameters present in the potential, we take help of exact potential of hydrogen and Helium atom. We fix $\gamma = 1$ similar to BR model. The parameter λ used to play with the shape of the exchange potential is fixed to 0.877, by matching the exact exchange energy of of hydrogen atom(i.e., 0.312 Hartree). The value of parameter β is fixed to 20.00 by comparing to exchange energy of He atom. With these constants, we calculate the exchange energies of noble gases from He to Xe, and the exchange energies are tabulated in Table 3.1. For comparison, we put the exchange energies of BR, Hartree-Fock, and LDA. For these calculations, we use numerical Hartree-Fock orbital of Clementi-Roetti.[143] The improved exchange energies of these noble gases by mBR over BR can be observed. As atomic number increases, the exchange energies of mBR becomes more close to the HF energies. We compare the exchange (hole) potential of Ne atom considering both BR, and mBR methods in Fig. 3.1. The exact exchange potential (optimized effective potential (OEP)) is also prsented in the same figure. The close resemblance between these two potentials will allow the replacement of BR with the Laplacian free mBR. The successful application of mBR potential on noble gas atoms encourages us to use the potential in calculation of band gap of solids
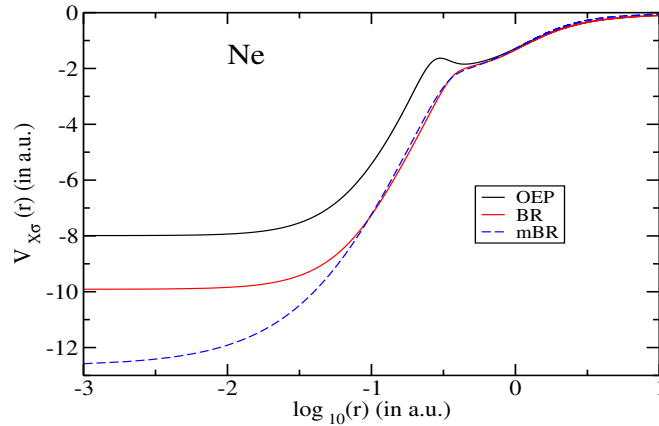
Figure 3.1: Exchange potentials of Ne atom using BR, and mBR methods. For BR the $\gamma = 0.8$ is used. The exact potential as obtained from the optimized effective potential (OEP) method is also shown.

3.2 Band Gaps using mBR

To apply asymptotically correct mBR potential to calculate band gaps of solids, we follow the framework of Becke and Johnson (BJ).[127] The exchange potential of BJ has a good resemblance with the atomic potential. A basic yet effective idea lies in the development of BJ potential. As the Slater potential fails to recover the atomic shell structure, the difference between the optimized effective potential (OEP) and the Slater potential, i.e., $\Delta v_{X\sigma} = v_{X\sigma}^{OEP} - v_{X\sigma}^{Slater}$ is added to the Slater potential. The form of $\Delta v_{X\sigma}$ is carefully chosen so that it depends on the fraction of kinetic energy density and the charge density. Also, the BJ potential is tested with the BR potential(Eq. 3.10) by replacing the Slater potential, and the form is written as,

$$v_{X,\sigma}^{BJ} = v_{X,\sigma}^{BR} + \frac{1}{\pi}\sqrt{\frac{5}{12}}\sqrt{\frac{2\tau_\sigma}{\rho_\sigma}}, \tag{3.26}$$

In combination of LDA exchange and correlation, Tran et al.,[128] used the form of BJ exchange potential in the self-consistent method to calculate the band gaps of non-magnetic semiconductors and insulators. This method improves the band gaps of these solids in comparison with conventional LDA, and GGA methods. The underestimation by PBE

functional is corrected up to 0.5-1 eV. Though BJ able to reduce the difference between the experimental and popularly used PBE functional, the underestimation still exists. Such scope allows Tran and Blaha[129] for more improvement. They proposed a modification usually known as TBMBJ potential, and is written as,

$$v_{X,\sigma}^{TBMBJ} = Cv_{X,\sigma}^{BR} + (3C-2)\frac{1}{\pi}\sqrt{\frac{5}{12}}\sqrt{\frac{2\tau_\sigma}{\rho_\sigma}}. \tag{3.27}$$

The parameter C present in the above potential Eq.(3.27) makes it different from Eq.(3.26). The form of this parameter is given by,

$$C = \mathscr{A} + \mathscr{B}\left(\frac{1}{V_{cell}}\int_{cell}\frac{|\nabla\rho(r')|}{\rho(r')}d^3r'\right)^{1/2}, \tag{3.28}$$

The parameter C depends on the structure of system or on the lattice parameter of the crystal through the volume of the unit cell V_{cell}. Other two parameters of TBMBJ model were fixed to be $\mathscr{A} = -0.012$ and $\mathscr{B} = 1.023$ bohr$^{1/2}$, and the strategy to fix these parameters was to compare the calculated band gap with the experimental band gap for a test set of solids. The TBMBJ model reduces to the BJ model potential when the parameter C is set to 1. It is shown that the use of lattice structure dependent parameter C in the TBMBJ potential increases the accuracy of band gaps in cases of noble gas solids with insulating band gaps, semiconductors, and transition metal oxides (Table I of Ref. [129]). Also other analysis[144] shows the improvement of TBMBJ in the band gap calculation. It is concluded that the variation of parameter C affects the band gap linearly,[129,144] i.e., the smaller values of C are good for narrow band gap solids, and larger C are better for large gaps solids. Also, different sets of constants $\mathscr{A}$, $\mathscr{B}$, and the exponent are suggested by fitting with larger testing set.[145]

Now, staying in the framework of TBMBJ, we use the mBR potential Eq.(3.24) in Eq.(3.27). By this we have the final form of the potential as,

$$v_{X,\sigma}^{mBR-TBMBJ} = \tilde{C}v_{X,\sigma}^{mBR} + (3\tilde{C}-2)\frac{1}{\pi}\sqrt{\frac{5}{12}}\sqrt{\frac{2\tau_\sigma}{\rho_\sigma}}. \tag{3.29}$$

The parameter $\tilde{C}$ is similar to C but with different values of used constants $\mathscr{A}$, and $\mathscr{B}$. The values of constants $\mathscr{A}$, and $\mathscr{B}$ are determined by comparing the band gaps of semiconductors with corresponding experimental references. With these constants the parameter $\tilde{C}$ is determined to be,

$$\tilde{C} = -0.030 + 1.0 \left(\frac{1}{V_{cell}} \int_{cell} \frac{|\nabla \rho(r')|}{\rho(r')} d^3 r' \right)^{1/2} \qquad (3.30)$$

Now, we apply the newly developed exchange-only potential to predict the band gap of a wide variety of solids and monolayer systems. Before doing all the calculations, we list the details of our calculation procedure.

3.3   Computational details and Results

Aiming to calculate the band gaps of solids, we use full-potential linearized augmented-plane-wave (FLAPW) method implemented within WIEN2K[146] code. The band gaps for PBE functional, and BJ, TBMBJ exchange potentials are calculated using WIEN2K code. And mBR-TBMBJ potential is implemented in the framework of TBMBJ in the WIEN2K code. In addition, to get more qualitative picture of the functionals, we calculate the band gaps of the discussed test sets with a more accurate method, i.e., hybrid functional given by Heyd-Scuseria-Ernzerhof (HSE).[55] For these calculations, we use projector-augmented-wave (PAW) method implemented within the Vienna *ab initio* simulation package (VASP).[147,148,149,150] For all the calculations, we use experimental lattice constants. For Brilloun zone interaction, we use 1000 k points for all the solids, 6 k points for the oligoacenes, and 100 k points for mono-layer calculations. All other requirements for WIEN2K calculations are taken to be default values provided with WIEN2K package. The hybrid methods are carried out by VASP because of computational efficiency of pseudopotential method. The hybrid methods need a part of Hartree-Fock exchange in addition to density dependent exchange, so calculation with all electron method WIEN2K is very expensive. Using these computational set up, we do calculation for different test sets having contemporary importance. The first test set comprise of narrow band gap semi-

conductors to wide band gap of noble gas solids. Then, we consider the solids having experimental band gaps within 5 eV.

3.3.1 Bandgaps of semiconducting and insulating solids

To demonstrate the performance of developed exchange potential, we first use a set of solids having narrow band gaps to large band insulators as discussed in Table 2 of Reference.[128] In Table 3.2, Fundamental band gaps of PBE functional are tabulated in second column. For all the exchange only potentials, we use LDA exchange energy and LDA correlation energies to do SCF calculations. The band gaps corresponding to these potentials are listed in next three consecutive columns. For comparison, we provide more accurate hybrid functional values, and the experimental values in the last two columns. In the last row, MAE of of all the methods corresponding to the experimental values are shown, and the least error is marked with bold font. Usually noble gas-solids possess high insulating band gaps, and PBE, BJ, HSE method seen to be underestimating up to large extent. However, results of two potentials TBMBJ and mBR-TBMBJ are very close to experimental gap, and mBR-TBMBJ overestimates the gap (maximum up to 3.11 eV for Neon and exact for Xenon). Also the a little overestimation in case of narrow band gap semiconductors by mBR-TBMBJ is observed. To deeply understand the performance through error, we do a box plot Fig. 3.2 for the absolute errors of all the methods. From the statistical plot, it is clear that the mBR-TBMBJ is better than all other methods in terms of least quartile points except TBMBJ as TBMBJ has the lower maximum error value.

3.3.2 Bandgaps of Oxides

Here, we calculate fundamental band gaps of fourteen oxides with different space groups and structures. This test set comprised of semiconducting oxides is not biased to any exchange-correlation functionals. The band gaps of the oxides as obtained from considered methods are tabulated in Table 3.3. All the columns are similar to Table 3.2, and the MAE of all these calculated methods are in the last row. In the Reference [151], the au-

Table 3.2: Fundamental band gaps in eV for PBE XC energy functional and BJ, TBMBJ, mBR-TBMBJ exchange potentials with LDA correlation are given in second to fifth columns. The hybrid HSE and experimental band gaps are given in the last two columns. The last row is for the MAE Δ.

Solids .	PBE	BJ[a]	TBMBJ	mBR-TBMBJ	HSE	Expt[a]
Ne	11.59	13.14	23.74	24.81	14.27	21.70
Ar	8.72	9.63	13.87	16.11	10.37	14.20
Kr	7.31	7.98	11.38	13.04	8.71	11.60
Xe	6.21	6.76	8.68	9.80	7.44	9.80
C	4.16	4.42	5.07	5.24	5.26	5.48
Si	0.58	0.84	1.16	1.36	1.17	1.17
Ge	0.06	0.18	0.82	0.96	0.82	0.74
LiF	9.18	10.17	13.01	13.71	11.46	14.20
LiCl	6.37	6.96	8.89	9.82	7.81	9.40
MgO	4.77	5.64	7.26	7.50	6.47	7.83
ScN	0.00	0.17	0.87	1.10	0.90	0.90
BN	4.47	4.98	5.82	6.08	5.76	6.25
MgS	3.56	4.11	6.22	7.02	4.66	4.78
SiC	1.36	1.84	2.25	2.37	2.23	2.40
ZnS	1.91	2.57	3.50	3.71	3.30	3.91
GaN	1.65	2.21	2.70	2.71	3.15	3.20
GaAs	0.51	0.75	1.61	1.72	1.40	1.52
CdS	1.13	1.51	2.61	2.94	2.14	2.42
AlN	3.34	4.87	4.97	5.10	4.55	6.28
Δ	2.67	2.05	**0.58**	0.71	1.37	−

a-Reference [128, 129]
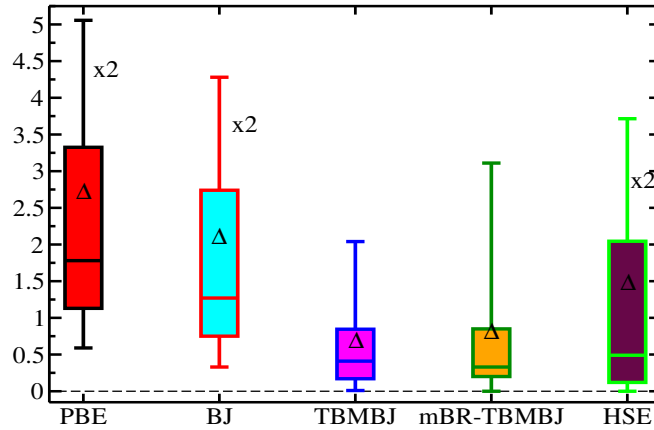
Figure 3.2: Shown are the box plots for absolute errors of band gaps. The solids present in Table 3.2 are considered for analysis of considered functionals. The whiskers start from the minimum of absolute error to the maximum of value absolute error. For clarity, we have scaled down the maximum errors of PBE, BJ, and HSE to their half values. The Δ present inside the boxes represent the MAE of corresponding methods. 25% of errors are below the lower end of the box known as quartile one (Q1). Similarly, the upper end known as quartile three (Q3), above which, we have 25% errors.

thors discussed the optoelectronic properties of oxides with general formula MCuOCh(M = Bi, La; Ch = S, Te) and the underestimation in the gap is shown considering the GGA(PBE) method. For the same oxides with the experimental lattice constant, we calculate energy gap using PBE-E_{xc}, all the exchange potentials, and hybrid HSE06 methods. For BiCuOS and BiCuOTe, PBE has underestimating gaps; BJ band gaps are close to the reference gap, and all the advance methods, i.e., TBMBJ, mBR-TBMBJ, HSE06 have slightly overestimating gaps. For LaCuOS and LaCuOTe, the gap increases from PBE to HSE. The solids having larger band gaps like $CuAlO_2$ and $BaSnO_3$ are noteworthy materials for optoelectronic applications, and materials like $LiCoO_2$ and $LiBiO_3$ having comparatively smaller band gaps are valuable for photovoltaic cell and battery applications. Similarly, $PbTiO_3$ and $BaTiO_3$ are very effective for memory and energy storage devices. In most of the cases, the band gaps of PBE are well smaller than the experimental gaps. Though BJ able to improve over PBE, it still falls short to the reference. The advance exchange potentials TBMBJ and mBR-TBMBJ are more accurate in the semilocal treatment of DFT and mBR-TBMBJ is more substantial method. In some of the cases, e.g., Ag_2PdO_2, $LiCoO_2$, $LiNbO_3$, HSE overestimates the gap. From the MAE

value shown in the last row of Table 3.3, mBR-TBMBJ and HSE are very close and good
have good agreement with the experiment.

Table 3.3: Fundamental band gaps (in eV) for a set of oxides are shown. The structure of
these oxides and their experimental band gaps are from the references listed below in this
table.

Oxides	PBE	BJ	TBMBJ	mBR-TBMBJ	HSE	EXPT.
BiCuOS	0.68	0.97	1.23	1.30	1.46	1.1^b
BiCuOTe	0.09	0.34	0.61	0.70	0.81	0.5^b
LaCuOS	1.85	1.94	2.18	2.35	3.00	3.1^b
LaCuOTe	1.35	1.42	1.65	1.83	2.25	2.4^b
Ag_2PdO_2	0.00	0.37	0.96	1.07	1.12	0.18^c
$CuAlO_2$	1.84	2.14	2.14	2.16	3.34	3.11^d
$LiCoO_2$	1.06	1.77	3.66	3.99	4.09	2.7^e
$BaSnO_3$	1.34	1.82	3.04	3.31	2.55	3.4^f
$NaBiO_3$	1.42	1.80	2.84	3.06	2.65	2.6^g
$LiBiO_3$	0.54	0.87	1.61	1.71	1.62	1.8^h
$LaMnO_3$	0.00	0.00	0.84	1.33	2.40^a	1.7^i
$PbTiO_3$	2.37	2.38	2.76	3.03	3.32	3.4^j
$BaTiO_3$	1.91	2.05	2.62	2.78	3.05	3.2^k
$LiNbO_3$	3.65	3.85	4.37	4.39	5.02	3.78^l
MAE (Δ)	1.05	0.83	0.57	0.51	**0.49**	—

a - Reference [152] b - Reference [151] c - Reference [153] d - Reference [154] e -
Reference [155] f - Reference [156] g - Reference [157] h - Reference [158] i -
Reference [159] j - Reference [160] k - Reference [161] l - Reference [162]

3.3.3 mBR-TBMBJ for Transition Metal Dichalcogenides

Transition metal dichalcogenides (TMDs) are good candidates for solar cell applications
due to their indirect semiconducting band gaps. Due to high temperature and high-
pressure stability, these layered materials are very convenient for photovoltaic and photo-
electrochemical solar cells. We take a test set containing nine TMDs and calculate their
semiconducting band gaps with the above mentioned exchange functionals and exchange
potentials. Similar to Table 3.3, we tabulated the band gaps of these TMDs in Table 3.4.

Table 3.4: Fundamental Band gaps (in eV) for a set of nine bulk TMDs are shown. All the columns are similar to Table 3.3.

TMDs	PBE	BJ	TBMBJ	mBR-TBMBJ	HSE	EXPT.
HfS_2	0.93	1.03	1.64	2.14	1.70	1.96-2.85[a]
$HfSe_2$	0.48	0.60	1.06	1.42	1.14	1.13[b]
MoS_2	0.88	0.94	1.12	1.23	1.46	1.23[c]
$MoSe_2$	0.83	0.89	1.02	1.13	1.33	1.09[c]
WS_2	0.99	1.05	1.23	1.40	1.56	1.35[c]
WSe_2	0.95	1.01	1.15	1.26	1.44	1.20[c]
ZrS_2	0.79	0.83	1.26	1.51	1.59	1.68-1.72[d]
$ZrSe_2$	0.32	0.39	0.70	0.89	1.00	1.20[e]
ZrSeS	0.65	0.70	1.08	1.29	1.30	1.44[e]
Δ	0.63	0.56	0.25	**0.11**	0.21	–

a- Reference [163, 164, 165] b- Reference [163] c- Reference [166] d- Reference [163, 167] e- Reference[167]

It is observed that the band gap values increase from PBE to HSE except HfS_2 and $HfSe_2$. In these two cases, the predicted band gap by HSE is smaller than that of mBR-TBMBJ, and the band gap of HfS_2 as determined by mBR-TBMBJ is more close to the experimental value. However, in most of the cases, PBE has large underestimated gaps, and HSE has little over estimated gaps. Because of the higher values of mBR-TBMBJ than TBMBJ, it acts like a bridge between TBMBJ and HSE. From Table 3.4, it is observed that in most of the cases, the band gaps obtained from mBR-TBMBJ are more close to reference values, as a result the MAE of this method is the least among all the considered methods. In Fig. 3.3, total density of states (DOS) of ZrS_2 is plotted for TBMBJ, mBR-TBMBJ, and HSE functionals. The band gap for all these methods can be observed from the difference between the valence band maximum(VBM), and the conduction band minimum(CBM). The valence density of states of this dia-magnetic n-type semiconductor is dominated by p-orbitals of Sulfur and the conduction DOS is dominated by d-orbitals of Zirconium. Also, all these methods can produce the peak of X-ray photoemission spectra ZrS_2[168] correctly.
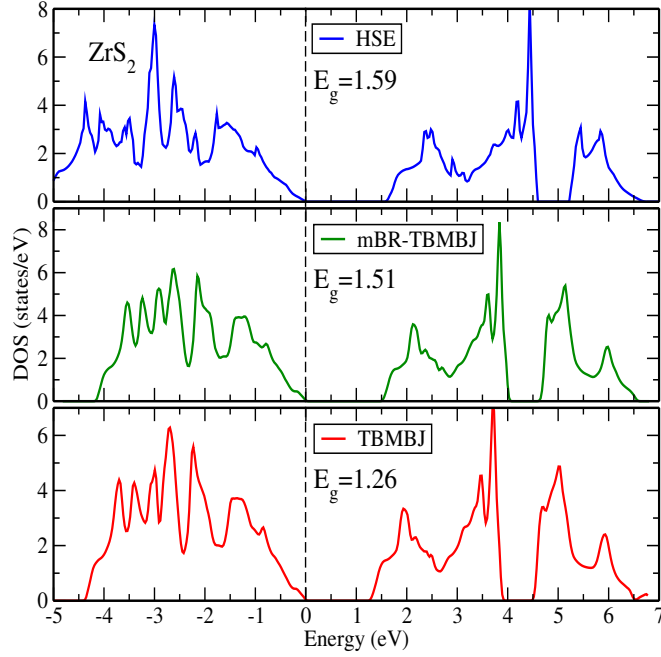
Figure 3.3: Total density of states for ZrS2 as obtained from TBMBJ, mBR-TBMBJ, and HSE functionals.

Table 3.5: Fundamental band gaps (in eV) for a set of TMOs are shown. The columns are similar to the previous table. In addition, PBE+U results of these TMOs are presented in the second last column. The last row contains the MAE and the least error is in bold font.

TMOs	PBE	BJ	TBMBJ	mBR-TBMBJ	HSE	PBE+U	EXPT.
CoO	0.00	0.48	2.93	3.03	3.41	3.62	3.6^a
FeO	0.00	0.34	1.80	1.99	2.20	2.05	2.4^b
MnO	0.86	1.13	3.02	3.14	2.80	2.39	3.9^b
NiO	0.95	1.64	4.13	3.98	4.42	3.26	$4.0, 4.3^b$
MAE(Δ)	3.02	2.57	0.56	**0.43**	0.47	0.65	–

a - Reference [169] b - Reference [129]

3.3.4 Band gaps of Transition Metal monoxides

In this subsection, we calculate the band gaps of four magnetic materials that are challenging for density functionals due to their insulating behavior. These transition metal mono-oxides (TMOs), i.e., CoO, Feo, MnO, and NiO known as Mott insulators are considered to study the performance of discussed methods. We adopt spin-polarized calculation of these anti-ferromagnets with appropriate magnetic ordering. It is known that the most used DFT method, i.e., GGA(PBE) predicts the Mott insulator as conductors. It can be followed from Table 3.5 that PBE unable to predict the insulating behavior CoO and FeO, and substantially underestimates the gaps of MnO and NiO. In addition, for these TMOs, we calculate the band gaps using PBE+U (PBE is used instead of the LDA) method in WIEN2K code with the value of parameter U same as Reference [120]. All these exchange energy potentials BJ, TBMBJ, mBR-TBMBJ able to give finite band gaps in all the cases, and band gap values follows BJ<TBMBJ<mBR-TBMBJ. Though HSE and PBE+U determine close gap values for some TMOs, mBR-TBMBJ has minimum MAE as it has better values in all the anti-ferromagnetic solids.

3.3.5 Band gaps of Oligoacenes

In a attempt to address the prediction of band gaps of organic molecular crystals, we calculate discuss the electronic properties of oligoacenes. These oligoacenes are are known for the application in field of organic optoelectronic. We follow the Reference [170] for crystal structure information and the structure for the calculation are collected from Cambridge Structural Database (CSD).[171] The band gap of these cata-condensed polycyclic aromatic hydrocarbons (PAH) depends on the size, i.e., with the addition of the CH rings, the gap decreases. All the exchange-correlation functionals and the exchange potentials able to follow the trend. Drastic underestimated band gap by PBE is observed, even the HSE has smaller values up to 1 eV than the experiment. From PBE to HSE, the gap values increase, and the MAE decrease gradually. The MAE of HSE is the minimum among all the cases.

Table 3.6: Band gaps (in eV) for four oligoacenes are shown. All the columns are identical to Table 3.3, and 3.4.

Oligoacenes	PBE	BJ	TBMBJ	mBR-TBMBJ	HSE	EXPT.
Napthalene(2A)	3.343	3.428	3.690	3.836	4.088	5.0^a
Anthracene(3A)	1.548	1.603	1.705	1.718	2.115	3.9^a
Tetracene(4A)	1.408	1.457	1.678	1.830	1.883	2.9^a
Pentacene(5A)	0.968	1.005	1.202	1.350	1.423	2.2^a
MAE (Δ)	1.68	1.62	1.43	1.31	**1.12**	–

a - Reference [170]
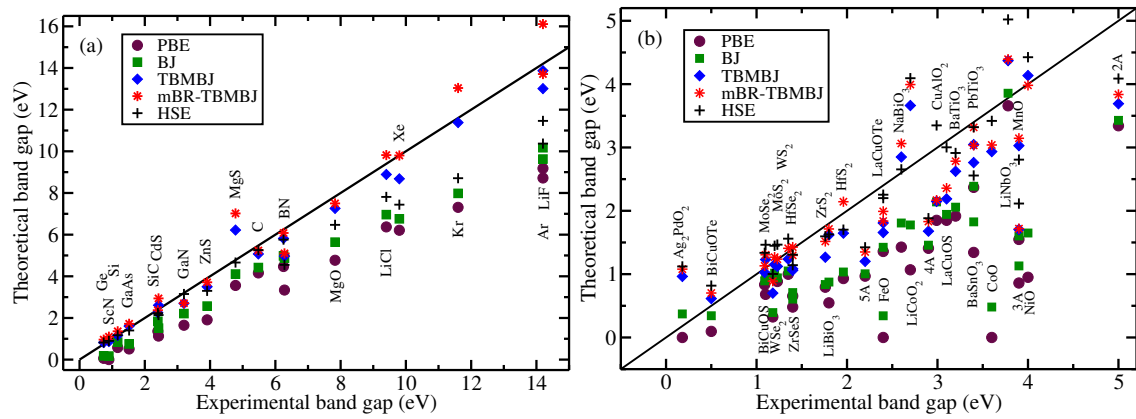
Figure 3.4: Theoretical band gap versus experimental band gap for solids (a) present in Tables 3.2 (b) present in Table 3.3 to 3.6.

3.4   Potentials on mono-layer: A case study

Electronic properties of bulk solids change in their two-dimensional structure. Prioritizing the band gaps of doped graphene and hexagonal boron nitride (hBN) sheets, we examine the performance of the discussed exchange potentials. Graphene, a mono-layer extracted from graphite is recognized for its generous properties. However, due to its it effective zero band gap, graphene is inefficient for semiconductor applications. For electronics applications, and to open semiconducting band gaps, iso-valent foreign atom doping is a trivial option. In recent articles,[172,173] authors discussed the optical and electronic prop-
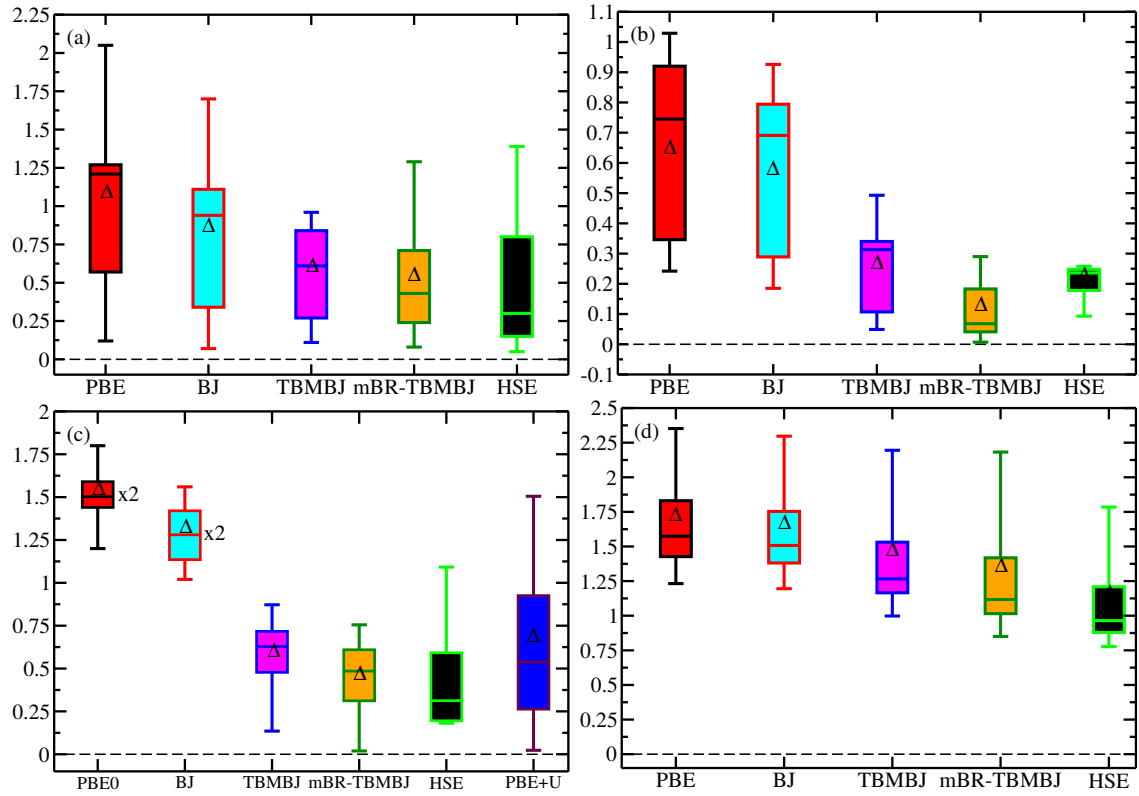
Figure 3.5: Box plots similar to Fig. 3.2 for (a) oxides present in Table 3.3, (b) TMDs present in Table 3.4, (c) TMOs present in Table 3.5, and (d) oligoacenes present in Table 3.6.

erties of silicon doped graphene with varying concentrations. It is seen that the band gap of such doped graphenes genuinely depend on the percentage of silicon. To address the band gap of such systems, we consider PBE energy functional, three exchange potentials, and HSE hybrid functional. To get appropriate stable structure, first, we relax the atomic positions of the structures with the TPSS[30] meta-GGA exchange-correlation functional in VASP using optimized lattice constants discussed in [173]. Then, we use this relaxed structure to calculate the band gaps for all the examined methods. To confine the electrons in the plane, we add vacuum layer above 20Å in all the cases. It is to be noted that TBMBJ and mBR-TBMBJ have lattice constant dependent parameter C. To get rid of the effect of vacuum in the parameter C, It is recommend to use an average $\nabla\rho/\rho$ from the bulk calculation of the same material.[146] So, we extract this factor from graphite and bulk boron nitride to be used in Si-doped graphene, and hBN sheet, respectively.

Table 3.7: Tabulated are the band gaps (in eV) of silicon doped graphenes having different doping percentage. The values for HSE and G_0W_0 are given in last two columns, and collected from Ref. [173]. The band gap of hBN using different potentials and energy functionals are shown in the lower panel of this table.

% of Si	PBE	BJ	TBMBJ	mBR-TBMBJ	HSE	G_0W_0
50	2.54	2.94	3.41	3.22	3.42	3.73
25	1.42	1.62	1.90	1.80	1.83	2.10
12.5	1.04	1.16	1.33	1.28	1.13	1.30
8.33	0.81	0.88	0.97	0.95	0.79	0.78
hBN	4.66	5.28	5.13	4.13	5.7	5.96^a

a - Experimental band gap from the Reference [174]

We tabulated the band gaps of those mono-layer structures considering PBE, BJ, TBMBJ, mBR-TBMBJ, HSE, and G_0W_0 in Table 3.7. In the lower panel of the same table, we show the band gaps for hBN. Comparing all the cases of Si-doped graphene, it is observed that the band gap decreases with the increase of doping percentage of silicon. The G_0W_0 method for 50% doped silicon opens the gap of 3.73 eV that is highest among all. For this percentage of Si, the band gap of TBMBJ and HSE are almost same. However, the behavior of mBR-TBMBJ potential is different from the bulk calculation. It is seen that, mBR-TBMBJ band gaps are larger than that of TBMBJ in all the bulk calculations, but this behavior reverses in layer calculations. For hBN, mBR-TBMBJ becomes inadequate even in comparison to PBE GGA functional, and BJ potential band gap is more close to HSE and G_0W_0. Such anomaly in case of layer calculation comes from the choice of parameter C. It is seen that in case of bulk , the band gap increases monotonically with parameter C, but this not the same in case of discussed layer calculations. We observe that the band gap for mono-layers attains a maximum value at a certain C, then the gap decreases. Also, different values of constants present within C, i.e., α, β, and the exponent used in article [145] will not improve the hBN band gap. Using the cell average of $|\nabla\rho|/\rho$ (second term in the right hand side of Eq. 3.28) from the bulk structure is admissible in case Si-doped graphene, but in case of hBN, it fails. So, it will be problematic to conclude the band gap of mono-layers from potentials constructed on
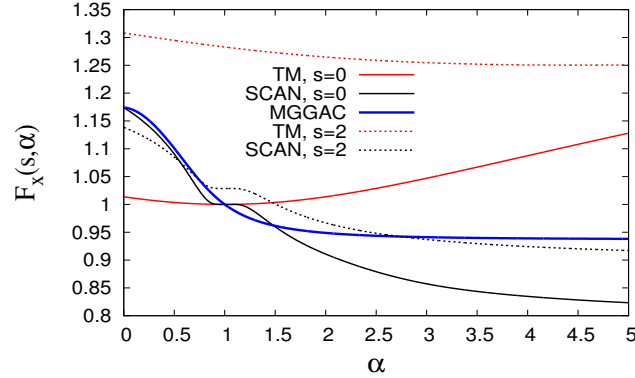
Figure 3.6: The variation of enhancement factors of different functionals with $\alpha = (\tau - \tau^W)/\tau^{unif}$.

TBMBJ exchange potential unless a particular model appropriate for 2D systems is developed in the TBMBJ framework. So, the question is which method within the semilocal DFT should be adopted for these systems? As the potentials can not be trusted, we have to depend on the exchange energy functionals. We examine recently-developed meta-GGA XC functionals TM, SCAN, and MGGAC[22] to calculate the band gaps of graphene based systems. The meta-GGA functionals include some amount of derivative discontinuity through the kinetic energy density and the amount of included Δ_{xc} is proportional to the slope of the negative slope of the enhancement factor with α.[175] So, In Fig. 3.6, we show the variation of $F_x(s, \alpha)$ with α for these functionals. For a fixed value of reduced gradient $s = 0$ and $s = 2$, both TM and SCAN have different curves, whereas due to no s dependency, MGGAC curve is fixed for all any value of s. The slopes of SCAN and MGGAC have more steep slope than TM, so we expect better band gaps for SCAN and MGGAC than TM.

In Tables 3.8 and 3.9, we present the band gaps of Si and Ge doped systems for different doping percentage. It is observed the accuracy of the MGGAC functional is at the same level of HSE hybrid method. The considered functionals can be organised according to the predicted band gaps of these systems and follows, PBE<TM<SCAN<MGGAC. The MGGAC functional only depends on the iso-orbital indicator α, this is an advantage of MGGAC functional over other semilocal functionals. And for 2D materials, the MG-

Table 3.8: Calculated band gaps (in eV) of Si doped graphene with different doping percentage similar to Table 3.7 are shown. The GW, GW_0,[173] and HSE[176] values are tabulated for comparison.

Doping %	GW	GW_0	HSE	PBE	SCAN	TM	MGGAC
50	4.10	3.88	3.42	2.57	2.85	2.68	3.44
25	2.51	2.27	1.83	1.29	1.53	1.37	1.84
12.5	1.69	1.46	1.13	0.76	0.92	0.81	1.12
8.33	1.11	0.92	0.79	0.53	0.64	0.56	0.77

Table 3.9: Band gaps (in eV) of Ge doped graphene for different semilocal methods along with the hybrid HSE functional are tabulated.

Doping %	HSE	PBE	SCAN	TM	MGGAC
50	2.79	2.06	2.25	2.20	2.83
25	1.50	0.92	1.11	0.92	1.43
12.5	1.00	0.67	0.78	0.72	0.97
8.33	0.72	0.49	0.57	0.51	0.69

GAC energy functional is an alternate and welcome option with the accuracy in the level of hybrid methods.

3.5   Concluding remarks

In this chapter, we propose a exchange-only potential appropriate for calculating band gaps of bulk solids having experimental band gaps from narrow band gap semiconductor to wide band gap insulators. For this our first step was to modify the Becke-Roussel potential by replacing the Laplacian of density with the expansion of Kohn-Sham kinetic energy density, modifying the exchange hole using the generalized coordinate transfer model, and introducing the non-homogeneity of the actual system through the Fermi wave vector. Due to the Laplacian free model of this potential, it can be implemented in any density functional code within generalized KS scheme. Though the generalized coordinate transformation allows a family of exchange hole, we picked one that is close to the hydrogenic exchange hole. Then the mBR potential is used in the framework of TBMBJ potential model to calculate the band gaps of a wide variety of sets containing solids of

present day interest. Starting from the narrow band gap semiconductors, insulators, oxides, transition metal dichalcogenides, transition metal mono-oxides, organic crystals to mono-layered structures, we examined the band gaps of developed mBR-TBMBJ potential. To compare the results, we tabulated the band gaps for PBE, BJ, TBMBJ, and hybrid HSE functionals. Analyzing the band gap of bulk solids, the underestimation by PBE functional for all the structures is concluded. Though the BJ potential improves over PBE, the predicted band gaps by it is still far from the experimental data. Other two potentials have the accuracy close to comparable costlier hybrid method, i.e. HSE06. In most of the cases , it is seen that mBR-TBMBJ acts like a bridge between the TBMBJ and HSE06 method, and the mean absolute error of it is more close to HSE06 functional. Moreover, the mBR-TBMBJ potential improves the band gaps of solids for which TBMBJ potential underestimates. By applying these exchange-only potentials to silicon-doped graphene and hexagonal Boron nitride, we observe the anomaly in using the parameter C. It is observed that for bulk calculation, the band gap increases monotonically with C, however, in case of mono-layered structures this condition is not followed even if C is extracted from the corresponding bulk structure. So it is concluded that due to the use of crystal structure dependent parameter C, it is not advised to use such advance potentials in the calculation of two-dimensional structures with the vacuum. Hence, our examined MG-GAC XC functional is an alternate method for 2D materials with accuracy level close to hybrid methods.

Chapter 4

Reverse Engineered Exchange holes and Long-range corrected screened hybrid-functionals

Though the GGA and meta-GGA XC functionals are quite successful, they face limitations in describing the excited state properties e.g. reaction barrier heights,[177] charge transfer,[178] Rydberg excitation,[179] and excitation energies[180,181] etc. These problems are attributed to the inherent many-electron self-interaction (MESI) error[182,183,184] and wrong prediction of energies at noninteger electron numbers by the semilocal density functional approximations(DFAs). The discontinuity arising at the integer electron number N is ignored by DFAs and DFAs predict very low energies at fractional N. Again, the HF method is also unable to produce the linear behavior of the energy at fractional particle numbers(Eq.(3.1)) and predicts average higher energies at N. These aforementioned problems are bypassed in hybrid approach. As mentioned in the introduction, the hybrid methods use some part of exact exchange or HF exchange in addition to the DFAs. The global hybrid functional having forms similar to Eq.(1.53) and Eq.(1.54) suffers from incorrect asymptotic potential and thus the range separated hybrids are adopted to obey such important constraints for molecules. The range-separation of Coulomb interaction Eq.(1.55) allows to employ the HF in the LR and the DFA in the SR. So, the LR- corrected hybrid

methods written as,

$$E_{XC}^{LC-hybrid} = E_X^{SR-DFA}(\omega) + E_X^{LR-HF}(\omega) + E_C^{DFA}, \qquad (4.1)$$

with screening parameter ω. With help of the error function and the complementary error function Eq.(1.55), the cut-off distance is selected. The LR-HF part of the exchange is obtained by multiplying the LR operator with Eq.(1.4) and given by,

$$E_X^{LR-HF} = -\frac{1}{2} \sum_{i,j=1}^{N} \sum_{\sigma} \int d^3r \int d^3r' \frac{\phi_i^*(\mathbf{r}\sigma)\phi_j^*(\mathbf{r}'\sigma) \, erf(\omega|\mathbf{r}-\mathbf{r}'|) \, \phi_j(\mathbf{r}\sigma)\phi_i(\mathbf{r}'\sigma)}{|\mathbf{r}-\mathbf{r}'|} \qquad (4.2)$$

The numerical implementation can be followed from the Ref. [185]. The correlation part is complete density functional. The remaining SR-DFA construction is our main motivation. The form of the SR-DFA is written as,

$$E_X^{SR-DFA}(\omega) = \frac{1}{2} \int d^3r \int d^3r' \frac{\rho(\mathbf{r}) \, (1 - erf(\omega|\mathbf{r}-\mathbf{r}'|)) \, \rho_x(\mathbf{r},\mathbf{r}')}{|\mathbf{r}-\mathbf{r}'|}. \qquad (4.3)$$

To get the SR-DFA, we need a form of the exchange hole $\rho_x(\mathbf{r},\mathbf{r}')$. Direct form of exchange hole can be derived from the density matrix using Eq.(3.5). But to get a GGA type exchange hole, we need to use the reverse engineered technique as there is no direct derivation to get the exchange hole. A positive side of this method is it satisfies constraints like on-top exact hole, uniform gas limit, energy sum rule, and normalization condition. the widely used LR corrected hybrid functional known as LC-ωPBE[186] was constructed by using the reverse engineered exchange hole of PBE[17] functional. The PBE exchange hole was modeled by Ernzerhof and Perdew (EP) first used by LC-ωPBE. However, the EP model suffers more problems in analytic integration and in the differentiation with respect to the density to get the potential. Also, it violates the Lieb-Oxford bound and for large s the energy obtained from model hole deviates from the PBE exchange energy. So, we adopt the Henderson-Janesko-Scuseria (HJS)[187] model to get exchange holes of GGA type exchange energy functionals. The exchange hole is the charge distribution that

interacts with the electron and using the pair-distribution function, it is written as,

$$\rho(\mathbf{r})\rho_x(\mathbf{r},\mathbf{r}') = -\rho_1(\mathbf{r};\mathbf{r}')\rho_1(\mathbf{r}';\mathbf{r}), \tag{4.4}$$

where, the electron density is $\rho(\mathbf{r}) = \rho_1(\mathbf{r};\mathbf{r})$. Following Eq.(3.4) and Eq.(3.5) exchange energy can be calculated from the exchange hole. But for a given exchange energy, to get corresponding exchange hole, we will use all the known constraints that exchange hole should satisfy. So let's list all the constraints that can be used for construction,

1. Negativity: the exchange hole is negative, $\rho_x(\mathbf{r},\mathbf{r}') \leq 0$

2. On-top exchange hole: From Eq.(4.4),

$$\rho_x(\mathbf{r},\mathbf{r}) = -\rho(\mathbf{r})/2. \tag{4.5}$$

3. Normalization: the exchange hole density integrates to exact negative one,

$$\int d\mathbf{r}'\rho_x(\mathbf{r},\mathbf{r}') = -1. \tag{4.6}$$

4. Energy constraint: The exchange hole should reproduce energy same as the given functional,

$$\frac{1}{2}\int d\mathbf{r}\,d\mathbf{r}'\frac{\rho(\mathbf{r})\rho_x(\mathbf{r},\mathbf{r}')}{|\mathbf{r}-\mathbf{r}'|} = E_x. \tag{4.7}$$

In addition, another constraint from the curvature of LDA shape function $\tilde{J}$ will be used. The angle-averaged and system-averaged LDA exchange hole is related to the shape function as,

$$\rho_x(\mathbf{r},\mathbf{r}+\mathbf{u}) = \rho_x^{LDA}[\rho(\mathbf{r}),\mathbf{u}] = \rho(\mathbf{r})\tilde{J}^{LDA}(y). \tag{4.8}$$

Where $\mathbf{u} = \mathbf{r}' - \mathbf{r}$, $y = k_F u$ and $k_F = (3\pi^2\rho)^{1/3}$ is the Fermi wave vector. So, we need a form of the shape function $\tilde{J}$ to get the exchange hole. To avoid Friedel oscillations observed in the exchange hole of HEG, a smooth non-oscillating model for the shape

function was first proposed by Perdew and Wang (PW92)[188] as,

$$J^{PW92}(y) = -\frac{A}{y^2}\frac{1}{1+(4/9)Ay^2} + \left(\frac{A}{y^2}+B+Cy^2\right)e^{-Dy^2}. \tag{4.9}$$

Where $A = 0.59$, $B = -0.54354$, $C = 0.027678$, and $D = 0.18843$. Any form of J related with the exchange hole as Eq.(4.8) should respect the constraints that exchange hole satisfies. Now, we derive the constraints for J using the listed constraints for exchange holes.

1. Due to positive electron density, $\tilde{J}^{LDA}(y) \leq 0$ (following first constraint of exchange hole)

2. The second constraint Eq.(4.5) implies

$$\tilde{J}^{LDA}(0) = -\frac{1}{2} \tag{4.10}$$

3. Following Eq.(4.6), we can write

$$\int_0^\infty du\, 4\pi u^2 \rho(\mathbf{r})\tilde{J}^{LDA}(k_F u) = \frac{4}{3\pi}\int_0^\infty dy\, y^2 \tilde{J}^{LDA}(y) = -1. \tag{4.11}$$

4. From Eq.(4.7), using HEG exchange energy density, it can be written as,

$$2\pi \int_0^\infty du\, u\, \rho(\mathbf{r})\tilde{J}^{LDA}(k_F u) = -\frac{3k_F}{4\pi} \Rightarrow \frac{8}{9}\int_0^\infty dy\, y\tilde{J}^{LDA}(y) = -1 \tag{4.12}$$

5. For small inter-electronic distance the HEG shape function goes as,

$$\tilde{J}^{LDA}(y) \rightarrow -\frac{1}{2} + \frac{y^2}{10} + ...,$$

that leads to

$$\frac{d^2\tilde{J}^{LDA}(y)}{dy^2}\Big|_{y=0} = \frac{1}{5} \tag{4.13}$$

6. For large inter-electronic distance,

$$\tilde{J}^{LDA}(y) \rightarrow -\frac{9}{4y^4} - \frac{9cos(2y)}{4y^4} \tag{4.14}$$

These constraints for the shape function are used by PW to model a non-oscillatory model of shape function given in Eq.(4.9). But Eq.(4.9) is not smooth enough and contains an unwanted small shoulder at large u. To get rid of such this unnecessary part EP model was proposed by adding y^4 term as,

$$J^{EP}(y) = -\frac{\mathscr{A}}{y^2} \frac{1}{1+(4/9)\mathscr{A}y^2} + \left(\frac{\mathscr{A}}{y^2} + \mathscr{B} + \mathscr{C}y^2 + \mathscr{E}y^4\right) e^{-\mathscr{D}y^2}. \tag{4.15}$$

We have already noted the problems of EP model and addressing those problems, the HJS model for LDA shape function was proposed as,

$$J^{LDA}_{HJS}(y) = -\frac{9}{4y^4} \left(1 - e^{-\mathscr{A}y^2}\right) + \left(\frac{9\mathscr{A}}{4y^2} + \mathscr{B} + \mathscr{C}y^2 + \mathscr{E}y^4\right) e^{-\mathscr{D}y^2}. \tag{4.16}$$

The HJS model only differs from the EP model by the behavior of the shape function at large inter-electronic distance. Now, the task is to assign appropriate values to the constants present in Eq.(4.16). Imposing the on-top constraint Eq.(4.10), we get

$$\mathscr{B} = \frac{9}{4} \left(\mathscr{A}\mathscr{D} - \frac{\mathscr{A}^2}{2}\right) - \frac{1}{2}. \tag{4.17}$$

Next, imposing the shape function constant Eq.(4.13), the value of $\mathscr{C}$ in terms of $\mathscr{A}$, $\mathscr{B}$, and $\mathscr{D}$ is obtained as,

$$\mathscr{C} = \mathscr{B}\mathscr{D} + \frac{3\mathscr{A}^3}{8} - \frac{9\mathscr{A}\mathscr{D}^2}{8} + \frac{1}{10}. \tag{4.18}$$

Similarly, the parameter $\mathscr{E}$ is fixed from the normalization constraint Eq.(4.11),

$$\mathscr{E} = \frac{6}{5}\mathscr{A}^{1/2}\mathscr{D}^3(2\mathscr{D}^{1/2} - \mathscr{A}^{1/2}) - \frac{2}{5}\mathscr{C}\mathscr{D} - \frac{4}{15}\mathscr{B}\mathscr{D}^2 - \frac{4}{5}\sqrt{\pi}\mathscr{D}^{7/2}. \tag{4.19}$$

The parameters $\mathscr{B}$, $\mathscr{C}$, and $\mathscr{E}$ are represented in term of $\mathscr{A}$, and $\mathscr{D}$. By imposing energy constraint Eq.(4.12), the values of $\mathscr{A}$, and $\mathscr{D}$ are determined to be $\mathscr{A} = 0.75211$, and $\mathscr{D} = 0.609650$. These values leads to $\mathscr{B} = -0.106364$, $\mathscr{C} = -0.118649$, and $\mathscr{E} = -0.0477963$. Up to now, we have discussed the construction of LDA shape function. Next, using the LDA shape function, we will show the HJS model to construct GGA type shape function J_{HJS}^{GGA}. Introducing the gradient dependent functions in $J_{HJS}^{LDA}(y)$, an ansatz for the GGA is given as,

$$J_{HJS}^{GGA}(y,s) = \left[-\frac{9}{4y^4}\left(1 - e^{-\mathscr{A}y^2}\right) + \left(\frac{9\mathscr{A}}{4y^2} + \mathscr{B} + \mathscr{C}\mathscr{F}(s)y^2 + \mathscr{E}\mathscr{G}(s)y^4\right)e^{-\mathscr{D}y^2}\right]e^{-s^2\mathscr{H}(s)y^2}.$$

(4.20)

The function $\mathscr{F}(s)$ is determined imposing the small u behavior and given as,

$$\mathscr{F}(s) = 1 - \frac{s^2}{27\mathscr{C}(1 + s^2/4)} - \frac{s^2\mathscr{H}}{2\mathscr{C}}$$

(4.21)

Before derivation of other two s dependent functions, we write some useful expressions that will be used later. (i) $\zeta = s^2\mathscr{H}(s)$, (ii) $\eta = \mathscr{A} + \zeta$, and (iii) $\lambda = \mathscr{D} + \zeta$. For a particular form of $\mathscr{F}(s)$ and $\mathscr{H}(s)$, we impose the normalization constraint Eq.(4.11) to the GGA shape function,

$$\frac{4}{3\pi}\int_0^\infty dy\, y^2 \tilde{J}_{HJS}^{GGA}(y,s) = -1.$$

(4.22)

And solving the above Eq.(4.22) for $\mathscr{G}(s)$, we get

$$\frac{3}{\sqrt{\pi}}\left(\sqrt{\zeta} - \sqrt{\eta}\right) + \frac{5\mathscr{E}\mathscr{G}(s)}{4\sqrt{\pi}\lambda^{7/2}} + \frac{\mathscr{C}\mathscr{F}(s)}{2\sqrt{\pi}\lambda^{5/2}} + \frac{\mathscr{B}}{3\sqrt{\pi}\lambda^{3/2}} + \frac{3\mathscr{A}}{2\sqrt{\pi}\lambda^{1/2}} = -1$$
$$\Rightarrow \mathscr{E}\mathscr{G}(s) = -\frac{2}{5}\mathscr{C}\mathscr{F}(s)\lambda - \frac{4}{15}\mathscr{B}\lambda^2 - \frac{6}{5}\mathscr{A}\lambda^3 - \frac{4}{5}\sqrt{\pi}\lambda^{7/2} - \frac{12}{5}\lambda^{7/2}\left(\sqrt{\zeta} - \sqrt{\eta}\right)$$

(4.23)

Finally to get the energy value of assigned energy functional, we use the energy integral Eq.(4.7) and Eq.(4.12),

$$
-\frac{8}{9}\int_0^\infty dy\, y\tilde{J}_{HJS}^{GGA}(y,s) = F_x^{GGA}(s)
$$

$$
Or\ \mathscr{A} - \frac{4\mathscr{B}}{9\lambda} - \frac{4\mathscr{C}\,\mathscr{F}(s)}{9\lambda^2} - \frac{8\mathscr{E}\,\mathscr{G}(s)}{9\lambda^3} + \zeta\ln\left(\frac{\zeta}{\lambda}\right) - \eta\ln\left(\frac{\eta}{\lambda}\right) = F_x^{GGA}(s) \tag{4.24}
$$

For any GGA type enhancement factor $F_x^{GGA}(s)$, we solve the Eq.(4.24) to get $\mathscr{H}(s)$, numerically. Putting derived forms of $\mathscr{F}(s)$ and $\mathscr{G}(s)$ in Eq.(4.24) on left side and using target s dependent enhancement factor, we solve for a numerical $\mathscr{H}(s)$. Then the numerical solution is fitted ta rational function,

$$
\mathscr{H}(s) = \left(\sum_{i=2}^{7} a_i s^i\right)/\left(1 + \sum_{i=1}^{9} b_i s^i\right). \tag{4.25}
$$

Having an appropriate shape function in our hand, we calculate the range-separated enhancement factor for SR region as,

$$
F_x^{SR-GGA}(s,\omega,k_F) = -\frac{8}{9}\int_0^\infty dy\, y\tilde{J}_{HJS}^{GGA}(y,s)\left(1 - erf\left(\frac{y}{k_F}\omega\right)\right). \tag{4.26}
$$

Or,

$$
\begin{aligned}
F_x^{SR-GGA}(s,\omega,k_F) = \mathscr{A} &- \frac{4\mathscr{B}}{9\lambda}(1-\chi) - \frac{4\mathscr{C}\,\mathscr{F}(s)}{9\lambda^2}\left(1 - \frac{3\chi}{2} + \frac{\chi^3}{2}\right) \\
&- \frac{8\mathscr{E}\,\mathscr{G}(s)}{9\lambda^3}\left(1 - \frac{15\chi}{8} + \frac{5\chi^3}{4} - \frac{3\chi^5}{8}\right) + 2v\left(\sqrt{\zeta+v^2} - \sqrt{\eta+v^2}\right) \\
&+ 2\zeta\ln\left(\frac{v+\sqrt{\zeta+v^2}}{v+\sqrt{\lambda+v^2}}\right) - 2\eta\ln\left(\frac{v+\sqrt{\eta+v^2}}{v+\sqrt{\lambda+v^2}}\right)
\end{aligned}
$$

$$\tag{4.27}$$

where $v = \omega/k_F$ and $\chi = v/\sqrt{\lambda+v^2}$. We use this HJS method to get exchange holes of three prototype exchange energy functionals.

4.0.1   Three prototype long-range corrected hybrid functionals

To construct LR corrected hybrid functionals, we take three prototype XC functionals that are developed based on PBE XC functional given in Eq.(1.37). The asymptotic PBE (APBE)[189] functional developed from the semiclassical atom theory, PBE functional for interfaces (PBEint)[190] developed by bridging the slowly and rapidly varying densities, and the semiclassical GGA at fourth order (SG4)[191] constructed by taking gradient expansion up to fourth order. These semilocal GGA functional are well known for their performances e.g. the APBE is accurate for atoms, molecules, and molecular complexes,[189,192,193] PBEint is satisfactory for hybrid interfaces and metal clusters,[190,194,195] and SG4 produces significantly well solid-state properties.[191,196,197]

APBE: Starting with the APBE GGA, the enhancement factor is given by,

$$F_x^{APBE} = 1 + \kappa - \kappa/[1 + \mu^{MGE2}s^2/\kappa], \qquad (4.28)$$

with $\mu^{MGE2} = 0.26$ and $\kappa = 0.804$. The value of κ is same as PBE and fixed from the Lieb-Oxford bound. But the value μ is different from PBE and fixed from modified second-order gradient expansion (MGE2).[189] Regarding the correlation energy functional, it is only different from the PBE with different value of $\beta = 3\mu^{MGE2}/\pi^2$ which is fixed from the local density linear response.

PBEint: The exchange enhancement factor of PBEint functional given by,

$$F_x^{PBEint} = 1 + \kappa - \kappa/[1 + \mu(s)s^2/\kappa] , \qquad (4.29)$$

where $\mu(s) = \mu^{GE2} + (\mu^{PBE} - \mu^{GE2})\frac{\alpha s^2}{1 + \alpha s^2}$ and $\alpha = 0.197$. The used $\mu(s)$ in PBEint act as an interpolation function such that for rapidly varying density $\mu \to \mu^{PBE}$ and for slowly varying density it goes to PBEsol, i.e., $\mu \to \mu^{PBEsol}$ As a result PBEint maintain good properties of both PBE and PBEsol XC functionals. Similar to APBE, PBEint correlation functional has the value for $\beta^{PBEint} = 0.052$.

SG4 : The exchange enhancement factor for the SG4[191] functional is written as,

$$F_x^{SG4} = 1 + \kappa_1 + \kappa_2 - \frac{\kappa_1\left(1 - \frac{\mu_1 s^2}{\kappa_1}\right)}{1 - \left(\frac{\mu_1 s^2}{\kappa_1}\right)^5} - \frac{\kappa_2}{1 + \frac{\mu_2 s^2}{\kappa_2}} \; . \tag{4.30}$$

It was constructed to recover the exact behavior of the modified gradient expansion of the exchange energy density up to fourth order. In addition, it keeps the Lieb-Oxford bound unchanged by imposing $\kappa_1 + \kappa_2 = 0.804$. To recover the second order expansion another condition $\mu_1 + \mu_2 = \mu^{MGE2} = 0.26$ was employed along with $\kappa_2 = -\mu_2^2/\nu^{MGE4}$. The parameters $\nu = -0.195$ is the fourth order coefficient and $\mu_1 = 0.042$ is fixed by fitting with the ionization potential in the semi classical neutral atom limit.

For the correlation energy density of the SG4 model is given by,

$$\varepsilon_c^{SG4} = \varepsilon_c^{LDA} + \phi^{\alpha t^3} H(r_s, \zeta, t). \tag{4.31}$$

The parameters $t = |\nabla \rho|/(2k_s \Phi \rho)$ known as reduced density gradient for correlation, $k_s = (4k_F/\pi)^{1/2}$ is known as Fermi screening wave vector, and Φ is the spin scaling factor. The value of $\alpha = 0.8$ was fixed by minimizing the entropy function. In the slowly varying limit ($t \to 0$), to recover LDA linear response, the relation $H \to \beta\Phi^3 t^2$ should be followed. For SG4 XC functional the form of β is given by

$$\beta = \beta_0 + \sigma t(1 - e^{-r_s^2}), \tag{4.32}$$

with $\beta_0 = 3\mu^{MGE2}/\pi^2$ and $\sigma = 0.07$. However, it is observed that α and σ are not flexible with the LC hybrid method. So, we only use APBE correlation functional which is the special case for SG4 correlation at $\beta = \beta_0 = 0.07903$, $\sigma = 0$, and $\alpha = 0$.

4.0.2 Range-separated hybrid using APBE, PBEint, and SG4

The range-separated hybrid functional using APBE, PBEint, and SG4 is only possible after constructing the exchange holes of corresponding functionals. So, employing the

Table 4.1: Fitted parameters to form $H(s)$ for the exchange holes of APBE, PBEint, and SG4 exchange functionals.

	APBE	PBEint	SG4
a_2	0.02273221	0.0047333	0.02273221
a_3	-0.06039976	-0.0101441	0.04855297
a_4	0.07814309	0.01072278	-0.12481836
a_5	-0.05481418	-0.00608029	0.09963666
a_6	0.01738706	0.00144668	-0.03066345
a_7	0.0008502	0.0000766	0.00432085
b_1	-2.91638499	-2.39737305	1.93055176
b_2	3.86022942	2.5499878	-5.47264766
b_3	-2.97137272	-1.54388838	5.37181798
b_4	1.52515139	0.59184499	-2.91240963
b_5	-0.57570311	-0.15548226	1.12772142
b_6	0.18417949	0.03286721	-0.31905254
b_7	-0.0462847	-0.00608099	0.10263425
b_8	0.01406773	0.00122022	-0.02540923
b_9	0.00066305	0.00005888	0.00343592

enhancement factors Eq.(4.28), Eq.(4.29), and Eq.(4.30) in the right side of Eq.(4.24), the s dependent function $H(s)$ is constructed numerically. In Table 4.1, we list all the fitted constants to form $H(s)$ (Eq.(4.25)) of APBE, PBEint, and SG4. To recover exact second order gradient expansion, we fix the parameter a_2, the coefficient of s^2 as,

$$a_2 = \frac{1}{6718464} \frac{(1215\mathscr{D}^2\mu_x - 4)^2}{\mathscr{D}^5}. \tag{4.33}$$

For PBEint $\mu_x = \mu^{GE2} = 10/81$ and for both APBE and SG4 $\mu_x = \mu^{MGE2} = 0.26$. By using this condition Eq.(4.33), we make sure the behavior of the functional well preserves in slowly varying density limit.

4.0.3   Correlation energy from local-density linear response

In constructing hybrid methods, it is a general practice to use the complete GGA correlation, i.e., without doing any changes in the form of the correlation energy functional. However, to get the XC energy functional that satisfies the local density linear response,

a small change is necessary in the correlation part. It is shown that LDA is a better approximation than the gradient expansion for small density variation around the uniform density.[198] So, for small density variation or at $s \to 0$, the coefficient of gradient dependent terms in both exchange and correlation energy functionals should cancel out each other. By imposing this constraint, we change the correlation energy parameters. Here, we show LC hybrid functionals with two choices of correlation energy functional. First one is the use of original APBE, PBEint, and SG4 correlation with corresponding SR-DFA exchange and another one is modifying the correlation energies that will satisfy the LDA linear response. The correlation energy functionals are developed by assigning the value of β present in the Eq. 7 of Ref. [17] as $\beta = 3\mu^{GE}/\pi^2$. Here, μ^{GE} is fixed from the gradient expansion form of the exchange at slowly varying density. In case of hybrid methods, as, we are using both DFA and HF in different ranges, we assign the correlation coefficient

$$\beta = 3(\mu_x^{\omega GGA,SR}(\nu) + \mu_x^{\omega LR-HF}(\nu))/\pi^2. \tag{4.34}$$

to satisfy the LDA linear response. The second order coefficient $\mu_x^{\omega GGA,SR}(\nu)$ is calculated by taking the Taylor expansion of Eq.(4.27) with respect to s and given by,

$$\mu_x^{\omega GGA,SR}(\nu) = \frac{4}{243}\left(\frac{1 - \frac{3}{2}\chi + \frac{1}{2}\chi^3}{\mathscr{D}^2}\right) - \frac{8}{9\mathscr{D}^3}\left(\frac{2}{135}\mathscr{D} - \frac{12}{5}\mathscr{D}^{7/2}a_2^{1/2}\right)\left(1 - \frac{15}{8}\chi + \frac{5}{4}\chi^3 - \frac{3}{8}\chi^5\right) \tag{4.35}$$

On the other hand, the LR-HF must recover the screened exchange gradient expansion derived in Ref. [199]. Then, we obtain

$$\mu_x^{\omega LR-HF}(\nu) = \frac{7}{81} - \frac{2\pi^2}{3}\int_0^\infty dz\, z\, a_x\, erfc(z\nu/2), \tag{4.36}$$

with

$$a_x = \frac{-72 + (72 - 36z^2 + z^4)\cos(z) - 2z(-36 + 5z^2)\sin(z)}{54\pi^2 z^4}. \tag{4.37}$$

In Fig.4.1, we plot β for the hybrids methods APBE, PBEint, and SG4. We mention that the APBE and SG4 functionals were constructed to recover the local density linear
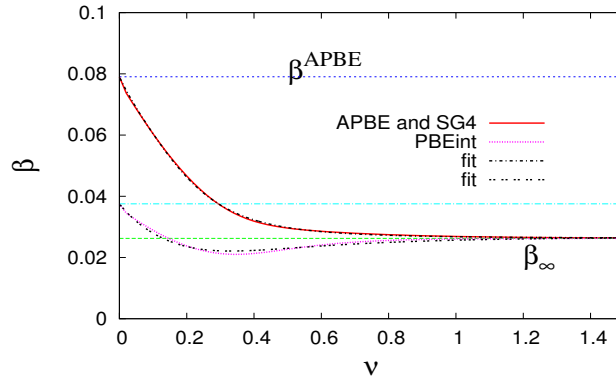
Figure 4.1: The correlation coefficient β of Eq.(4.34) plotted against the screened parameter $\nu = \omega/k_F$.

Table 4.2: Fitted parameters for β of APBE (SG4) and PBEint functional required in Eq.(4.38).

	APBE and SG4	PBEint
a_1	0.06929609	0.00000000
a_2	0.02090877	0.06413244
a_3	73.63025684	27.06803466
a_4	3.84513730	3.61233368
a_5	0.00000049	0.00005694
β_0	0.07903052	0.03750000
β_∞	0.02626845	0.02626845

response with $\beta^{APBE} = \beta_0^{SG4} \approx 0.07903$. Again, we note that β of Eq.(4.34) depends on both ω and k_F, and the GE2 correlation coefficient β^{GE2} is also k_F-dependent.[200]

For simplicity, we fit the exact β curves, with the formula

$$\beta_{fit}(\nu) = \frac{\beta_0 + a_1\nu + a_2\nu^2 + \beta_\infty a_3\nu^3}{1 + a_4\nu + a_5\nu^2 + a_3\nu^3}, \tag{4.38}$$

with $\beta_0 = 3\mu_x^{GGA}/\pi^2$, and $\beta_\infty = 3(7/81)/\pi^2$. The fitted β curves are very smooth and follows strictly the original curve. It can be observed in Fig.4.1. The parameters required for fitted β are listed in Table 4.2.

With the form of functionals in hand, we apply all the hybrid methods to well known test sets. The hybrid method satisfying the LDA linear response will be shown with an
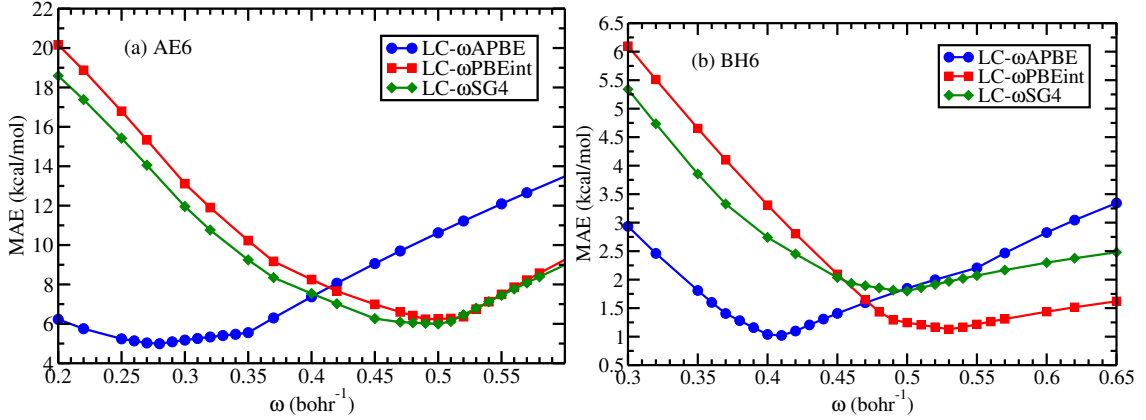
Figure 4.2: MAE plotted against ω for (a) AE6 data set, and (b) BH6 data set considering constructed LC hybrid XC functionals.

Table 4.3: Optimized values of the range-separated parameter ω (in bohr^{-1}) of constructed functionals.

LC-ωPBE	LC-ωAPBE	LC-ωPBEint	LC-ωSG4	LC-ωAPBE (β_{fit})	LC-ωPBEint (β_{fit})	LC-ωSG4 (β_{fit})
0.40	0.37	0.52	0.50	0.37	0.53	0.53

extension $-\beta_{fit}$ now onward. Before going to calculation part, we need the value of parameter ω.

The value of ω is optimized by minimizing the MAE of atomization energies (AE6) and barrier heights (BH6) test sets. For a particular value of ω, we calculate the MAEs of these test sets using developed hybrid functionals and are plotted in Fig. 4.2 and Fig. 4.3. It is observed that the LC-ωSG4 has the minimum at $\omega = 0.50$ bohr^{-1}. For LC-ωAPBE and LC-ωPBEint, we fix ω using $\omega = \omega_{min}^{AE6}/4 + 3\omega_{min}^{BH6}/4$ and the values of ω are obtained to be 0.37 bohr^{-1} and 0.52 bohr^{-1}, respectively. Next, for the β_{fit} functionals, we use the same formula as before to fix ω. The least MAE for these functionals in case of AE6 and BH6 data sets can be seen in Fig. 4.3. The values for ω in case of LC-ωAPBE(β_{fit}), LC-ωPBEint(β_{fit}), and LC-ωSG4(β_{fit}) are fixed to be 0.37 bohr^{-1}, 0.53 bohr^{-1}, and 0.53 bohr^{-1}, respectively.

In Table 4.3, we list the optimized values of ω for all the developed functionals along with a most used hybrid method LC-ωPBE. It is observed that the functionals with β_{fit} correlation have similar range separation parameters as original functionals.
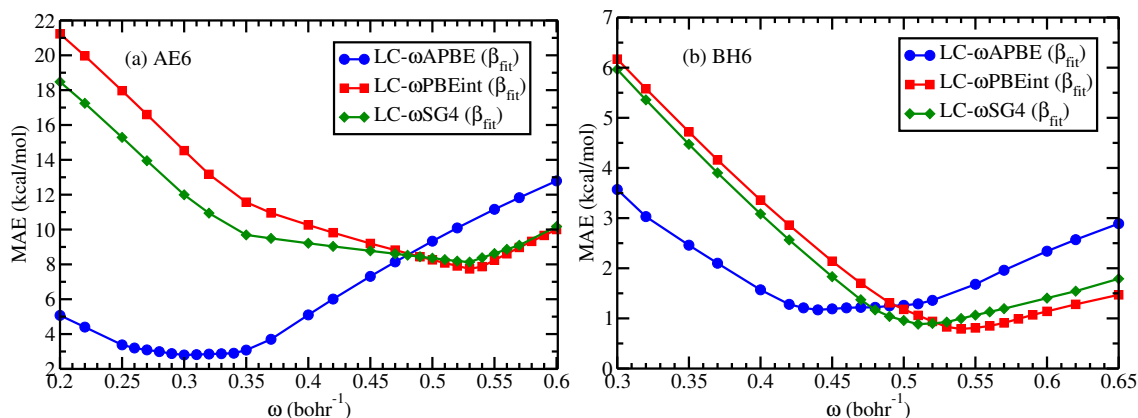
Figure 4.3: MAE plotted against ω for (a) AE6 data set, and (b) BH6 data set considering constructed LC hybrid XC functionals satisfying the LDA linear response.

4.1 Results for thermochemistry and noncovalent interactions

With optimized range-separated parameters available for all the functionals, they are ready to be applied to different test sets to assess the performances of these functionals against previously proposed functionals. So, we list the test sets that are employed to examine the functionals.

4.1.1 Benchmark test sets and computational details

The proposed LC-hybrid functionals are implemented in the NWCHEM software[201] to do the SCF calculations. We take help of Minnesota 2.0 data set[202] and G2/148 test set[203] to calculate atomization energies. The collected thermochemical and non-covalent interactions test sets are : (i) AE6 − test set of 6 small molecules,[202] (ii) G2/148 − atomization energy of 148 molecules. The reference CCSD(T) values of the G2/148 set are taken from ref. [42], (iii) PA8 - 8 proton affinities,[202] (iv) BH6 - 6 barrier heights,[202] (v) HTBH38 - 38 hydrogen transfers barrier heights,[202] (vi) NHTBH38 - 38 non-hydrogen transfers barrier heights,[202] (vii) BH76RC - energies of 30 chemical reactions,[204] (viii) HB6 - 6 hydrogen bond dissociation energies,[202,205,206,207] (ix) DI6 - 6 dipolar bond dissociation energies,[202,205,206,207] (x) PPS5 - 5 $\pi - \pi$ system dissociation energies,[202,205,206,207] (xi)

CT7 - binding energies of 7 charge transfer complexes,[202,205,206,207] (xii) ABDE12 - 12 alkyl bond dissociation energies,[202,205,206,207] (xiii) ISOL6 - isomerization energies of 6 large molecules,[202,208] (xiv) DC9 - 9 difficult cases,[202,209] (xv) HC7 - 7 hydrocarbon chemistry,[202,210]and (xvi) πTC13 - thermochemistry of 13 π systems.[202,211,212] All the calculations are performed using the $6-311++(3df, 3pd)$ basis set. The errors for all these test sets considering all the proposed functionals and LC-ωPBE functional are tabulated in Table 4.4. Due to large number of data sets the Table 4.4 extends to Table 4.5.

First, we calculate the atomization energies of two popular test sets AE6 and G2/148. Better atomization energies are necessary to claim a functional to be better. From Table 4.4, it can be observed that the LC-ωAPBE(β_{fit}) functional has the best MAE for both the test sets. The improvement is even better than the LC-ωPBE functional. But other β_{fit} functionals are not sustainable as fail to improve over their base LC functionals. The LC-ωSG4(β_{fit}) functional is the worst performing functional in both the AE6 and G2/148 test sets with MAE $\approx$ 8.1 kcal/mol. All the considered functionals are accurate in predicting the proton affinities. As applied to the PA8 test set, it is observed that the maximum error is 0.117 eV for LC-ωAPBE and LC-ωPBEint has the least error of 0.077 eV. Using the β_{fit} correlation energy the LC-ωAPBE(β_{fit}) improves the proton affinity in compare to original correlation, and the error reduced from 0.117 eV to 0.079. But this improvement of β_{fit} is not true always. It can be observed that for reaction barrier heights (BH6), LC-ωAPBE(β_{fit}) deteriorates the error from LC-ωAPBE. But in other two β_{fit} cases the error improve. In case of hydrogen reaction barrier heights (HTBH38), the least error is observed for LC-ωAPBE with MAE=1.20 kcal/mol, and all the three β_{fit} functionals have more errors. The worst observed error is 1.99 kcal/mol for LC-ωSG4(β_{fit}). But for non-hydrogen reaction barrier heights (NHTBH38), the use of β_{fit} correlation methods improve over regular correlation energies in LC hybrid functionals. The LC-ωAPBE(β_{fit}) method is the best with MAE=1.81 kcal/mol. The recalculated reaction barrier heights BH76RC test is a combined set of both HTBH38 and NHTBH38. The LC-ωAPBE has the minimum error and LC-ωAPBE(β_{fit}) has the second least error. So, the LDA linear response corrected functionals have moderate improvement over regular

Table 4.4: Mean errors and mean absolute errors of different test sets as obtained using various range-separated hybrid functionals. The last line represents the relative mean absolute error with respect to the LC-ωPBE. The Best/worst MAE of each test are shown in bold/underline style.

		LC-ωPBE ω = 0.40	LC-ωAPBE ω = 0.37	LC-ωPBEint ω = 0.52	LC-ωSG4 ω = 0.50	LC-ωAPBE(β_{fit}) ω = 0.37	LC-ωPBEint(β_{fit}) ω = 0.53	LC-ωSG4(β_{fit}) ω = 0.53
		atomization energy (kcal/mol)						
AE6	ME	0.24	6.29	0.51	-2.39	2.39	-1.33	-1.68
	MAE	5.37	6.29	6.36	5.99	**3.70**	7.74	<u>8.13</u>
		atomization energy of 148 molecules(kcal/mol)						
G2/148	ME	-0.20	-4.93	1.26	-0.67	-1.57	2.80	2.61
	MAE	4.32	5.64	6.25	5.21	**3.87**	7.85	<u>8.14</u>
		proton affinity (eV)						
PA8	ME	0.086	0.117	0.058	0.084	0.079	0.060	0.068
	MAE	0.086	<u>0.117</u>	**0.077**	0.097	0.079	0.078	0.082
		barrier heights (kcal/mol)						
BH6	ME	-1.64	-1.12	-0.62	-0.19	-1.75	-0.48	-0.13
	MAE	1.75	1.40	1.16	1.80	<u>2.10</u>	**0.83**	0.92
		hydrogen barrier heights (kcal/mol)						
HTBH38	ME	-0.57	-0.17	0.52	1.03	-0.78	0.67	1.09
	MAE	1.26	**1.20**	1.57	1.63	1.91	1.63	<u>1.99</u>
		non-hydrogen barrier heights (kcal/mol)						
NHTBH38	ME	1.55	1.35	3.24	3.60	0.29	3.12	3.04
	MAE	2.52	2.24	3.59	<u>3.75</u>	**1.81**	3.50	3.41
		reaction barrier heights recalculated (kcal/mol)						
BH76RC	ME	0.23	0.39	1.68	2.10	-0.40	1.71	1.91
	MAE	1.84	**1.66**	2.45	<u>2.72</u>	1.78	2.44	2.57
		hydrogen bonding dissociation energies (kcal/mol)						
HB6	ME	-0.67	-1.15	0.30	0.00	-0.52	0.55	0.72
	MAE	0.67	<u>1.15</u>	0.50	**0.43**	0.52	0.55	0.72

Table 4.5: Contuation of previous Table.

		LC-ωPBE $\omega = 0.40$	LC-ωAPBE $\omega = 0.37$	LC-ωPBEint $\omega = 0.52$	LC-ωSG4 $\omega = 0.50$	LC-ωAPBE(β_{fit}) $\omega = 0.37$	LC-ωPBEint(β_{fit}) $\omega = 0.53$	LC-ωSG4(β_{fit}) $\omega = 0.53$
		dipole bonding dissociation energies (kcal/mol)						
DI6	ME	0.73	0.88	0.15	0.46	0.40	0.03	-0.03
	MAE	0.73	0.88	0.32	0.50	0.40	0.23	**0.20**
		$\pi - \pi$ staking dissociation energies (kcal/mol)						
PPS5	ME	-1.41	-1.80	-0.88	-0.96	-1.32	-0.66	-0.28
	MAE	1.41	1.80	0.88	0.96	1.32	0.66	**0.48**
		dissociation energies of charge transfer complexes (kcal/mol)						
CT7	ME	-0.99	-1.11	-0.57	-0.82	-0.50	0.39	-0.23
	MAE	0.99	1.11	0.57	0.82	0.50	0.40	**0.34**
		alkali bond dissociation energies (kcal/mol)						
ABDE12	ME	-5.52	-7.94	-3.42	-4.32	-8.18	-3.57	-4.69
	MAE	5.52	7.94	**3.42**	4.32	8.18	3.57	4.69
		isomerization energies (kcal/mol)						
ISOL6	ME	0.56	1.00	-0.47	-0.42	1.59	-0.26	0.15
	MAE	**1.57**	1.95	2.11	2.07	2.01	2.13	2.17
		difficult cases (kcal/mol)						
DC9	ME	4.43	-9.22	16.59	15.06	8.92	17.27	15.09
	MAE	15.43	17.41	21.12	18.83	**13.97**	22.71	21.42
		hydrocarbon chemistry (kcal/mol)						
HC7	ME	9.74	10.53	24.27	24.29	2.31	21.13	15.99
	MAE	13.96	15.47	27.38	27.81	**7.04**	24.30	19.47
		thermochemistry of π systems (kcal/mol)						
πTC13	ME	4.05	4.92	3.61	4.26	4.20	3.81	4.26
	MAE	**4.24**	5.00	4.27	4.89	4.27	4.49	4.95
RMAE		1.00	1.15	1.04	1.11	**0.92**	1.04	1.06

methods in predicting reaction barrier heights.

Now, we discuss the capability of LC hybrid functionals in predicting dissociation energies of non-covalent interactions. In the first test set HB76 that contains six hydrogen bonded complexes, LC-ωSG4 is the best in describing the interaction energies. A considerable improvement is also observed by the linear response recovered method LC-ωAPBE(β_{fit}). For other non-covalent data sets dipole interacting systems (DI6 test), $\pi - \pi$ systems (PPS5 test), and dissociation energies of charge transfer molecular complexes (CT7 test), the LC-ωSG4(β_{fit}) has minimum errors in all the cases. The importance of LDA linear response satisfied correlation energies can be felt by observing the β_{fit} functionals and regular ones. Particularly, the LC-ωAPBE(β_{fit}) method improves a lot in comparison to LC-ωAPBE.

Next, in the alkali bond dissociation energies ABDE12 data set, the errors are not much sensitive to the β_{fit} correlation. In fact, the HF mixing percentage has more effect on this test set. The best functionals are LC-ωPBEint and LC-ωSG4, followed by LC-ωPBE, and the worst functionals are LC-ωAPBE and LC-ωAPBE(β_{fit}). For isomerization energies test set (ISOL6), it is clear that the LC-ωPBE is the best method with least MAE of 1.57 kcal/mol. However, the accuracy of all the functionals are acceptable as the MAEs are around 2 kcal/mol. The use of β_{fit} correlation marginally worsen the error in compare to original correlation. For nine complexes constituting DC9 test set and seven hydrocarbon chemistry HC7, the LC-ωAPBE(β_{fit}) is the best method. Finally, for the thermochemistry of thirteen π systems, the LC-ωPBE functional has the least error. The MAE of LC-ωAPBE(β_{fit}) is very close to the minimum error and it improves over the the regular LC-ωAPBE method.

In the end, we show the relative errors of present methods with the well-known and most used LC-hybrid LC-ωPBE in the last row of Table 4.5. The RMAE is calculated as

$$\text{RMAE} = \frac{1}{\text{M}} \sum_{i=1}^{\text{M}} \text{MAE}_i / \text{MAE}_{i,\text{LC}-\omega\text{PBE}},$$

where M is the total number of test sets used. We perceive that the local density linear response based LC-hybrids improve over their regular counterparts. The β_{fit} methods

are very close to the LC-ωPBE method. The LC-ωAPBE(β_{fit}) method is better than the LC-ωPBE functional as the RMAE is 0.92. However, all the methods are close to LC-ωPBE and the LC-ωAPBE(β_{fit}) method can be an alternate method for quantum chemistry calculation in hybrid level.

4.2   Summary and conclusions

The usefulness of the LC-hybrid functionals are discussed. We have presented a brief note on the way to construct LC-hybrid functionals. The range separated hybrid methods need the exchange hole of a given exchange functional and there is no direct derivation for the exchange hole. We adopted HJS model to construct exchange holes of three exchange energy functionals APBE, PBEint, and SG4. The constructed exchange holes are employed to make three type of LC-hybrid methods with corresponding correlation energy functionals. Here, we show that by separating the range and using some part of HF exchange in the exchange part of the hybrid method, the LDA linear response constraint is ignored. To address such issue, we proposed the correlation energies that make whole hybrid XC method to satisfy the LDA linear response. All the developed methods are applied to a wide range of test sets representing main-group thermochemistry and non-covalent interactions. It is seen that the proposed hybrid named LC-ωAPBE(β_{fit}) outperforms the well-known method LC-ωPBE in many cases. Overall, the proposed method to construct the correlation energy that will make the XC functional obey the LDA linear response will be very beneficial for future functional construction.

Chapter 5

Dispersion corrected semilocal density functionals for solid state and quantum chemistry applications

In this chapter, we explore the efficiency of DFT in describing the nonlocal, long-range, and weak dispersion interactions. Being one of the most used many-body approach, DFT is successfully applied to several fields from atoms, molecules, solids to larger-sized clusters. In principle, the way in which the electron-electron interaction is treated must contain all type of long or short-range interactions including the van der Walls (vdW). However, DFT at any level starting from LDA, GGA, meta-GGA to hybrid approximations is unable to account this weak, long-range interaction completely.[55,213,214,215] This weak interaction present in the dispersion bonded matter arises due to the long-range correlation between the electrons. The instantaneous quantum electronic charge fluctuations are the causes for such correlations and the construction of local or semilocal approximations do not include such concepts. Density functional approximations behave well when the densities of the considered system overlap, but in case of vdW interaction, the overlapping of densities are barely encountered. Therefore, to describe systems having such essential long-range correlations e.g. noble gas dimers, layered solids, bio-molecular complexes, the cluster of molecules, etc. within DFT, we need to add such correlation separately along with usual

E_{xc}. The wave function methods like MP2, CCSD(T) are capable of including the long-range correlation, but are very expensive calculations. Therefore, the semilocal method within DFT is the most preferred way for dispersion-bonded systems.

Several ways to include the nonlocal correlation are followed within DFT. However, the most common approach is to combine the long-range correlation with the approximated semilocal XC energy functional E_{xc}, i.e.,

$$E_{xc} = E_{xc}^{sl} + E_c^{nl},$$

(5.1)

where E_{xc}^{sl} is the semilocal XC energy and E_c^{nl} is the nonlocal correlation representing the long-range interaction. A number of approximations with different series such as DFT-D,[216,217,218] Tkatchenko-Scheffler (TS)[219,220,221] method, vdW-DF,[222,223,224,225,226] and exchange-hole dipole moment (XDM),[227,228,229,230] are proposed and extensively applied.[231,232] The well-known DFT+D series, in the prelimnary stage used the dispersion coefficient that depends on the dispersion coefficient of constituent atoms, a scaling parameter, and a damping function to cut-off the length of interactions. In later stages, the vdW coefficients are modified to depend on the chemical environments of elements. The advance vdW methods DFT-D3 and TS methods applied successfully to molecules and solids.[232,233,234] However, the accuracy of the calculation depends on the choice of both semilocal and nonlocal corrections.[235,236] Among these nonlocal corrections, we find the Rutgers-Chalmers method is preferred for solids having weak dispersion interactions.

Among various well-known nonlocal correlation methods, we find the Rutgers-Chalmers vdW-DF method is the most preferred method for vdW interacting solids. The vdW-DF method uses a nonlocal kernel connecting two densities, and the form of the correlation energy is written as,[224]

$$E_c^{nl} = \frac{1}{2} \int \int d\mathbf{r} d\mathbf{r}' \rho(\mathbf{r}) \Phi(\mathbf{r}, \mathbf{r}') \rho(\mathbf{r}'),$$

(5.2)

Here, the nonlocal kernel $\Phi(\mathbf{r}, \mathbf{r}') = \Phi(\rho(\mathbf{r}), \rho'(\mathbf{r}'), |\nabla\rho(\mathbf{r})|, |\nabla\rho'(\mathbf{r}')|, |\mathbf{r}-\mathbf{r}'|)$ is obtained from the adiabatic connection formula representing the density-density response function.

Different density dependent form of the nonlocal correlation part along with various form of semilocal density functionals are applied to molecules and solids,[237,238,239,240] successfully. Among such approximations, rVV10[241] method is simple and more accurate within the vdW-DF series. The rVV10 functional is the revised version of VV10 nonlocal correlation,[242] and both these exchange-correlation functionals have common semilocal E_{xc}, a refitted form of PW86[16] exchange functional(rPW86)[243] and the LDA correlation functional. Due to the adjustable parameters b and C present in non-local correction, the rVV10 long range correlation is compatible with any semilocal E_{xc}^{sl}. It is seen that the non-local corrections are more effective when added with semilocal functionals having no significant dispersion interactions. In other words, to avoid double counting of dispersion interaction the nonlocal correction should be used along with functionals giving no significant binding energy in van der Waals complexes. In a recent work,[244] Peng et al. combined the rVV10 nonlocal correlation with the SCAN[34] semilocal meta-GGA functional with appropriate parameter b. Also, the rVV10 correction is added to the Perdew-Burke-Ernzerhof (PBE),[17,245] PBE for solids (PBEsol),[246,247] GGA functional from semi-classical atom theory (SG4),[248,249] and Armiento and Mattsson (AM05).[250,251] In every cases, the parameters are different and are fixed to be suitable for respective functionals.

However, the Recently developed (TM)[42] meta-GGA functional suitable for both chemistry and solid-state systems is yet to be examined on dispersion bonded solids and molecules. In this work, we propose a van der Waals model combining the TM E_{xc}^{sl} and rVV10 non local correlation. The present method is applied to a wide range of test sets comprising of molecules and solids. As, we are fixing the parameters from the layered material test set, we name the functional as TM+rVV10L.

5.1 Theoretical background

5.1.1 The rVV10 nonlocal correlation

As mentioned above, the rVV10 nonlocal correlation is modified over the VV10 correlation kernel, and both of them are based on vdW-DF[224] nonlocal functionals and are

written as

$$E_c^{nl} = \int d\mathbf{r}\rho(\mathbf{r})\left[\frac{1}{2}\int d\mathbf{r}'\rho(\mathbf{r}')\Phi(\mathbf{r},\mathbf{r}') + \beta\right]. \tag{5.3}$$

Here, $\Phi(\mathbf{r},\mathbf{r}')$ is the correlation kernel same as Eq.(5.2), $\beta = \frac{1}{32}[\frac{3}{b^2}]^{3/4}$ is a parameter used to control the short-range damping of the R^{-6} ($R = |\mathbf{r}-\mathbf{r}'|$) asymptotic. The rVV10 Kernel is written as

$$\Phi^{rVV10} = -\frac{3}{2}\frac{1}{(qR^2+1)(q'R^2+1)(qR^2+q'R^2+2)}, \tag{5.4}$$

where $q(\mathbf{r}) = \omega_0(\mathbf{r})/k(\mathbf{r})$ and similarly for q'. Here,[242]

$$\omega_0(\mathbf{r}) = \sqrt{\omega_g^2(\mathbf{r}) + \frac{\omega_p^2(\mathbf{r})}{3}}, \tag{5.5}$$

$k(\mathbf{r}) = 3b\frac{\omega_p(\mathbf{r})}{k_s^2(\mathbf{r})}$, $k_s = \sqrt{3}\omega_p/v_F$ is the Thomas-Fermi screening wave vector, and the local Fermi velocity given as $v_F = (3\pi\rho)^{1/3}$. The ω_p is the local plasma frequency related to the density as $\omega_p^2 = 4\pi\rho$ and the local band gap given by

$$\omega_g^2(\mathbf{r}) = C\left|\frac{\nabla\rho(\mathbf{r})}{\rho(\mathbf{r})}\right|^4. \tag{5.6}$$

Now, we have two parameters, b present within β, and parameter C present in Eq.(5.6). The parameter C is used to extract an accurate C_6 coefficient of van der Waals interaction. Due to presence of these two parameters, rVV10 functional is more flexible with any semilocal E_{xc}.

5.1.2 The TM and TMTPSS functional

We outline the construction of the TM functional so that it will be convenient to understand the influence of the semilocal as well as the nonlocal correlation effects. As mentioned, the TM functional is constructed from the DME, and it is correct up to fourth-order gradient expansion (GE4[252]) for solids. Rewriting the XC energy form using en-

hancement factor Eq.(1.50),

$$E_{xc}^{TM}[\rho_\uparrow, \rho_\downarrow] = \int d^3r \rho \varepsilon_{xc}^{unif}(\rho_\uparrow, \rho_\downarrow)[wF_x^{DME} + (1-w)F_x^{sc}]. \tag{5.7}$$

The weight factor $w = [(\tau_W/\tau)^2 + 3(\tau_W/\tau)^3]/[1 + (\tau_W/\tau)^3]^2$ controls the portion of compact density (for which the DME is accurate) and the slowly varying correction (for which the GE4 is accurate). For homogeneous electron density, w is 0 and for one-electron bound-state densities, $w = 1$. The von Weizsäcker[253] kinetic energy density $\tau_W = |\nabla\rho|^2/8\rho$ is used. The spin-unpolarized form of the DME part of the enhancement factor written as,

$$F_x^{DME} = \frac{1}{f^2} + \frac{7}{9f^4}\left\{1 + \frac{595}{24}(2\lambda-1)^2 p \right. \tag{5.8}$$
$$\left. - \frac{1}{\tau^{unif}}\left[\tau - 3(\lambda^2 - \lambda + \frac{1}{2}) \times (\tau - \tau^{unif} - \frac{1}{72}\frac{|\nabla\rho|^2}{\rho})\right]\right\},$$

where $f = [1 + 10(70y/27) + \beta y^2]^{1/10}$, $y = (2\lambda-1)^2 p$, and $\beta = 79.873$. And $p = s^2 = (|\nabla\rho|/2k_F\rho)^2$ with the Fermi vector being defined as $k_F = (3\pi^2\rho)^{1/3}$, and τ^{unif} is the uniform kinetic energy density. The fourth order gradient expansion required for slowly varying electron density is included through F_x^{sc} as given in Eq.(1.51). Because of the use of both F_x^{DME}, and F_x^{sc} along with the weight factor, the TM functional able to perform well in both uniform and slowly-varying-density limiting conditions. In the work of TM, both TPSS,[30] and a modified form of TPSS correlation energy are combined with the exchange energy. The correlation energy of TPSS is modified through $C(\zeta, \xi)$ (present in Eq. 12 of Ref. [30])

$$C(\zeta, \xi) = \frac{0.1\zeta^2 + 0.32\zeta^4}{\{1 + \xi^2[(1+\zeta)^{-4/3} + (1-\zeta)^{-4/3}]/2\}^4}, \tag{5.9}$$

where $\zeta = (\rho_\uparrow + \rho_\downarrow)/\rho$ is the spin-polarization and $\xi = |\nabla\zeta|/2k_F$. The imposed small change make the correlation functional more compatible with the TM exchange by improving the behavior in the low-density limit. The combination of TM exchange with modified TPSS correlation, and with the original TPSS correlation energies are called
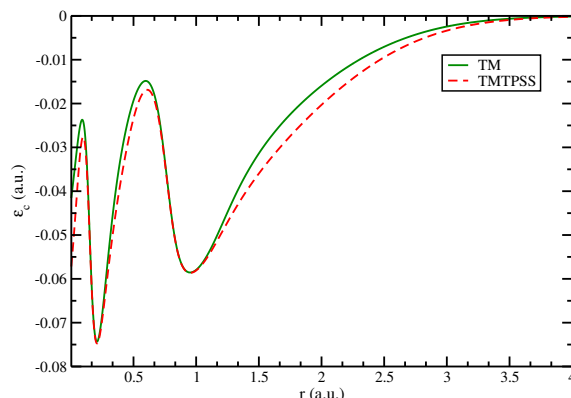
Figure 5.1: The correlation energy per electron is plotted against the radial distance for the argon atom.

TM and TMTPSS functional, respectively. It is to be noted that, both the correlation energies are one-electron self-interaction free. To get a clear picture of these two correlation energies, we plot the correlation energy per particle for Ar atom using both the functionals in Fig. 5.1. It can be seen that, within the core region both the functionals do not show any significant difference. However, in the valence region, the difference is clear, and TMTPSS decays slower than the TM. We believe that such small difference in the valence region will have notable effect on long-range chemical properties. Also, it is concluded that the TM correlation functional is slightly better than TMTPSS functional.

5.1.3   Compatibility and parameters for rVV10 with TM and TMTPSS

First, we need some analysis on the choice of functionals in the combination of rVV10. Both the functionals in the semilocal form are applied to a test set of 26 layered materials.[251] The inter-layer distance and the binding energies of these layered materials are dominated by van der Waals interactions. It is seen that the GGA functionals (e.g., PBE, PBEsol, etc.) usually underestimate the binding energies and incorrectly bind the layers due to absence of the vdW interaction.[249,251] Whereas, the SCAN functional, that contains some amount of the short and intermediate vdW interactions possess improved results than GGAs.[244] It was discussed that the TM functional also includes some part of the vdW interaction through the DME exchange hole.[254] The correlation of TM functional respects

the low-density or strong interaction limiting conditions. As a result, TM behaves better compared to the SCAN in the case of noncovalent interactions, layer-layer binding energy (E_b), interlayer lattice constants (c), and hydrogen-bonded systems.[255,256,257] But this improvement is not up to mark in case of TMTPSS method, and it is seen that TMTPSS have quite different solid state properties compare to TM. For example, the inter-layer binding energies and the inter-layer lattice constants are underestimated by TMTPSS more than the TM. So, we examine the compatibility of both these methods with the rVV10 non-local correlation. For this, we need to fix the above discussed parameters b, and C of rVV10 correction for TM, and TMTPSS, separately. To get a rough idea, first, we plot the binding energy of graphite using SCAN, TM, and TMTPSS functionals in Fig. 5.2. From this plot, it is clear that both TM and TMTPSS methods have quite improved curve than the SCAN, but still away from the reference RPA binding energy. By analyzing the fixed parameter of SCAN+rVV10,[244] we expect TM+rVV10, and TMTPSS+rVV10 require higher values of b than 15.7. It is because the non-local correlation varies inversely with b, and $b = 15.7$ is fixed for SCAN+rVV10. Now, the proposed dispersion corrected XC functional is given as

$$E_{xc}^{TM/TMTPSS+rVV10L} = E_x^{TM} + E_c^{TM/TPSS} + E_c^{rVV10}. \tag{5.10}$$

From previous work, it is observed that to fix the parameters, different ways have been adopted by different authors. Keeping the value of parameter $C = 0.0093$(at its original value[242]), the value of b is determined by using a set of molecular complexes,[241,242] determining the binding energy curve of rare-gases,[244] and from layered materials test set.[245,251] Besides, some authors preferred to change[247,249,251] the value of constant C. In our work, we fix $C = 0.0093$ as the effect of C is not so drastic for our chosen semilocal functional. And b is fixed comparing the calculated binding energies of 26 layered materials(present in (Table 5.2) with the RPA reference values. The fixed parameters $b = 25$ and 22.7 are for TM+rVV10L and TMTPSS+rVV10L, and L is added to the names because the parameters are fixed using layers. As discussed before, such higher values of b and order of b for these functionals (SCAN<TMTPSS<TM) are expected.
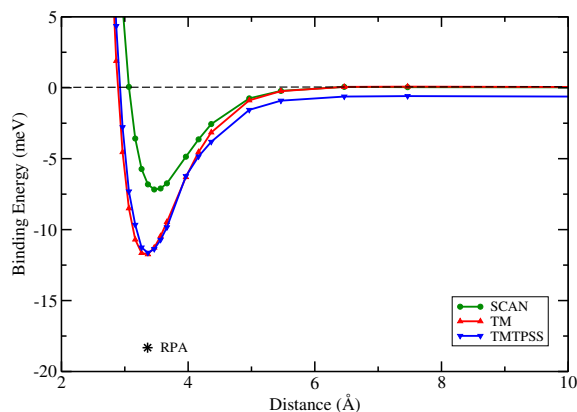
Figure 5.2: The binding energy curves as obtained from TM and TMTPSS functionals for bi-layer graphene are shown. The SCAN binding energy curve is also given for comparison along with the RPA binding energy value.

5.2 Computational details and Results

To apply proposed dispersion methods on molecules and solids, we discuss the prerequisites for the calculations. The calculations are done with the projector-augmented-wave (PAW) method as implemented within the Vienna *ab initio* simulation package (VASP).[147,148,149,150] First, TM and TMTPSS functionals are implemented in the VASP code, and the rVV10 dispersion method as implemented by Peng et al.[244] is used. An orthorhombic box having $23 \times 24 \times 25$ Å^3 dimension is used to perform the calculations of noble gases, and complexes present in the S22 data set.[259] For larger complexes L7 test set,[260] we use 30Å sided cube. A plane wave energy cutoff 650 eV, 900 eV, and 1200 eV are used for L7, S22, and nobles gases, respectively. A single Γ point is used for sampling the Brillouin-zone of all the molecular calculations, and an energy convergence criterion of 10^{-6} is used. The energy cutoff of 800 eV was used in all calculations along with the k-point sampling of $16 \times 16 \times 8$ and $16 \times 16 \times 1$ for bulk and monolayers are used. For physisorption calculations, the plane-wave energy cutoff of 600 eV and k-point sampling of $8 \times 8 \times 1$ Monkhorst-Pack[262] are employed. To avoid interaction between layers in the perpendicular direction, we used a vacuum layer of 20Å. All the considered test sets are summarized in Table 5.1.

Table 5.1: Test sets used in this work

Test set	description
26 layer solids[251]	26 layer materials for interlayer, intralayer lattice constants and binding energy
NGS4[258]	Lattice constants and cohesive energies for four noble -gas solids
NG2[244]	Binding energy of 2 Noble gas dimer (Ar_2 and Kr_2)
S22[259]	binding energy of 22 non-covalent interactions
L7[260]	7 large molecular complexes with more long-range dispersion effect
Physisorption[261]	adsorption of Ar, Kr, and Xe noble gases on different metal surfaces

5.2.1 Layered materials

The interaction between different layers of material are dominated by the vdW interaction. To predict inter-layer lattice constant and binding energies of such materials, dispersion corrected methods are essential. Due to extensive practical applications of such materials, synthesis and electronic structure calculations of new predicted materials are present-day research interests.[264,265,266,267] We calculate the inter-layer lattice constant c and binding energies E_b of 26 layered materials[251] using proposed new dispersion corrected methods and their bare semilocal methods. Inter-layer lattice constants and the distance between any two layers are dominated by the vdW interaction, but the intralayer lattice constant a of these materials are dominated by covalent interactions. So, we tabulated only c, and E_b for these 26 layers using TM, TMTPSS, TM+rVV10L, and TMTPSS+rVV10L in Table 5.2. Also, we provide the RPA reference values[251] of binding energies, and experimental inter-layer lattice constants of this test set for comparison. Focusing on two bare semilocal methods, it is clear that only semilocal DFT significantly underestimates the binding energies and loosely binds the layers. Between TM and TMTPSS, TM is more

Table 5.2: Binding energy (E_b) in meV/Å^2 and interlayer lattice constant c in Å for a set of 26 layered materials are shown. The RPA values for E_b and the experimental c values taken as reference from Ref.[251, 263]. The last two rows represent MAE and MAPE.

	Reference		TM		TMTPSS		TM+rVV10L		TMTPSS+rVV10L	
	E_b	c	E_b	c	E_b	c	E_b	c	E_b	c
Graphite	18.32	6.70	11.28	6.63	10.71	6.71	18.69	6.43	18.76	6.51
H-BN	14.49	6.54	12.54	6.47	11.82	6.56	19.44	6.30	19.54	6.38
HfS$_2$	16.13	5.84	9.56	5.89	8.38	5.95	16.97	5.83	16.56	5.83
HfSe$_2$	17.09	6.16	10.34	6.21	9.10	6.29	17.61	6.13	17.14	6.18
HfTe$_2$	18.68	6.65	13.00	6.76	10.27	6.86	20.67	6.66	18.79	6.76
MoS$_2$	20.53	12.3	11.37	12.49	9.63	12.61	21.79	12.27	20.93	12.38
MoSe$_2$	19.63	12.93	11.69	13.15	10.10	13.3	21.52	12.95	20.77	13.06
MoTe$_2$	20.80	13.97	18.86	14.21	16.33	14.4	22.84	13.99	21.54	14.16
NbSe$_2$	19.57	12.55	14.96	12.67	12.41	12.89	24.55	12.52	22.84	12.65
NbTe$_2$	23.03	6.61	18.86	6.93	16.33	7.08	26.84	7.04	26.32	7.04
PbO	20.25	5.00	19.71	4.78	17.68	4.87	26.71	4.71	25.11	4.71
PdTe$_2$	40.17	5.11	32.85	5.08	26.72	5.17	42.23	5.08	36.67	5.14
PtS$_2$	20.55	5.04	12.07	5.19	10.07	5.36	21.71	4.99	20.42	5.14
PtSe$_2$	19.05	5.11	12.37	5.25	8.10	5.54	22.19	5.07	18.59	5.30
TaS$_2$	17.68	5.90	12.79	5.99	11.00	6.06	23.19	5.94	21.47	5.95
TaSe$_2$	19.44	6.27	13.39	6.37	11.89	6.44	22.7	6.28	21.57	6.33
TiS$_2$	18.88	5.90	13.75	5.72	11.91	5.79	21.54	5.70	20.83	5.71
TiSe$_2$	17.39	6.27	14.41	6.05	12.26	6.17	22.02	6.04	20.79	6.05
TiTe$_2$	19.76	6.50	17.07	6.56	13.47	6.69	24.53	6.54	21.93	6.61
VS$_2$	25.61	5.75	16.50	5.85	14.38	5.93	24.59	5.81	24.54	5.82
Vse$_2$	22.26	6.11	15.59	6.27	12.88	6.34	23.38	6.11	22.92	6.21
WS$_2$	20.24	12.32	10.89	12.58	9.26	12.68	21.47	12.36	20.76	12.39
Wse$_2$	19.98	12.96	11.43	13.22	9.54	13.37	21.60	13.03	19.16	13.03
ZrS$_2$	16.98	5.81	9.96	5.87	8.75	5.93	17.28	5.77	16.80	5.82
ZrSe$_2$	18.53	6.13	10.87	6.19	9.57	6.27	18.09	6.14	17.53	6.16
ZrTe$_2$	16.34	6.66	14.36	6.72	12.55	6.84	21.71	6.65	20.68	6.74
MAE	–	–	6.01	0.13	8.18	0.21	2.59	**0.07**	**1.75**	0.11
MAPE	–	–	30.3	1.88	41.37	2.93	13.64	**1.18**	**9.16**	1.64
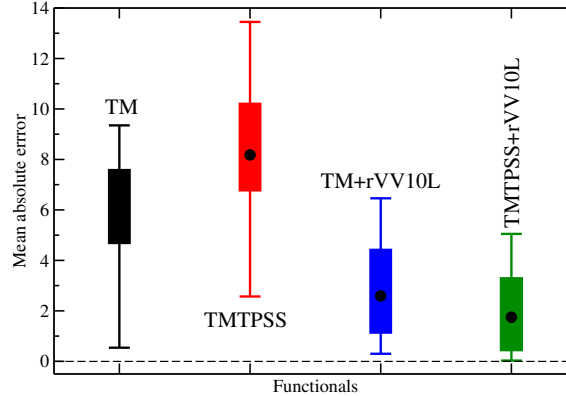
Figure 5.3: Ahown are the box plots of absolute errors of layered materials' binding energies. Discussed functionals TM, TMTPSS and their dispersion corrected part are considered. The lower and upper ends of whiskers represent the minimum and maximum absolute error values. The quartile one (Q1) point of represented by the bottom of the box keep 25% of errors below this point, and above the quartile three (Q3) point represented by the top of the box 25% of errors falls. The median for the errors are presented by the parallel lines present within the respective boxes of different methods and the black circles represent the mean.

accurate in predicting both c, and E_b than TMTPSS. The addition of rVV10 nonlocal correlation increases the accuracy in predicting both c, and E_b. The TMTPSS+rVV10L is better for binding energies and the error is less than that of TM+rVV10L, but in the performance of interlayer lattice constant c, TM+rVV10L is better. Also, 50% reduction in the MAE of c is observed by the addition of rVV10 vdW correction.

In Fig. 5.3, we show the box plots for absolute errors of binding energies. The minimum and maximum error values represented by lower end and upper end of vertical lines. The quartile one (Q1) point represented by lower end of rectangular boxes below which 25% of data lies, and above Q3 presented by upper end of box, 25% of data lies. The median and the mean of the errors are presented by the bands and the dark circles within the boxes. The Q1 and Q3 points of TMTPSS+rVV10L are smaller than those of TM+rVV10L. For a better understanding, in Fig. 5.4, we plot the mean errors in the binding energies and mean errors of interlayer lattice constant for the complete data set. The main figure is for Two dispersion corrected functionals TM+rVV10L and TMTPSS+rVV10L, and the inset is for the bare semilocal functionals. The underestimation in the binding energy for bare semilocal methods is clear from the inset figure, as the
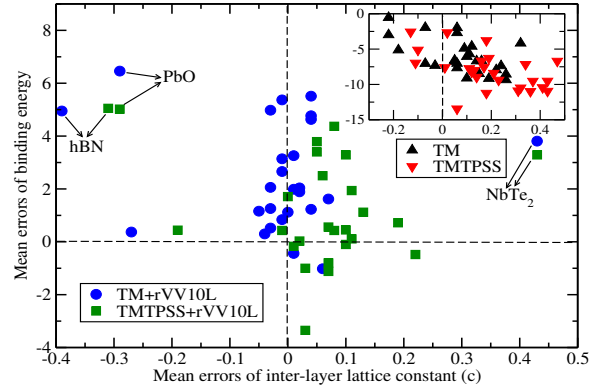
Figure 5.4: Mean errors in binding energies of layered materials versus mean errors in interlayer lattice constant these twenty-six materials (Table 5.2). The dispersion corrected methods are in the main figure, and the bare semilocal functionals are in the inset.

Table 5.3: The MAE and MAPE in binding energy (E_b) and lattice constant (c) of different functionals for 26 layered materials. The references for the collected functionals are given in bottom of the table. The smallest values are in bold font.

Methods	E_b		c	
	MAE	MAPE	MAE	MAPE
SCAN[a]	12.37	62.38	0.32	4.34
TM	6.01	30.30	0.13	1.88
TMTPSS	8.18	41.37	0.21	2.93
PW86R-VV10[b]	10.01	52.49	0.09	1.29
PW86R-VV10sol[b]	**1.52**	**7.05**	0.25	3.38
AM05-VV10sol[b]	2.26	11.13	0.16	2.19
rev-vdW-DF2[a]	4.66	24.77	**0.07**	**1.12**
PBE+rVV10L[c]	1.70	8.68	0.15	2.04
PBEsol+rVV10s[d]	2.86	14.57	0.08	1.39
SCAN+rVV10[a]	1.62	8.37	0.08	1.29
TM+rVV10L	2.59	13.64	**0.07**	1.18
TMTPSS+rVV10L	1.75	9.16	0.11	1.64

a-Ref. [244], b-Ref. [251], c-Ref. [245], d-Ref. [247]

ME in binding energies fall below the zero line. And the underbinding in c is clear, as most of the errors in interlayer lattice constants fall in the right zone. The improvement due to the addition of vdW correction are understandable as comparative more number of points are close to the crossing point of two zero lines. To get an idea of the accuracy of the present methods, in Table 5.3, we list the MAE and MAPE of some available vdW corrected methods for the layered material test set. Among three semilocal functionals and nine long-range corrected functionals, PW86R-VV10sol method[251] has the least error in the binding energy. For lattice constant c, both rev-vdW-DF2[240] and TM+rVV10L are equally good. However, three meta-GGA functionals in combination with rVV10 correction, i.e., SCAN+rVV10, TM+rVV10L, and TMTPSS+rVV10L methods are close in describing the layered materials.

5.2.2 Noble-gas Solids

In the formation of noble-gas solids, the dispersion interaction is crucial. In accessing the proposed vdW methods, we calculate lattice constants and cohesive energies of a test set containing four noble gas-solids Ne, Ar, Kr, and Xe.[258,268,269,270] We present the lattice constants, and cohesive energies for TM, TMTPSS, TM+rVV10L, TMTPSS+rVV10L along with the experimental results in Table 5.4. It is observed that the semilocal functionals without the vdW correction are quite good in describing the lattice constants of noble-gas solids. Due to addition of rVV10 to these semilocal functionals, the equilibrium lattice constant reduces and goes away from the reference values resulting overbinding of atoms. The TM method is the best among considered functionals with MAE of 0.14 Å. Though the vdW methods TM+rVV10L, and TMTPSS+rVV10L unable to increase the accuracy in describing lattice constants, they are impressively good for cohesive energies. From the lower panel of Table 5.4, the cohesive energies of TM, and TMTPSS are far from the reference and addition of nonlocal correction significantly increases the the cohesive energies towards the experimental values. Between the bare meta-GGA methods, TM is better than that of TMTPSS, however TMTPSS+rVV10L has the least error, and TM+rVV10 is good for all the solids except Ne.

Table 5.4: The lattice constants (in Å) and Cohesive energies(in meV/atom) of first four noble-gas solids as obtained using considered functionals are tabulated. The reference experimental values[258,268] are given in the last column. The bold font numbers are the MAE and MAPE.

Solids	TM	TMTPSS	TM+rVV10L	TMTPSS+rVV10L	Expt.
			Lattice constants (Å)		
Ne	3.97	3.93	3.90	3.83	4.35
Ar	5.16	5.18	5.05	5.05	5.23
Kr	5.60	5.62	5.47	5.47	5.61
Xe	6.13	6.19	6.00	6.03	6.10
MAE	**0.14**	0.15	0.24	0.16	–
MAPE	**3.10**	3.34	5.01	3.65	–
			Cohesive energies (meV/atom)		
Ne	36.0	22.9	51.0	43.3	27.2
Ar	69.4	66.4	98.4	98.9	88.9
Kr	83.5	78.8	118.9	117.8	122.5
Xe	102.2	94.3	151.5	148.3	169.8
MAE	33.7	36.4	13.8	**12.5**	–
MAPE	31.4	30.2	27.9	**19.9**	–

5.2.3   Noble-gas dimers

Similar to noble-gas solids, the formation of noble-gas dimers mainly depend on vdW interaction. The prediction of correct interaction energy curves of noble-gas dimers that shows the correct bond length and the binding energy has been a tough task for DFT. In an attempt to apply semilocal as well as nonlocal corrected methods, we plot the binding energy curves for Ar_2, and Kr_2 dimer in Fig. 5.5. Such assessment is necessary to examine the stability and effect of vdW corrections. From these plots, it is clear that the semilocal methods are able to bind the monomers but the energy values are far from the CCSD(T) reference values. And the improved calculated energies corresponding to different atomic distances by the use of rVV10 correction are clear. Though both TM+rVV10L, and TMTPSS+rVV10L are close to CCSD(T) curve, TMTPSS+rVV10L behaves better than TM+rVV10L. The deviation from the reference curve by TM+rVV10L is expected due to comparatively larger value of parameter b. We observe the binding energy curve for TM+rVV10L will get very close to the CCSD(T) for $b = 12.5$. However, such smaller b
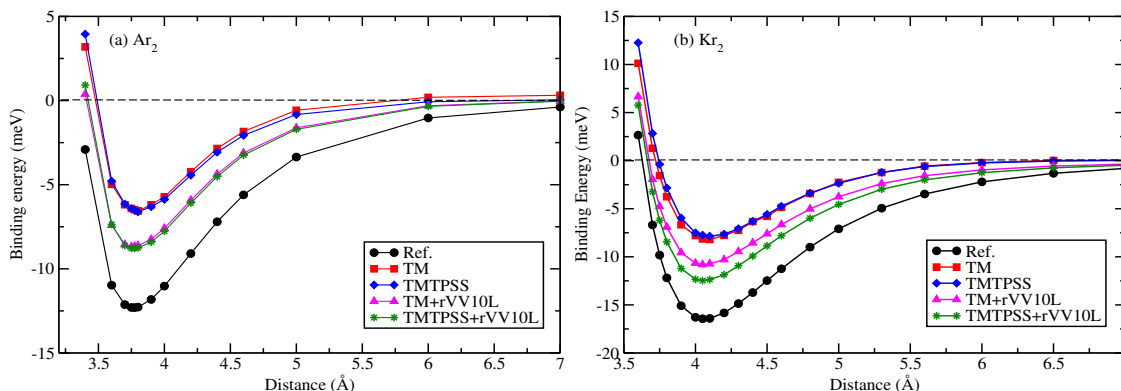
Figure 5.5: (a) Binding energy curves of Ar_2 dimer, and (b) Kr_2 dimer using TM, TMTPSS and corresponding dispersion corrected methods.

will cause unacceptable errors in all other test sets. Again, it can be seen that the fixed parameters for both TM+rVV10L and TMTPSS+rVV10L give minimum energy values at the equilibrium distance of 3.75 Å for Ar_2 and 4.05 Å for Kr_2 respectively, which are very close to the CCSD(T) results.

5.2.4 The S22 benchmark set

The S22 data set[259] is a very relevant test set for applying new proposed vdW functionals. Out of twenty two complexes, seven are hydrogen-bonded, eight dispersion dominated, and seven mixed complexes. In Table 5.5, the interaction energies of all these complexes are tabulated for TM and TMTPSS semilocal methods, TM+rVV10L and TMTPSS+rVV10L vdW methods, and CCSD(T) reference values. The bare TM functional is very accurate for all the subsets of S22, and it is far better than TMTPSS with the MAE of 0.50 kcal/mol. Also, this is the least error for this test set. The nonlocal correction to TM leads the interaction energies to differ from the reference resulting increase of MAE. However, the MAPE for TM+rVV10L is lesser than the bare TM. Between two rVV10 corrected methods, the MAE of TMTPSS+rVV10L, and MAPE of TM+rVV10L are lesser in magnitude. Also, the TMTPSS+rVV10L has more accurate binding energies of H-bonded complexes, and both nonlocal corrected methods are quantitatively similar in case of dispersion and mixed bonded complexes. In attempt to compare the performance

Table 5.5: Binding energies (in kcal/mol) for complexes present in S22 data set using TM, TMTPSS, TM+rVV10L, and TMTPSS+rVV10. The CCSD(T) values[271,272] are tabulated for reference.

Complexes (Symmetry)	CCSD(T)	TM	TMTPSS	TM+rVV10L	TMTPSS+rVV10
7 hydrogen-bonded complexes					
NH$_3$ dimer (C$_{2h}$)	3.15	3.34	2.88	3.01	2.96
H$_2$O dimer (C$_s$)	5.00	5.32	5.05	5.30	5.12
Formic acid dimer (C$_{2h}$)	18.75	19.95	18.90	19.94	19.19
Formamide dimer (C$_{2h}$)	16.06	16.73	14.07	13.83	14.35
Uracil dimer (C$_{2h}$)	20.64	19.87	17.10	17.22	17.60
2-pyridone-2-aminopyridine (C$_1$)	16.94	17.33	14.04	14.20	14.58
Adenine-thymine WC (C$_1$)	16.74	16.27	13.16	13.48	13.80
8 dispersion-bound complexes					
CH$_4$ dimer (D$_{3d}$)	0.53	0.45	0.44	0.52	0.52
C$_2$H$_4$ dimer (D$_{2d}$)	1.48	1.39	1.35	1.56	1.52
Benzene-CH$_4$ (C$_3$)	1.45	0.91	1.07	1.37	1.30
Benzene dimer (C$_{2h}$)	2.66	2.02	1.82	2.63	2.56
Pyrazine dimer (C$_s$)	4.26	3.32	3.17	4.02	3.92
Uracil dimer (C$_2$)	9.78	9.08	8.61	9.89	9.77
Indole-benzene (C$_1$)	4.52	3.61	3.25	4.48	4.33
Adenine-thymine (C$_1$)	11.66	11.1	10.38	12.03	11.98
7 mixed complexes					
C$_2$H$_4$-C$_2$H$_2$ (C$_{2v}$)	1.50	1.31	1.09	1.23	1.19
Benzene-H$_2$O (C$_s$)	3.28	3.28	3.31	3.63	3.52
Benzene-NH$_3$ (C$_s$)	2.32	2.25	2.09	2.34	2.31
Benzene-HCN (C$_s$)	4.54	4.41	4.07	4.47	4.32
Benzene dimer (C$_{2v}$)	2.72	1.94	1.95	2.50	2.42
Indole-benzene (C$_s$)	5.63	4.78	4.42	5.17	5.07
Phenol dimer (C$_1$)	7.1	6.47	6.32	7.04	6.89
MAE	−	**0.50**	1.02	0.71	0.62
MAPE (Δ)	−	10.88	15.84	**7.08**	7.20

Table 5.6: MAE and MAPE of S22 data set for some available functionals.

Methods	MAE	MAPE
SCAN[a]	0.94	20.7
TM	0.50	10.88
TMTPSS	1.02	15.82
PW86R-vv10[b]	0.35	4.87
PW86R-VV10sol[b]	1.17	26.47
AM05-VV10sol[b]	1.44	36.27
vdW-DF2[a]	0.94	14.71
rVV10[a]	**0.30**	**4.52**
SCAN+rVV10[a]	0.43	6.46
TM+rVV10L	0.71	7.08
TMTPSS+rVV10L	0.62	7.20

a-Ref. [244], b-Ref. [251]

Table 5.7: Interaction energies in kcal/mol of L7 data set for different functionals. The structure and reference QCISD(T) values are collected from Ref. [260]. The calculated MAE and MAPE for all these complexes, calculated taking QCISD(T) as reference values, are tablulated in the last two rows. The bold font numbers are the least errors.

L7 Complexes	QCISD(T)	SCAN	TM	TMTPSS	SCAN+rVV10L	TM+rVV10L	TMTPSS+rVV10L
Octadecane dimer (CBH)	-11.06	-3.40	-6.34	-6.08	-8.23	-8.83	-11.45
Guanine trimer (GGG)	-2.40	0.84	-0.53	-0.36	-1.50	-1.73	-2.39
Circumcoronene···Adenine dimer (C3A)	-18.19	-7.35	-10.54	-9.99	-13.83	-13.88	-16.82
Circumcoronene···Guanine-cytosine dimer (C3GC)	-31.25	-13.04	-18.94	-17.97	-24.41	-24.75	-28.21
Phenylalanine trimer (PHE)	-25.76	-22.65	-20.73	-20.54	-25.94	-22.57	-23.52
Coronene dimer (C2C2PD)	-24.36	-8.22	-12.46	-11.79	-16.77	-16.74	-19.08
Guanine-cytosine dimer (GCGC)	-14.37	-0.25	4.68	4.94	-6.05	2.09	-0.56
MAE	−	10.47	8.93	9.37	4.43	5.85	**3.75**
MAPE	−	71.24	57.56	60.54	28.18	35.82	**21.10**

of the newly proposed methods with previously developed functionals, we list MAE and MAPE of the interaction energies in Table 5.6. It is observed that for S22 test set, the parent rVV10 method is better than other methods with MAE of 0.30 kcal/mol. To get a clear idea of error statistics, we show a box plot in Fig. 5.6 for the absolute errors of all the complexes present in S22. The maximum difference of TM for any complexes is very less and it is suitable for all the complexes present in S22. Though the top end of the whiskers are comparatively higher in position for the rVV10 corrected functionals, 50% of the absolute errors represented by the median line, and 75% of errors represented by Q3 are below 0.23 kcal/mol, and 0.45 kcal/mol respectively.
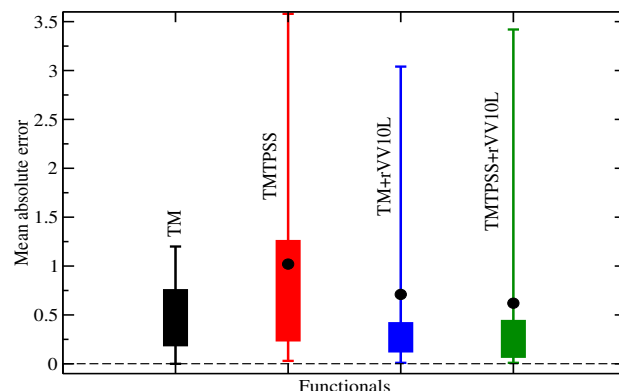
Figure 5.6: Box plots for absolute errors in interaction energies of S22 data set using all the functionals. The description of all box plots are similar to 5.3.

5.2.5   L7 molecular data set

After applying the developed vdW methods to noble gases and smaller molecular complexes, we examine the performance on large-sized complexes combined under L7 data set.[260] Such large complexes require significant amount of dispersion interaction to bind the complexes. Such data set dominated by dispersion interaction is a challenge to new contemporary vdW methods. In Ref.,[260] importance of these complexes, the structures, and the reference binding energies can be perceived. Applying SCAN, TM, and TMTPSS meta-GGA functionals, and nonlocal correlation added functionals SCAN+rVV10, TM+rVV10L, and TMTPSS+rVV10L to this test set, we list the interaction energies in Table 5.7. Besides theses methods, we collect quadratic configuration interaction(QCISD(T)) values for reference. Analyzing Table 5.7, it is observed that, the binding energies of bare SCAN functional are far from the QCISD(T) values, and SCAN unable to bind the guanine trimer (GGG). Both the errors of TM and TMTPSS are better than SCAN but they fail to bind guanine-cytosine dimer (GCGC). The improved binding energies by adding the nonlocal correlation to the semilocal E$_{xc}$ are clear for all the vdW methods. Among all the vdW methods only TM+rVV10L does not bind GCGC complex, but all other functionals SCAN+rVV10 and TMTPSS+rVV10L have negative binding energies for all the large complexes. Except Guanine-cytosine base pairs, the interaction energies of TMTPSS+rVV10L functional are more close to reference values. Also, it is observed that

the errors for TMTPSS+rVV10L reduces 50% in the absence of GCGC complex.

5.2.6   Adsorption of noble gas on Metal surfaces

The vdW interaction is the most dominant interaction in predicting the interaction energies and the distance of noble gases on metal surfaces. Previous theoretical, and experimental researches on such systems show the importance of physisorption of noble gases on the metal surfaces. The conclusion of on-site preferences of noble gases on metal surfaces was in confusion for long time. In Ref. [231], Authors satisfactorily reviewed the history of preference by noble gases on metal surface site (on top or hollow). Some recent studies[231,261,273] show that the noble gases prefer to stay on top of metal atom instead of higher coordinate sites. So, in our calculations, we discuss only the on-top adsorption of Ar, Kr, Xe on Cu(110), Cu(111), Pd(111), and Pt(111) metal surfaces. In Table 5.8, both the adsorption distances and the energies are tabulated considering PBE functional representing the GGA method, SCAN, TM, TMTPSS representing meta-GGA, and SCAN+rVV10, TM+rVV10L, TMTPSS+rVV10L methods representing vdW corrected meta-GGA functionals. Also, we collect some available experimental values and tabulated in the last row. Compare to available experimental values, it is observed that PBE overestimates the distance between the noble gas atom and metal atom, and underestimates the adsorption energy (E_{ad}) up to a large extent. The adsorption distance (d) of SCAN and TMTPSS functionals for Xe on Cu(111) surface is 3.56 and 3.55 Å , respectively, and these are close to the experimental value. But for this system, the adsorption energy E_{ad} of SCAN and TMTPSS are far from the reference value E_{ad}=190 meV. The addition of rVV10 non-local correlation to the meta-GGA functionals shorten the adsorption distance d and increase E_{ad}. The adsorption obtained using the SCAN functional in case of Xe/Cu(111), TM in case of Xe/Pd(111), and SCAN+rVV10 in Xe/Pt(111) agree more closely with the experimental values. TM adsorption energy for Xe/Cu(111), SCAN+rVV10 adsorption energies for Kr/Pt(111), TM+rVV10L adsorption energy for Xe/Pt(111), and TMTPSS+rVV10L energy for Xe/Pd(111) are close to experimental values. The adsorption energy magnitude of both TM+rVV10L and TMTPSS+rVV10L are

Table 5.8: The equilibrium distance (d in Å) representing the distance of adsorption and the adsorption energy (E$_d$ in meV) for atop site adsorption of three noble gases Ar, Kr, and Xe on different metal surfaces. The experimental reference values are given in the last row and collected from Ref. [231, 261].

Methods	Xe/Cu(110)		Xe/Cu(111)		Ar/Pd(111)		Kr/Pd(111)		Xe/Pd(111)		Ar/Pt(111)		Kr/Pt(111)		Xe/Pt(111)	
	d	E$_{ad}$	d	E$_{ad}$	d	E$_{ad}$	d	E$_{ad}$	d	E$_{ad}$	d	E$_{ad}$	d	E$_{ad}$	d	E$_{ad}$
PBE	3.75	-29	4.18	-27	3.72	-11	3.69	-23	3.49	-54	3.92	-12	4.09	-19	3.81	-36
SCAN	3.57	-104	**3.56**	-50	3.52	-56	3.38	-96	3.43	-177	3.6	-54	3.57	-73	3.58	-140
TM	3.37	-160	3.49	**-166**	3.56	-68	3.66	-102	**3.15**	-281	3.46	-72	3.46	-115	3.38	-203
TMTPSS	3.52	-129	3.55	-153	3.45	-74	3.34	-135	3.27	-245	3.36	-71	3.44	-106	3.33	-183
SCAN+rVV10	3.49	-199	3.5	-217	3.5	-146	3.37	-203	3.44	-324	3.57	-122	**3.57**	**-166**	3.33	-275
TM+rVV10L	3.05	-238	3.39	-250	3.35	-132	3.22	-219	3.2	-362	3.39	-128	3.42	-179	3.31	**-294**
TMTPSS+rVV10L	3.11	-230	3.49	-240	3.38	-133	3.35	-199	3.38	**-319**	3.36	-120	3.39	-175	3.33	-282
Expt.	—	—	3.60	-190	—	—	—	—	3.07	-320	—	—	—	—	3.54	-320
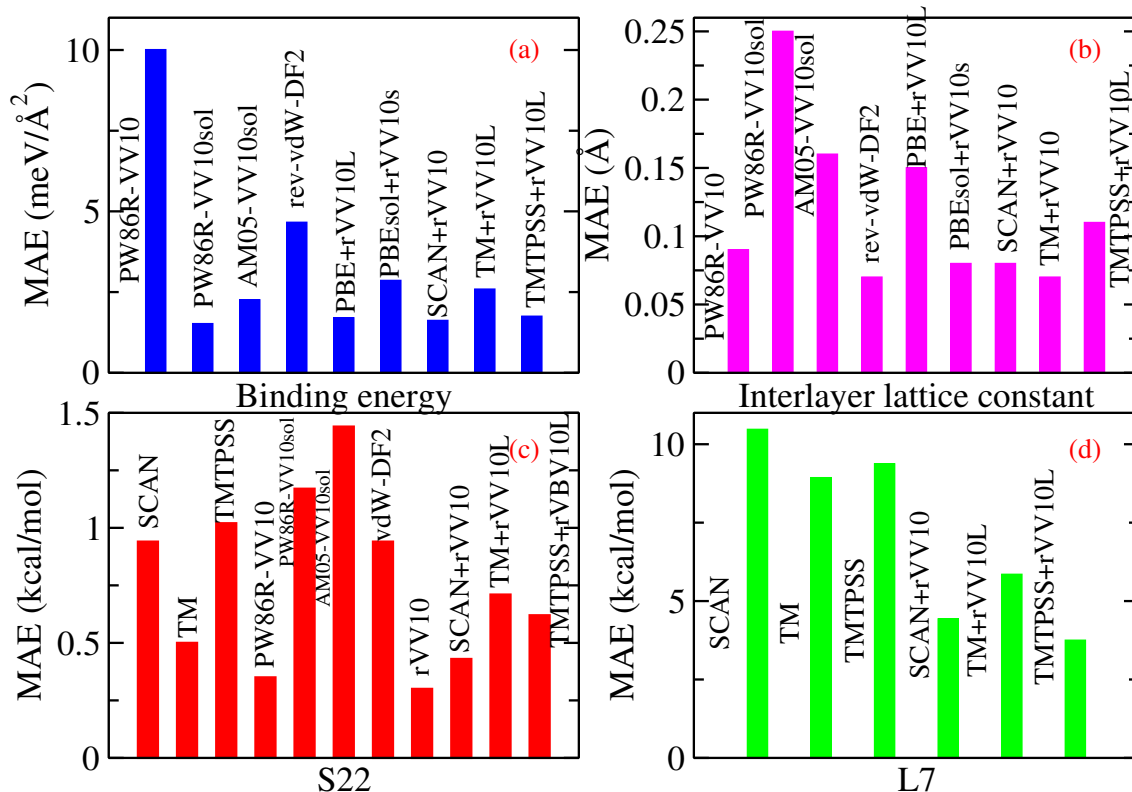
Figure 5.7: The pictorial view of MAEs in (a) binding energies, (b) interlayer lattice constant of 26 layered materials, (c) interaction energies of S22, and (d) L7 test sets.

more than SCAN+rVV10 functionals in all the cases, which implies more tightly bound systems than SCAN+rVV10.

5.3 Concluding Remarks

The long-range dispersion interaction is very crucial for the systems starting from simple noble-gas dimer, smaller molecular complex, larger molecular complexes to layered materials. In this context, we propose the use of advance rVV10 correlation with the recently developed TM meta-GGA exchange-correlation functional. As two correlation functionals of TM, and TMTPSS can be combined with the TM exchange, we examine the compatibility of both these correlations with the rVV10 non-local correction. The developed functionals named TM+rVV10L and TMTPSS+rVV10L are very effective due to the adjustable proportion of semilocal functionals and the rVV10 correlation.Applying

these functionals to systems dominated by dispersion interaction e.g., a set of 26 layered materials, noble gas-solids, noble gas-dimers, a set of 22 molecular complexes, a set of 7 large sized complexes, and physisorption of noble gases on metal surfaces, it is concluded that these methods can be applied to new contemporary molecular complexes to solids due ti their well-balanced accuracy. Also, we find that TM+rVV10L functional is better in predicting structural properties, whereas TMTPSS+rVV10L is better in describing binding energies. For an overview and comparison, we plot mean absolute errors of different data sets in Fig. 5.7 using developed functionals and some available results. Due to the more precise interpretation of interaction energies, the present proposition can be used for the large scale structural properties of the van der Waals systems.

Chapter 6

Summary and Outlook

The whole thesis is dedicated to the construction of new exchange-correlation energy functionals within density functional theory. The basic proposition is to work on model exchange holes for proposing new methods. Starting with two-dimensional models, we have shown the importance of 2D DFT and its application. Our methods for 2D XC functionals are promising for quantum dot systems. The presence of Laplacian of density in functionals or potentials leads to numerical problems, particularly, the Laplacian of density tends to diverge near nucleus. So, using Laplacian free model of exchange hole, the band gap problem of KS DFT is addressed. Next, we have shown the construction of exchange holes from a given exchange energy functional and constructed three types of range-separated hybrid functionals that are accurate for quantum molecular complexes. Finally, we use a non-local correlation with the semilocal XC functional constructed from the exchange hole to address dispersion dominated systems. Overall, we covered important fields where DFT needs to be revisited repeatedly.

Our development in these fields will help the DFT community do multiscale calculations and further develop new methods. Notably, using our 2D XC functionals, the quantum dot systems representing artificial graphene-like systems can be analyzed more accurately. In calculating the bandgap of bulk materials, our model MBR-TBMBJ is quite successful, but in the case of 2D-layered materials, new potentials are needed to be developed. Again, our proposition, along with the HJS model, will be beneficial in the case of

hybrid functional development. To study van der Waals systems, the nonlocal correction to the semilocal density functionals is a successful method. Other than rVV10 nonlocal correlation, the correlations like D2, D3, or D4 can readily be made appropriate for advance semilocal functionals.

References

[1] E. Engel and R. M. Dreizler. Springer, Berlin, 2011.

[2] R.G. Parr and W. Yang Yang. Oxford Univ. Press, 1989.

[3] C. C. J. Roothaan, *Rev. Mod. Phys.* **23**, 69–89 (1951).

[4] L. H. Thomas, *Math. Proc. Camb. Philos. Soc.* **23**, 542548 (1927).

[5] Elliott H Lieb and Barry Simon, *Advances in Mathematics*, **23**, 22–116 (1977).

[6] P. Hohenberg and W. Kohn, *Phys. Rev.* **136**, B864 (1964).

[7] Elliott H. Lieb, *Int. J. Quantum Chem.* **24**, 243–277 (1983).

[8] W. Kohn and L. J. Sham, *Phys. Rev.* **140**, A1133 (1965).

[9] W. Kohn, *Rev. Mod. Phys.* **71**, 1253–1266 (1999).

[10] John P. Perdew and Karla Schmidt, *AIP Conf. Proc*, **577**, 1–20 (2001).

[11] S. H. Vosko, L. Wilk, and M. Nusair, *Can. J. Phys.* **58**, 1200–1211 (1980).

[12] P. S. Svendsen and U. von Barth, *Phys. Rev. B*, **54**, 17402–17413 (1996).

[13] E. Engel and R. M. Dreizler. Springer, Berlin, 2011.

[14] A. D. Becke, *Phys. Rev. A*, **38**, 3098–3100 (1988).

[15] John P. Perdew, *Phys. Rev. Lett.* **55**, 1665–1668 (1985).

[16] John P. Perdew and Wang Yue, *Phys. Rev. B*, **33**, 8800–8802 (1986).

[17] John P. Perdew, Kieron Burke, and Matthias Ernzerhof, *Phys. Rev. Lett.* **77**, 3865–3868 (1996).

[18] Elliott H. Lieb and Stephen Oxford, *Int. J. Quantum Chem.* **19**, 427–439 (1981).

[19] John P. Perdew et al., *Phys. Rev. Lett.* **100**, 136406 (2008).

[20] A. D. Becke, *Int. J. Quantum Chem.* **23**, 1915–1922 (1983).

[21] A. D. Becke, *J. Chem. Phys.* **85**, 7184–7187 (1986).

[22] Bikash Patra et al., *Phys. Rev. B*, **100**, 155140 (2019).

[23] Jorge M. del Campo et al., *J. Chem. Phys.* **136**, 104108 (2012).

[24] Axel D. Becke, *J. Chem. Phys.* **107**, 8554–8560 (1997).

[25] Axel D. Becke, *J. Chem. Phys.* **109**, 2092–2098 (1998).

[26] Troy Van Voorhis and Gustavo E. Scuseria, *J. Chem. Phys.* **109**, 400–410 (1998).

[27] A. Seidl et al., *Phys. Rev. B*, **53**, 3764–3774 (1996).

[28] James W. Furness and Jianwei Sun, *Phys. Rev. B*, **99**, 041119 (2019).

[29] John P. Perdew et al., *Phys. Rev. Lett.* **82**, 2544–2547 (1999).

[30] Jianmin Tao et al., *Phys. Rev. Lett.* **91**, 146401 (2003).

[31] John P. Perdew et al., *Phys. Rev. Lett.* **103**, 026403 (2009).

[32] Jianwei Sun, Bing Xiao, and Adrienn Ruzsinszky, *J. Chem. Phys.* **137**, 051101 (2012).

[33] Jianwei Sun, John P. Perdew, and Adrienn Ruzsinszky, *Proc. Natl. Acad. Sci.* **112**, 685–689 (2015).

[34] Jianwei Sun, Adrienn Ruzsinszky, and John P. Perdew, *Phys. Rev. Lett.* **115**, 036402 (2015).

[35] Thilo Aschebrock and Stephan Kümmel, *Phys. Rev. Research*, **1**, 033082 (2019).

[36] Albert P. Bartk and Jonathan R. Yates, *J. Chem. Phys.* **150**, 161101 (2019).

[37] D. Meja-Rodrguez and S. B. Trickey, *J. Chem. Phys.* **151**, 207101 (2019).

[38] James William Furness et al., *J. Phys. Chem. Lett.* **0**, null (0).

[39] Richard M. Koehl, Gregory K. Odom, and Gustavo E. Scuseria, *Mol. Phys.* **87**, 835–843 (1996).

[40] By TROY VAN VOORHIS GUSTAVO E. SCUSERIA, *Mol. Phys.* **92**, 601–608 (1997).

[41] Yan Zhao and Donald G. Truhlar, *J. Chem. Phys.* **125**, 194101 (2006).

[42] Jianmin Tao and Yuxiang Mo, *Phys. Rev. Lett.* **117**, 073001 (2016).

[43] Subrata Jana, Abhilash Patra, and Prasanjit Samal, *J. Chem. Phys.* **149**, 044120 (2018).

[44] Subrata Jana, Kedar Sharma, and Prasanjit Samal, *J. Chem. Phys.* **149**, 164703 (2018).

[45] Yuxiang Mo et al., *J. Chem. Phys.* **145**, 234306 (2016).

[46] Yuxiang Mo, Guocai Tian, and Jianmin Tao, *Phys. Chem. Chem. Phys.* **19**, 21707–21713 (2017).

[47] Enrico Clementi and Subhas J. Chakravorty, *J. Chem. Phys.* **93**, 2591–2602 (1990).

[48] Axel D. Becke, *J. Chem. Phys.* **104**, 1040–1046 (1996).

[49] John P. Perdew and Yue Wang, *Phys. Rev. B*, **45**, 13244–13249 (1992).

[50] C. Adamo and V. Barone, *Chem. Phys. Lett.* **274**, 242 –250 (1997).

[51] Chengteh Lee, Weitao Yang, and Robert G. Parr, *Phys. Rev. B*, **37**, 785–789 (1988).

[52] Carlo Adamo and Vincenzo Barone, *J. Chem. Phys.* **110**, 6158–6170 (1999).

[53] Thierry Leininger et al., *Chem. Phys. Lett.* **275**, 151 –160 (1997).

[54] Jochen Heyd, Gustavo E. Scuseria, and Matthias Ernzerhof, *J. Chem. Phys.* **118**, 8207–8215 (2003).

[55] Jochen Heyd, ustavo E. Scuseria, and Matthias Ernzerhof, *J. Chem. Phys.* **118**, 8207–8215 (2003).

[56] Jochen Heyd and Gustavo E. Scuseria, *J. Chem. Phys.* **121**, 1187–1192 (2004).

[57] Susi Lehtola et al., *SoftwareX*, **7**, 1 –5 (2018).

[58] Miguel A.L. Marques, Micael J.T. Oliveira, and Tobias Burnus, *Comp. Phys. Comm.* **183**, 2272 –2281 (2012).

[59] L. Pollack and J. P. Perdew, *J. Phys.: Condens. Matter*, **12**, 1239 (1999).

[60] Yong-Hoon Kim et al., *Phys. Rev. B*, **61**, 5202–5211 (2000).

[61] Lucian A. Constantin, John P. Perdew, and J. M. Pitarke, *Phys. Rev. Lett.* **101**, 016406 (2008).

[62] Lucian A. Constantin, *Phys. Rev. B*, **78**, 155106 (2008).

[63] Letizia Chiodo et al., *Phys. Rev. Lett.* **108**, 126402 (2012).

[64] Lucian A. Constantin, *Phys. Rev. B*, **93**, 121104 (2016).

[65] Claudio Attaccalite et al., *Phys. Rev. Lett.* **88**, 256601 (2002).

[66] E. Räsänen et al., *Phys. Rev. Lett.* **108**, 246803 (2012).

[67] Marco Polini et al., *Nature Nanotechnology*, **8**, 625–633 (2013).

[68] M. Aichinger et al., *Phys. Rev. B*, **89**, 235433 (2014).

[69] I Kylnp et al., *J. Phys. Condens. Matter*, **27**, 425501 (2015).

[70] Ilkka Kylnp et al., *New J. Phys.* **18**, 083014 (2016).

[71] Takao Tsuneda and Kimihiko Hirao, *Phys. Rev. B*, **62**, 15527–15531 (2000).

[72] Jianmin Tao, Michael Springborg, and John P. Perdew, *J. Chem. Phys.* **119**, 6457–6464 (2003).

[73] J. W. Negele and D. Vautherin, *Phys. Rev. C*, **5**, 1472–1493 (1972).

[74] Subrata Jana and Prasanjit Samal, *J. Phys. Chem. A*, **121**, 4804–4811 (2017).

[75] S. Pittalis et al., *Phys. Rev. B*, **76**, 235314 (2007).

[76] Stefano Pittalis et al., *Phys. Rev. A*, **79**, 012503 (2009).

[77] J. B. Krieger, Yan Li, and G. J. Iafrate, *Phys. Rev. A*, **46**, 5453–5458 (1992).

[78] P. A. M. Dirac, *Math. Proc. Camb. Philos. Soc.* **26**, 376385 (1930).

[79] J. G. Vilhena et al., *J. Chem. Theory Comput.* **10**, 1837–1842 (2014).

[80] Miguel A.L. Marques et al., *Comput. Phys. Commun.* **151**, 60 –78 (2003).

[81] A. K. Rajagopal and John C. Kimball, *Phys. Rev. B*, **15**, 2819–2825 (1977).

[82] A. D. Becke, *J. Chem. Phys.* **88**, 1053–1062 (1988).

[83] J. G. Vilhena et al., *J. Chem. Theory Comput.* **10**, 1837–1842 (2014).

[84] Stefano Pittalis et al., *Phys. Rev. A*, **79**, 012503 (2009).

[85] S. Pittalis, E. Räsänen, and M. A. L. Marques, *Phys. Rev. B*, **78**, 195322 (2008).

[86] S. Pittalis et al., *Phys. Rev. B*, **79**, 085316 (2009).

[87] E. Räsänen, S. Pittalis, and C. R. Proetto, *Phys. Rev. B*, **81**, 195103 (2010).

[88] M Taut, *J. Phys. A*, **27**, 1045 (1994).

[89] Massimo Rontani et al., *J. Chem. Phys.* **124**, 124102 (2006).

[90] Francesco Pederiva, C. J. Umrigar, and E. Lipparini, *Phys. Rev. B*, **62**, 8120–8125 (2000).

[91] H. Saarikoski et al., *Phys. Rev. B*, **67**, 205327 (2003).

[92] Alexander Odriazola et al., *J. Phys.: Condens. Matter*, **25**, 505504 (2013).

[93] Stephanie M. Reimann and Matti Manninen, *Rev. Mod. Phys.* **74**, 1283–1342 (2002).

[94] Renato Colle and Oriano Salvetti, *Theor. Chim. Acta*, **37**, 329–334 (1975).

[95] Renato Colle and Oriano Salvetti, *Theor. Chim. Acta*, **53**, 55–63 (1979).

[96] Takao Tsuneda and Kimihiko Hirao, *Chem. Phys. Lett.* **268**, 510 –520 (1997).

[97] Takao Tsuneda, Toshihisa Suzumura, and Kimihiko Hirao, *J. Chem. Phy.* **110**, 10664–10678 (1999).

[98] A. K. Rajagopal, J. C. Kimball, and Mahadev Banerjee, *Phys. Rev. B*, **18**, 2339–2345 (1978).

[99] Federico Moscard and Emilio San-Fabin, *Int. J. Quantum Chem.* **40**, 23–32 (1991).

[100] Abhilash Patra, Subrata Jana, and Prasanjit Samal, *J. Chem. Phys.* **148**, 134117 (2018).

[101] Abhilash Patra, Subrata Jana, and Prasanjit Samal, *J. Phys. Chem. A*, **122**, 3455–3461 (2018).

[102] Mel Levy and John P. Perdew, *Phys. Rev. A*, **32**, 2010–2021 (1985).

[103] Mel Levy, *Int. J. Quantum Chem.* **36**, 617–619 (1989).

[104] Andreas Görling and Mel Levy, *Phys. Rev. A*, **45**, 1509–1517 (1992).

[105] John P. Perdew et al., *Phys. Rev. Lett.* **49**, 1691–1694 (1982).

[106] John P. Perdew and Mel Levy, *Phys. Rev. Lett.* **51**, 1884–1887 (1983).

[107] John P. Perdew et al., *Proc Natl Acad Sci*, **114**, 2801–2806 (2017).

[108] T. Grabo, T. Kreibich, and E.K.U. Gross, *Molecular Engineering*, **7**, 27–50 (1997).

[109] Andreas Görling, *Phys. Rev. B*, **53**, 7024–7029 (1996).

[110] Ji Klime et al., *J. Chem. Phys.* **143**, 102816 (2015).

[111] Paula Mori-Sánchez, Aron J. Cohen, and Weitao Yang, *Phys. Rev. Lett.* **100**, 146401 (2008).

[112] M. K. Y. Chan and G. Ceder, *Phys. Rev. Lett.* **105**, 196403 (2010).

[113] Matthias Ernzerhof and Gustavo E. Scuseria, *J. Chem. Phys.* **110**, 5029–5036 (1999).

[114] Jochen Heyd et al., *J. Chem. Phys.* **123**, 174101 (2005).

[115] Zeng-hui Yang et al., *Phys. Rev. B*, **93**, 205205 (2016).

[116] John P. Perdew et al., *Proc Natl Acad Sci*, **114**, 2801–2806 (2017).

[117] J.P. Perdew, *Chem. Phys. Lett.* **64**, 127 –130 (1979).

[118] Mark R. Pederson and Chun C. Lin, *J. Chem. Phys.* **88**, 1807–1817 (1988).

[119] J. P. Perdew and Alex Zunger, *Phys. Rev. B*, **23**, 5048–5079 (1981).

[120] Vladimir I. Anisimov, Jan Zaanen, and Ole K. Andersen, *Phys. Rev. B*, **44**, 943–954 (1991).

[121] Wilfried G. Aulbur, Martin Städele, and Andreas Görling, *Phys. Rev. B*, **62**, 7121–7132 (2000).

[122] Sergey V. Faleev, Mark van Schilfgaarde, and Takao Kotani, *Phys. Rev. Lett.* **93**, 126406 (2004).

[123] Mark van Schilfgaarde, Takao Kotani, and Sergey V. Faleev, *Phys. Rev. B*, **74**, 245125 (2006).

[124] Athanasios N. Chantis, Mark van Schilfgaarde, and Takao Kotani, *Phys. Rev. B*, **76**, 165126 (2007).

[125] M. Shishkin and G. Kresse, *Phys. Rev. B*, **75**, 235102 (2007).

[126] M. Shishkin, M. Marsman, and G. Kresse, *Phys. Rev. Lett.* **99**, 246403 (2007).

[127] Axel D. Becke and Erin R. Johnson, *J. Chem. Phys.* **124**, 221101 (2006).

[128] Fabien Tran, Peter Blaha, and Karlheinz Schwarz, *J. Phys. Condens. Matter*, **19**, 196208 (2007).

[129] Fabien Tran and Peter Blaha, *Phys. Rev. Lett.* **102**, 226401 (2009).

[130] M. Kuisma et al., *Phys. Rev. B*, **82**, 115106 (2010).

[131] R. Armiento and S. Kümmel, *Phys. Rev. Lett.* **111**, 036402 (2013).

[132] Prashant Singh et al., *Phys. Rev. B*, **93**, 085204 (2016).

[133] Prashant Singh, Manoj K Harbola, and Duane D Johnson, *J. Phys. Condens. Matter*, **29**, 424001 (2017).

[134] Sujoy Datta et al., *J. Phys. Condens. Matter*, **31**, 495502 (2019).

[135] R. van Leeuwen and E. J. Baerends, *Phys. Rev. A*, **49**, 2421–2431 (1994).

[136] Oleg Gritsenko et al., *Phys. Rev. A*, **51**, 1944–1954 (1995).

[137] A. D. Becke and M. R. Roussel, *Phys. Rev. A*, **39**, 3761–3767 (1989).

[138] Jianmin Tao, Ireneusz W. Bulik, and Gustavo E. Scuseria, *Phys. Rev. B*, **95**, 125115 (2017).

[139] Patrick Jemmer and Peter J. Knowles, *Phys. Rev. A*, **51**, 3571–3575 (1995).

[140] Fabien Tran et al., *J. Chem. Phys.* **149**, 144105 (2018).

[141] Michael Springborg, *Chem. Phys. Lett.* **308**, 83 –90 (1999).

[142] Jianmin Tao, *J. Chem. Phys.* **115**, 3519–3530 (2001).

[143] Enrico Clementi and Carla Roetti, *At. Data Nucl. Data Tables*, **14**, 177 –478 (1974).

[144] David Koller, Fabien Tran, and Peter Blaha, *Phys. Rev. B*, **83**, 195134 (2011).

[145] David Koller, Fabien Tran, and Peter Blaha, *Phys. Rev. B*, **85**, 155109 (2012).

[146] P. Blaha et al. *WIEN2K, An Augmented Plane Wave + Local Orbitals Program for Calculating Crystal Properties*. Wien, Austria: Karlheinz Schwarz, Techn. Universität Wien, Austria, 2001.

[147] G. Kresse and J. Hafner, *Phys. Rev. B*, **47**, 558–561 (1993).

[148] G. Kresse and J. Furthmller, *Comput. Mater. Sci.* **6**, 15 –50 (1996).

[149] G Kresse and J Hafner, *J. Phys. Condens.Matter*, **6**, 8245 (1994).

[150] G. Kresse and D. Joubert, *Phys. Rev. B*, **59**, 1758–1775 (1999).

[151] Hidenori Hiramatsu et al., *Chem. Mater.* **20**, 326–334 (2008).

[152] Jiangang He and Cesare Franchini, *Phys. Rev. B*, **86**, 235117 (2012).

[153] Martin Schreyer and Martin Jansen, *Solid State Sci.* **3**, 25 –30 (2001).

[154] Ruei-Sung Yu et al., *Appl. Phys. Lett.* **90**, 191117 (2007).

[155] J. van Elp et al., *Phys. Rev. B*, **44**, 6090–6103 (1991).

[156] mile Bvillon et al., *J. Phys. Condens. Matter*, **20**, 145217 (2008).

[157] N. Kumada, N. Kinomura, and A.W. Sleight, *Materials Research Bulletin*, **35**, 2397 –2402 (2000).

[158] Rajalakshmi Ramachandran et al., *J. Chem. Sci.* **123**, 517–524 (2011).

[159] T. Saitoh et al., *Phys. Rev. B*, **51**, 13942–13951 (1995).

[160] John Robertson, *J. Vac. Sci. Technol. B Microelectron Nanometer Struct Process Meas Phenom*, **18**, 1785–1791 (2000).

[161] S. H. Wemple, *Phys. Rev. B*, **2**, 2679–2689 (1970).

[162] Yong Xu and Martin A.A. Schoonen, *American Mineralogist*, **85**, 543 (2000).

[163] D.L. Greenaway and R. Nitsche, *J. Phys. Chem. Solids*, **26**, 1445 –1458 (1965).

[164] K. Terashima and I. Imai, *Solid State Commun.* **63**, 315 –318 (1987).

[165] M. Traving et al., *Phys. Rev. B*, **63**, 035107 (2001).

[166] K. K. Kam and B. A. Parkinson, *J. Phys. Chem*, **86**, 463–467 (1982).

[167] S. G. Patel, S. K. Arora, and M. K. Agarwal, *Bull. Mater. Sci.* **21**, 297–301 (1998).

[168] G.K. Wertheim, F.J. DiSalvo, and D.N.E. Buchanan, *Solid State Communications*, **13**, 1225 –1228 (1973).

[169] M. Gvishi and D.S. Tannhauser, *J. Phys. Chem. Solids*, **33**, 893 –911 (1972).

[170] Kerstin Hummer and Claudia Ambrosch-Draxl, *Phys. Rev. B*, **72**, 205205 (2005).

[171] Colin R. Groom et al., *Acta Crystallographica Section B*, **72**, 171–179 (2016).

[172] M. Houmad et al., *Carbon*, **94**, 1021 –1027 (2015).

[173] Masoud Shahrokhi and Cline Leonard, *J. Alloys Compd.* **693**, 1185 –1196 (2017).

[174] D A Evans et al., *J. Phys. Condens. Matter*, **20**, 075233 (2008).

[175] Thilo Aschebrock and Stephan Kümmel, *Phys. Rev. Research*, **1**, 033082 (2019).

[176] Abhilash Patra et al., *Phys. Chem. Chem. Phys.* **21**, 19639–19650 (2019).

[177] Jingjing Zheng, Yan Zhao, and Donald G. Truhlar, *J. Chem. Theory Comput.* **5**, 808–821 (2009).

[178] Andreas Dreuw, Jennifer L. Weisman, and Martin Head-Gordon, *J. Chem. Phys.* **119**, 2943–2946 (2003).

[179] David J. Tozer and Nicholas C. Handy, *J. Chem. Phys.* **109**, 10180–10189 (1998).

[180] Aron J. Cohen, Paula Mori-Snchez, and Weitao Yang, *Chemical Reviews*, **112**, 289–320 (2012).

[181] Aron J. Cohen, Paula Mori-Sánchez, and Weitao Yang, *Science*, **321**, 792–794 (2008).

[182] Paula Mori-Snchez, Aron J. Cohen, and Weitao Yang, *J. Chem. Phys.* **125**, 201102 (2006).

[183] Paula Mori-Sánchez, Aron J. Cohen, and Weitao Yang, *Phys. Rev. Lett.* **100**, 146401 (2008).

[184] John P. Perdew et al., *Phys. Rev. Lett.* **49**, 1691–1694 (1982).

[185] Aliaksandr V. Krukau et al., *J. Chem. Phys.* **129**, 124103 (2008).

[186] Oleg A. Vydrov and Gustavo E. Scuseria, *J. Chem. Phys.* **125**, 234109 (2006).

[187] Thomas M. Henderson, Benjamin G. Janesko, and Gustavo E. Scuseria, *J. Chem. Phys.* **128**, 194105 (2008).

[188] John P. Perdew and Yue Wang, *Phys. Rev. B*, **46**, 12947–12954 (1992).

[189] Lucian A. Constantin et al., *Phys. Rev. Lett.* **106**, 186406 (2011).

[190] Eduardo Fabiano, Lucian A. Constantin, and Fabio Della Sala, *Phys. Rev. B*, **82**, 113104 (2010).

[191] Lucian A. Constantin et al., *Phys. Rev. B*, **93**, 045126 (2016).

[192] Eduardo Fabiano et al., *J. Chem. Theory Comput*, **11**, 122–131 (2014).

[193] E Fabiano, Lucian A Constantin, and F Della Sala, *J. Chem. Theory Comput*, **7**, 3548–3559 (2011).

[194] E Fabiano, Lucian A Constantin, and F Della Sala, *J. Chem. Phys.* **134**, 194112 (2011).

[195] E. Fabiano, Lucian A. Constantin, and F. Della Sala, *Int. J. Quantum Chem.* **113**, 673–682 (2013).

[196] Aleksandr V Terentjev et al., *Computation*, **6**, 7 (2018).

[197] Fabien Tran, Julia Stelzl, and Peter Blaha, *J. Chem. Phys.* **144**, 204120 (2016).

[198] Saverio Moroni, David M. Ceperley, and Gaetano Senatore, *Phys. Rev. Lett.* **75**, 689–692 (1995).

[199] Julien Toulouse, Franois Colonna, and Andreas Savin, *J. Chem. Phys.* **122**, 014110 (2005).

[200] CD Hu and David C Langreth, *Phys. Rev. B*, **33**, 943 (1986).

[201] M. Valiev et al., *Comput. Phys. Commun.* **181**, 1477 –1489 (2010).

[202] Roberto Peverati and Donald G. Truhlar, *Philosophical Transactions of the Royal Society of London A: Mathematical, Physical and Engineering Sciences*, **372**, (2014).

[203] Larry A. Curtiss et al., *J. Chem. Phys.* **94**, 7221–7230 (1991).

[204] Lars Goerigk et al., *Phys. Chem. Chem. Phys.* **19**, 32184–32215 (2017).

[205] Yan Zhao and Donald G. Truhlar, *J. Chem. Theory Comput.* **3**, 289–300 (2007).

[206] Yan Zhao and Donald G. Truhlar, *J. Chem. Phys.* **125**, 194101 (2006).

[207] Ekaterina I. Izgorodina, Michelle L. Coote, and Leo Radom, *J. Phys. Chem. A*, **109**, 7558–7566 (2005).

[208] Sijie Luo, Yan Zhao, and Donald G. Truhlar, *Phys. Chem. Chem. Phys.* **13**, 13683–13689 (2011).

[209] Roberto Peverati and Donald G. Truhlar, *J. Chem. Theory Comput.* **8**, 2310–2319 (2012).

[210] Roberto Peverati, Yan Zhao, and Donald G. Truhlar, *J. Phys. Chem. Lett.* **2**, 1991–1997 (2011).

[211] Yan Zhao, Nathan E. Schultz, and D. G. Truhlar, *J. Chem. Phys.* **123**, 161103 (2005).

[212] Yan Zhao and Donald G. Truhlar, *J. Phys. Chem. A*, **110**, 10478–10486 (2006).

[213] Oleg A. Vydrov and Gustavo E. Scuseria, *J. Chem. Phys.* **125**, 234109 (2006).

[214] Oleg A. Vydrov and Troy Van Voorhis, *J. Chem. Phys.* **130**, 104105 (2009).

[215] V. Wang et al., *Solid State Commun.* **177**, 74 –79 (2014).

[216] Marcus Elstner et al., *J. Chem. Phys.* **114**, 5149–5155 (2001).

[217] Stefan Grimme, *J. Comput. Chem.* **27**, 1787–1799 (2006).

[218] Stefan Grimme et al., *J. Chem. Phys.* **132**, 154104 (2010).

[219] Alexandre Tkatchenko and Matthias Scheffler, *Phys. Rev. Lett.* **102**, 073005 (2009).

[220] Alexandre Tkatchenko et al., *Phys. Rev. Lett.* **108**, 236402 (2012).

[221] Wei Liu et al., *Phys. Rev. Lett.* **115**, 036104 (2015).

[222] Henrik Rydberg et al., *Phys. Rev. B*, **62**, 6997–7006 (2000).

[223] H. Rydberg et al., *Phys. Rev. Lett.* **91**, 126402 (2003).

[224] M. Dion et al., *Phys. Rev. Lett.* **92**, 246401 (2004).

[225] Kyuho Lee et al., *Phys. Rev. B*, **82**, 081101 (2010).

[226] Fabien Tran et al., *Phys. Rev. Materials*, **3**, 063602 (2019).

[227] Axel D. Becke and Erin R. Johnson, *J. Chem. Phys.* **122**, 154104 (2005).

[228] Erin R. Johnson and Axel D. Becke, *J. Chem. Phys.* **123**, 024101 (2005).

[229] Axel D. Becke and Erin R. Johnson, *J. Chem. Phys.* **123**, 154101 (2005).

[230] Erin R. Johnson and Axel D. Becke, *J. Chem. Phys.* **124**, 174104 (2006).

[231] R D Diehl et al., *J. Phys. Condens. Matter*, **16**, S2839–S2862 (2004).

[232] Robert A DiStasio, Vivekanand V Gobre, and Alexandre Tkatchenko, *J. Phys. Condens. Matter*, **26**, 213202 (2014).

[233] Jonas Moellmann and Stefan Grimme, *J. Phys. Chem. C*, **118**, 7615–7621 (2014).

[234] Tomá š Bu čko et al., *Phys. Rev. B*, **87**, 064110 (2013).

[235] Kanchana S. Thanthiriwatte et al., *J. Chem. Theory Comput.* **7**, 88–96 (2011).

[236] N. N. Andriichenko and A. Yu. Ermilov, *Russ. J. Phys. Chem. A*, **87**, 1342–1348 (2013).

[237] Jiří Klimeš, David R Bowler, and Angelos Michaelides, *J. Phys. Condens. Matter*, **22**, 022201 (2009).

[238] Valentino R. Cooper, *Phys. Rev. B*, **81**, 161104 (2010).

[239] Kristian Berland and Per Hyldgaard, *Phys. Rev. B*, **89**, 035412 (2014).

[240] Ikutaro Hamada, *Phys. Rev. B*, **89**, 121103 (2014).

[241] Riccardo Sabatini, Tommaso Gorni, and Stefano de Gironcoli, *Phys. Rev. B*, **87**, 041108 (2013).

[242] Oleg A. Vydrov and Troy Van Voorhis, *J. Chem. Phys.* **133**, 244103 (2010).

[243] amonn D. Murray, Kyuho Lee, and David C. Langreth, *J. Chem. Theory Comput.* **5**, 2754–2762 (2009).

[244] Haowei Peng et al., *Phys. Rev. X*, **6**, 041005 (2016).

[245] Haowei Peng and John P. Perdew, *Phys. Rev. B*, **95**, 081105 (2017).

[246] Gábor I. Csonka et al., *Phys. Rev. B*, **79**, 155107 (2009).

[247] Aleksandr V. Terentjev, Lucian A. Constantin, and J. M. Pitarke, *Phys. Rev. B*, **98**, 214108 (2018).

[248] Lucian A. Constantin et al., *Phys. Rev. B*, **93**, 045126 (2016).

[249] Aleksandr V. Terentjev et al., *Computation*, **6**, (2018).

[250] R. Armiento and A. E. Mattsson, *Phys. Rev. B*, **72**, 085108 (2005).

[251] Torbjörn Björkman, *Phys. Rev. B*, **86**, 165109 (2012).

[252] P. S. Svendsen and U. von Barth, *Phys. Rev. B*, **54**, 17402–17413 (1996).

[253] C. F. v. Weizsäcker, *Zeitschrift für Physik*, **96**, 431–458 (1935).

[254] Hong Tang and Jianmin Tao, *Mater. Res. Express*, **5**, 076302 (2018).

[255] Yuxiang Mo et al., *J. Chem. Phys.* **145**, 234306 (2016).

[256] Subrata Jana, Kedar Sharma, and Prasanjit Samal, *J. Phys. Chem. A*, **123**, 6356–6369 (2019).

[257] Hong Tang and Jianmin Tao, *Int. J. Mod. Phys. B*, **33**, 1950300 (2019).

[258] Krzysztof Ro ściszewski et al., *Phys. Rev. B*, **60**, 7905–7910 (1999).

[259] Petr Jurecka et al., *Phys. Chem. Chem. Phys.* **8**, 1985–1993 (2006).

[260] Robert Sedlak et al., *J. Chem. Theory Comput.* **9**, 3364–3374 (2013).

[261] De-Li Chen, W A Al-Saidi, and J Karl Johnson, *J. Phys. Condens. Matter*, **24**, 424211 (2012).

[262] Hendrik J. Monkhorst and James D. Pack, *Phys. Rev. B*, **13**, 5188–5192 (1976).

[263] T. Björkman et al., *Phys. Rev. Lett.* **108**, 235502 (2012).

[264] Qing Hua Wang et al., *Nat. Nanotechnol.* **7**, 699 EP – (2012).

[265] Manish Chhowalla et al., *Nat Chem.* **5**, 263 EP – (2013).

[266] Mingsheng Xu et al., *Chem. Rev.* **113**, 3766–3798 (2013).

[267] Sheneve Z. Butler et al., *ACS Nano*, **7**, 2898–2926 (2013).

[268] Judith Harl and Georg Kresse, *Phys. Rev. B*, **77**, 045136 (2008).

[269] Fabien Tran and Jrg Hutter, *J. Chem. Phys.* **138**, 204103 (2013).

[270] Martin Callsen and Ikutaro Hamada, *Phys. Rev. B*, **91**, 195103 (2015).

[271] Rafa Podeszwa, Konrad Patkowski, and Krzysztof Szalewicz, *Phys. Chem. Chem. Phys.* **12**, 5974–5979 (2010).

[272] Tait Takatani et al., *J. Chem. Phys.* **132**, 144104 (2010).

[273] De-Li Chen, W. A. Al-Saidi, and J. Karl Johnson, *Phys. Rev. B*, **84**, 241405 (2011).